1993

# Geometric structures of thin films: Pt on Pd(110) and NiO on Ni(100)

Oden Lee Warren
*Iowa State University*

# INFORMATION TO USERS

This manuscript has been reproduced from the microfilm master. UMI films the text directly from the original or copy submitted. Thus, some thesis and dissertation copies are in typewriter face, while others may be from any type of computer printer.

**The quality of this reproduction is dependent upon the quality of the copy submitted.** Broken or indistinct print, colored or poor quality illustrations and photographs, print bleedthrough, substandard margins, and improper alignment can adversely affect reproduction.

In the unlikely event that the author did not send UMI a complete manuscript and there are missing pages, these will be noted. Also, if unauthorized copyright material had to be removed, a note will indicate the deletion.

Oversize materials (e.g., maps, drawings, charts) are reproduced by sectioning the original, beginning at the upper left-hand corner and continuing from left to right in equal sections with small overlaps. Each original is also photographed in one exposure and is included in reduced form at the back of the book.

Photographs included in the original manuscript have been reproduced xerographically in this copy. Higher quality 6" x 9" black and white photographic prints are available for any photographs or illustrations appearing in this copy for an additional charge. Contact UMI directly to order.

U·M·I

University Microfilms International
A Bell & Howell Information Company
300 North Zeeb Road, Ann Arbor, MI 48106-1346 USA
313/761-4700 800/521-0600

Order Number 9335035

# Geometric structures of thin films: Pt on Pd(110) and NiO on Ni(100)

Warren, Oden Lee, Ph.D.

Iowa State University, 1993

U·M·I
300 N. Zeeb Rd.
Ann Arbor, MI 48106

# Geometric structures of thin films: Pt on Pd(110) and NiO on Ni(100)

by

Oden Lee Warren

A Dissertation Submitted to the

Graduate Faculty in Partial Fulfillment of the

Requirements for the Degree of

DOCTOR OF PHILOSOPHY

Department: Chemistry
Major: Physical Chemistry

Approved:

Signature was redacted for privacy.

In Charge of Major Work

Signature was redacted for privacy.

For the Major Department

Signature was redacted for privacy.

For the Graduate College

Iowa State University
Ames, Iowa

1993

## DEDICATION

In memory of my father,

Francis Leon Warren

TABLE OF CONTENTS

# GENERAL INTRODUCTION

Geometric structure is arguably the most fundamental property of a surface. Other quantities, such as chemical reactivity and electronic structure, are known to correlate with structural parameters. Therefore, in order to achieve a microscopic understanding of surface processes, it is imperative that we have a priori knowledge of the relative positions of the atoms. Of course, this necessarily implies the need for studies to be carried out on well-defined surfaces in well-defined environments, e.g., on single-crystalline surfaces in ultrahigh vacuum. The relevance of this statement cannot be stressed enough in this day and age of miniaturization. As the size of solid-state components becomes increasingly smaller, the surface area to volume ratio becomes increasingly larger, and fundamental surface issues become of primal importance.

If the material is single-crystalline, then the logical starting point for the consideration of a surface is the bulk-truncated geometry. However, the mere presence of a surface results in a breaking of symmetry along the surface normal, which implies that the electronic structure of the first few layers differs from that of the bulk. Therefore, the bulk-truncated geometry does not, in general, represent the minimum in surface energy. As a consequence, surfaces usually relax or reconstruct.

Relaxation refers to the case where the surface layers move collectively away from their bulk-like positions, thereby preserving the (1x1) periodicity of the bulk layers. Relaxation generally involves, but is not restricted to, changes in the interlayer spacings. Examples of cases where relaxation encompasses more than changes in the interlayer

spacings include rigid lateral shifts in the first few layers of surfaces with only one mirror plane of symmetry (1), and rumpling of anions and cations in the topmost layer of the (100) surfaces of rocksalt materials (2).

The vast majority of studies on surface relaxation pertain to the low-index surfaces of metals (3,4). From these studies, three trends have emerged. 1) While closed-packed metal surfaces tend to adopt nearly bulk-truncated geometries, more open surfaces exhibit significant multilayer relaxation. 2) If the stacking sequence is ABAB..., then multilayer relaxation tends to be oscillatory, i.e., the first interlayer spacing is contracted relative to the bulk interlayer spacing, the second interlayer spacing is expanded, and so forth. 3) Even for metal surfaces exhibiting significant multilayer relaxation, the magnitude of relaxation tends to decay quite rapidly with depth; typically, only the first two interlayer spacings are detectably different from that of the bulk. Although these trends appear to be complex, they can be understood, at least conceptually, within the framework of a standard model in which metals tend to smooth out their surface corrugation, thereby lowering the kinetic energy of their delocalized surface electrons (5-10). In fact, as will be discussed later, the need for metals to lower the kinetic energy of their delocalized surface electrons can be strong enough to trigger reconstruction in some cases.

Reconstruction refers to the case where the periodicity of at least one surface layer differs from that of the bulk layers. If the change in periodicity does not result in a change in atomic density, then the reconstruction is deemed displacive. Conversely, if the change in

periodicity is due to a change in atomic density, then the reconstruction is deemed reconstructive. Reconstruction is usually discussed apart from relaxation, but in a certain sense, they are not mutually exclusive. For example, a surface that simply relaxes does not reconstruct, but a surface that reconstructs will also relax its atomic positions.

Among the more famous examples of displacive (or density-preserving) reconstructions are the zig-zag structures of the (100) surfaces of Mo and W (11). The topmost layer of both surfaces is unstable with respect to lateral displacements along the diagonal directions of the (1x1) surface mesh, which is quite surprising since an unreconstructed surface would possess high symmetry. At low temperatures, the displacements are correlated, forming zig-zag chains. In the case of W, every surface atom is displaced (12-15), but in the case of Mo, every seventh row of atoms remains in registry with the bulk layers, resulting in antiphase walls (16,17). At higher temperatures, the displacements are thought to be uncorrelated, resulting in a disordered surface with an average periodicity of (1x1) (18-27). The specific driving force for these rather unusual reconstructions is still controversial, but is generally thought to be related to a delicate interplay between electrons and phonons (19,28-31).

Among the more famous examples of reconstructive (or density-changing) reconstructions are the missing-row structures of the (110) surfaces of Ir, Pt, and Au (11). Until recently, it was thought that the clean surfaces of all three metals reconstructed to the (1x2) missing-row structure, which corresponds to an ordered array of (111) microfacets (32-41). However, in the case of Ir, it is now suspected that the (1x2) missing-row structure is stabilized by impurities (42). Alternative models for the clean surface

include the (1x3) missing-row structure, which also corresponds to an ordered array of (111) microfacets (43-47), and a structure in which the surface is grooved on a mesoscopic scale (48). Which of the two represents the ground state structure of the clean surface of Ir is a matter for debate. Nevertheless, it is clear that Ir falls in line with Pt and Au in the regard that the clean surface is unstable with respect to reconstruction.

The specific driving force for the missing-row reconstructions has been shown to be the need for the surface to increase the effective volume available to the delocalized surface electrons, thereby lowering their kinetic energy beyond what is possible by simple smoothing of the surface corrugation (49). Whether the increase in effective volume is energetically favorable is determined by whether the electronic charge density at the surface is above some critical value; only in the cases of Ir, Pt, and Au is this quantity above the critical value. This explanation is consistent with the fact that unreconstructed fcc(110) surfaces of transition and noble metals can be pushed into the (1x2) missing-row structure by a fraction of a monolayer of alkali metal (50-53). Apparently, the amount of charge transfer from the alkali metal to the surface is sufficient to increase the electronic charge density at the surface from below to above the critical value (54).

While it is obvious that much has been established about the geometric aspects of surfaces of bulk materials, comparatively little has been established in this regard about thin films. Thin films offer the exciting possibility of creating novel materials with properties much different from those of either the pure film material or the pure substrate material. The

unusual properties exhibited by Pd on Nb(110) provide one example of this point. Although Pd and Nb are both transition metals, the electronic structure of a monolayer of Pd on Nb(110) is reminiscent of that of a noble metal (55). As a consequence, a monolayer of Pd on Nb(110) is inactive towards the dissociative chemisorption of hydrogen (55), which is rather remarkable in light of the well-known affinity of Pd towards hydrogen (56-59).

As a second example of the unique properties that thin films can possess, Au alone is inactive towards the dehydrogenation of cyclohexane to benzene, but a monolayer of Au on Pt(100) or a monolayer of Pt on Au(100) increases the rate of this reaction fivefold relative to clean Pt (60,61). It is interesting to note that while the ground state structures of the clean (100) surfaces of Au and Pt correspond to quasi-hexagonal reconstructions (11), a monolayer of Au on Pt(100) and a monolayer of Pt on Au(100) exhibit (1x1) periodicity (60-62). Hence, one must wonder about the connection between the structures of these films and their enhanced reactivity. Therefore, as with surfaces of bulk materials, a knowledge of geometric structure is a prerequisite for developing a detailed understanding of the properties of thin films.

In this dissertation, we report on the geometric structures of two thin-film systems: Pt on Pd(110) and NiO on Ni(100). In the case of Pt on Pd(110), we have also found it necessary to investigate the surface geometry of the clean substrate due to a controversy over whether this surface undergoes an order-disorder transition in a manner somewhat analogous to the order-disorder transitions of the (100) surfaces of Mo and W (63-66). The method we have used for determining the structures is

dynamical low-energy electron-diffraction (LEED) analysis (67-71), which is widely regarded to be the standard to which all other surface structural techniques must compare. As a result of the effort reported in this dissertation, we believe that we have increased our understanding of the properties of Pt on Pd(110) and NiO on Ni(100) to a level beyond what is possible without the knowledge of the relative positions of the atoms.

## Explanation of Dissertation Format

Three papers are included in this dissertation. Paper I, "Dynamical Low-Energy Electron-Diffraction Investigation of Lateral Displacements in the Topmost Layer of Pd(110)", appears in Volume 47 of Physical Review B on pages 10848-10851, 1993. Paper II, "Determination of (1x1) and (1x2) Structures of Pt Thin Films on Pd(110) by Dynamical Low-Energy Electron-Diffraction Analysis", appears in Volume 47 of Physical Review B on pages 10839-10847, 1993. Paper III, "Structural Determination of a NiO(111) Film on Ni(100) by Dynamical Low-Energy Electron-Diffraction Analysis", has been submitted to The Journal of Chemical Physics. General conclusions follow the last paper and references cited in the general introduction follow the general conclusions. The appendix documents a newly-developed video LEED system. This system served the purpose of obtaining LEED intensities for the three papers.

PAPER I:

# DYNAMICAL LOW-ENERGY ELECTRON-DIFFRACTION INVESTIGATION OF LATERAL DISPLACEMENTS IN THE TOPMOST LAYER OF Pd(110)

# Dynamical Low-Energy Electron-Diffraction Investigation of Lateral Displacements in the Topmost Layer of Pd(110)

O.L. Warren and P.A. Thiel

Department of Chemistry and Ames Laboratory

Iowa State University

Ames, Iowa 50011

## ABSTRACT

Based on their He-atom diffraction evidence for an order-disorder transition on Pd(110) at 230 K, other authors have proposed a model in which the atoms of the topmost layer are displaced laterally by 0.7 Å along the [001] direction, with the directions of the displacements correlated at $T < 230$ K, but largely uncorrelated at $T > 230$ K. To test this model, we have examined the proposed ordered phase by dynamical low-energy electron-diffraction analysis. Our results favor a nonlaterally displaced geometry, with a contraction of 4.4±1.5% in the first interlayer spacing and an expansion of 1.5±1.5% in the second interlayer spacing, but do not conclusively rule out the possibility of lateral displacements smaller than ca. 0.13 Å. Nevertheless, lateral displacements of the magnitude required to account for the He-atom diffraction results are clearly not present.

# I. INTRODUCTION

The unreconstructed surface of clean Pd(110) has been the subject of numerous conflicting studies. In a He-atom diffraction study restricted to angular scans along the [001] direction, Francis and Richardson (1) observed substantial evidence for an order-disorder transition—possibly first order— on Pd(110) at 230 K, where the average domain width along the [001] direction exceeded the limit set by an instrumental transfer width of 50 Å at T <230 K, but was limited to only about 2-3 unit cells at T >230 K. Since Francis and Richardson were able to rule out the formation of small islands or narrow terraces, they proposed that the atoms of the topmost layer were displaced laterally along the [001] direction, where the directions of the displacements were correlated at T <230 K, but largely uncorrelated at T >230 K. An analysis of the diffraction profiles yielded an estimate of 0.7 Å for the magnitude of the displacements. Subsequently, in a study of low-energy electron-diffraction (LEED) profiles, Wolf et al. (2) observed subtle evidence for an order-disorder transition on Pd(110) at 250 K; however, in contrast to the results of Francis and Richardson, their results indicated that better order existed along the [001] direction at T >250 K. An analysis of the LEED profiles yielded an average domain width of 20 unit cells along the [001] direction at T <250 K and an average domain width of 28 unit cells along the [001] direction at T >250 K. Wolf et al. attributed the differences in the two studies to either different surface conditions or differences in the way electrons and He atoms probe the surface. More recently, Guillopé and Legrand (3) presented theoretical support for the existence of an order-disorder transition on Pd(110) at low

temperature; however, they favored a transition between a nonlaterally displaced phase at low temperature and a laterally disordered phase at higher temperature. And finally, Lahee, Toennies, and Wöll (4) attempted to reproduce the results of Francis and Richardson in a subsequent He-atom diffraction study, but found no evidence for an order-disorder transition on Pd(110). Since each of the results mentioned above pertain to the surface geometry of Pd(110), we conclude that there is no consensus in this regard.

If an order-disorder transition does occur on Pd(110) near 250 K, then its effect on LEED intensity-energy [I(E)] curves appears to be negligible. In the initial dynamical LEED study, Diehl et al. (5) varied the first two interlayer spacings in an analysis of I(E) curves collected at 300 K, and obtained a contraction of 5.7±2% in the first interlayer spacing and an expansion of 0.5±2% in the second interlayer spacing. Subsequently, Skottke et al. (6) varied the first two interlayer spacings in an analysis of I(E) curves collected at 130 K, and obtained a contraction of 5.1±1.5% in the first interlayer spacing and an expansion of 2.9±1.5% in the second interlayer spacing. Although both analyses were carried out for an assumed nonlaterally displaced geometry, we believe that the close similarity between the interlayer spacings obtained above and below the proposed transition temperature favors either the absence of a phase transition or favors a phase transition in which the local geometry remains the same in both phases—such as has been proposed by Francis and Richardson.

In this report, we present the results of a quantitative test of the model proposed by Francis and Richardson by dynamical LEED analysis. In agreement with the previous dynamical LEED results, we find that I(E)

curves collected above and below the proposed transition temperature do not differ significantly; thus, we have restricted our analysis to curves collected below the proposed transition temperature. We assume that the surface is ordered; therefore, our incorporation of lateral displacements entails a rigid shift of the topmost layer along the [001] direction.

## II. EXPERIMENTAL PROCEDURES

Experiments are performed in a stainless-steel ultrahigh-vacuum chamber (base pressure $\leq 1 \times 10^{-10}$ torr) equipped with a single-pass cylindrical mirror analyzer for Auger electron spectroscopy (AES); $\mu$-metal-shielded, display-type, four-grid LEED optics; quadrupole mass spectrometer; sputter gun; and provisions for gas exposure. The Pd(110) crystal is cleaned by cycles of $Ar^+$ bombardment at 300 K and annealing at 1100 K until impurity concentrations, with the possible exception of carbon, are reduced to the noise level of AES. Due to the overlap of the carbon 272-eV and Pd 279-eV Auger transitions, additional steps are taken to ensure that carbon levels are sufficiently low. Oxygen exposure at 640 K to remove carbon as carbon oxides and flashes to 1100 K to desorb residual oxygen are performed until the ratio of Pd 279-eV to Pd 330-eV AES peak-to-peak heights is reduced to a limiting value of ca. 0.17; 2-keV primary beam energy and 1-V peak-to-peak modulation voltage are used in AES work. After cleaning in the above manner, the surface exhibits a high-quality (1x1) LEED pattern. As a test to see if surface saturation can be achieved upon gas exposure, the (2x1) p1g1 LEED pattern of the CO-saturated surface (7) and the (1x2) LEED pattern of the hydrogen-induced paired-row reconstruction (8) are reproduced. Thermal desorption spectra from the CO-saturated surface are regularly consistent with those previously reported for a carbon-free surface (9).

Nineteen normal-incidence I(E) curves are acquired simultaneously (45-250 eV, 1-eV grid) in ca. 10 min with a computer-interfaced video processor and a silicon-intensified-target camera. The crystal is maintained at 105

K during data collection. Normal incidence is determined by comparing symmetry-equivalent curves. The ability to achieve normal incidence is demonstrated in Fig. 1. Sixteen video frames are averaged at each energy to improve the signal-to-noise ratio. Camera saturation effects are tested by acquiring curves over a wide range of camera aperture settings. Background subtraction is performed locally during data acquisition. Beam-current normalization is performed separately after measuring the current as a function of beam energy with the crystal biased sufficiently positive to suppress secondary emission. Equivalent beam averaging—a procedure known to minimize residual experimental errors (10)— is performed when possible, which reduces the set of 19 curves to 8 symmetry-nonequivalent curves over a total-energy range of $\Delta E$ =1153 eV. Beam indices are (0,1), (1,0), (1,1), (0,2), (2,0), (1,2), (2,1), and (0,3). Curves collected in two separate experiments are in excellent agreement, and are averaged to further enhance statistical reliability.

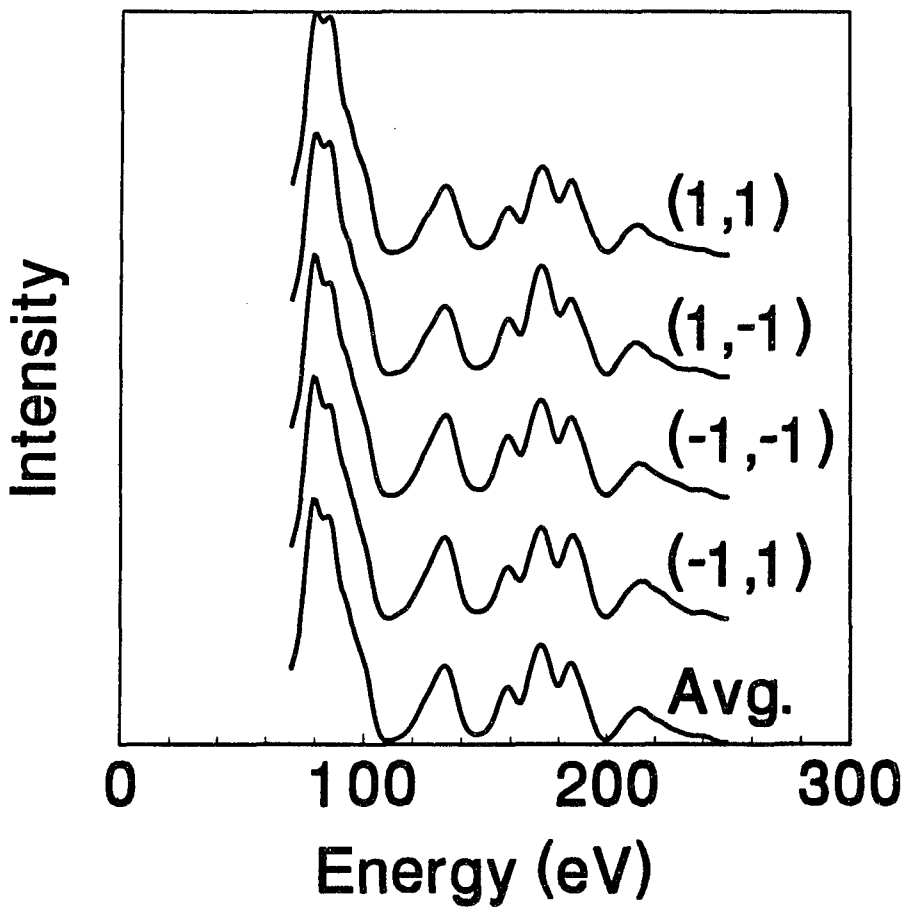


Figure 1. Comparison between experimental I(E) curves for the (1,1) beam set and their average at normal incidence
Curves are collected at 105 K.

## III. COMPUTATIONAL PROCEDURES

Theoretical I(E) curves are calculated up to 260 eV for normal incidence with the LEED package of Van Hove and Tong (11). After calculating reflection and transmission matrices within the self-consistent formalism, interlayer scattering is accomplished by layer doubling. Symmetry is used to reduce the computational effort. Up to 33 symmetry-nonequivalent beams are included when a twofold rotational axis and two orthogonal mirror planes are available as symmetry elements, which is the case when bulk layer registries are maintained throughout the crystal. Up to 61 symmetry-nonequivalent beams are included when only a mirror plane perpendicular to the $[1\bar{1}0]$ direction is available as a symmetry element, which is the case when the topmost layer is allowed to shift along the [001] direction. Two orientational domains must be considered when the topmost layer is allowed to shift (lateral displacements can be correlated in either the positive or negative [001] direction). Since the experimental LEED pattern contains a twofold rotational axis and two orthogonal mirror lines at normal incidence, the diffracted intensities from the two possible domains are assumed to add to the I(E) curves with equal weight. To accomplish this theoretically, we first calculate the intensities for one domain, and then sum the intensities of beams that are equivalent by symmetry when bulk layer registries are maintained throughout the crystal, but not equivalent by symmetry when the topmost layer is allowed to shift along the [001] direction.

Eight phase shifts ($\ell_{max}$ =7) calculated from the tabulated, nonrelativistic Pd potential of Morruzi, Janak, and Williams (12) are used

throughout. The phase shifts are corrected for temperature effects with an effective Debye temperature ($\theta_D$) of 230 K. The real part of the optical potential ($V_{or}$) is assumed to be independent of energy, and is initially set to -10 eV. This parameter is treated as a variable during reliability-factor (r-factor) analysis, and is rigidly shifted in 1-eV steps to obtain the best level of agreement. The final value of $V_{or}$ corresponding to the optimum geometry is -6 eV. The imaginary part of the optical potential ($V_{oi}$) is fixed at -4 eV. Optimization of $\theta_D$ and $V_{oi}$ is not performed since the selected values are nearly identical to previously determined optimum values for Pd(110) (5).

Experimental and theoretical I(E) curves are compared quantitatively with the Pendry r factor ($r_p$) (13). Since this r factor is highly sensitive to spectral noise (13), both sets of curves are smoothed with two passes of a three-point smoothing algorithm (14) prior to r-factor analysis.

## IV. RESULTS AND DISCUSSION

Varied structural parameters–the first interlayer spacing $d_{12}$, the second interlayer spacing $d_{23}$, and a registry shift of magnitude $\sigma$ along the [001] direction in the topmost layer– are shown schematically in Fig. 2. We increment $\sigma$ in steps of 0.1 Å, and for each value of $\sigma$, we independently vary $d_{12}$ and $d_{23}$ over a wide range, both in steps of 0.025 Å. Since the proposed registry shift is away from the hollow site and towards the short bridge site, increasingly larger values of $d_{12}$ are tested for increasingly larger values of $\sigma$. In all cases, we allow $d_{12}$ to range to values considerably larger than predicted by hard spheres of bulk metallic radius.

Figure 3 shows a representative comparison between experimental I(E) curves and best-fit theoretical I(E) curves for $\sigma$ =0, 0.1, 0.2, and 0.7 Å. The displayed curves illustrate various degrees of response with respect to $\sigma$, with the (0,2) curve being the most sensitive and the (1,2) curve being the least sensitive. We find that $\sigma$ =0, which corresponds to a nonlaterally displaced geometry, results in the lowest minimum r factor ($r_p$ =0.168); however, our results do not conclusively rule out the presence of small lateral displacements. For example, the minimum r factor for $\sigma$ =0.1 Å ($r_p$ =0.174) is only negligibly higher than the value obtained for no lateral displacements. In order to determine the uncertainty in $\sigma$, we use Pendry's (13) definition of the variance–$\Delta r = r_{min}(8V_{oi}/\Delta E)^{1/2}$– which indicates that only geometries yielding $r_p$ >0.196 can be ruled out as possible structures when one assumes that the minimum r factor obtained for $\sigma$ =0 corresponds to the global minimum. The minimum r factor for $\sigma$ =0.2 Å

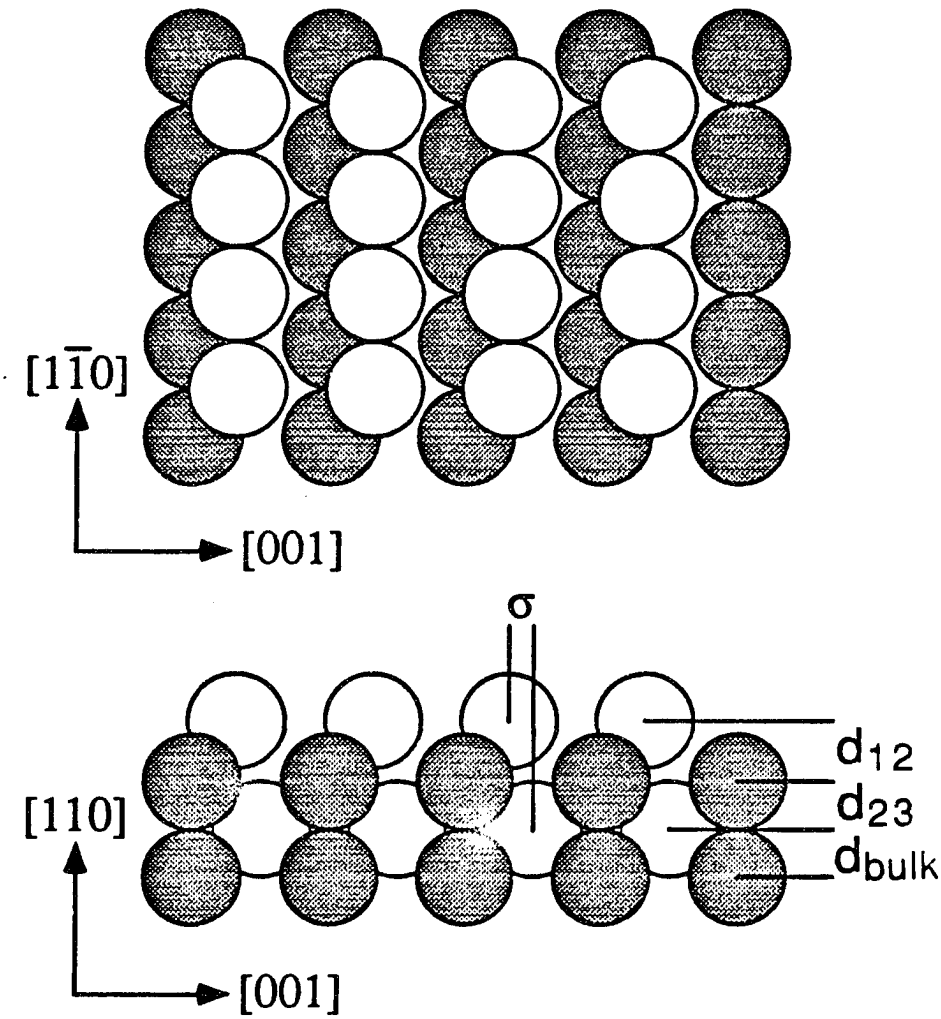


Figure 2. Schematic of Pd(110) exhibiting a rigid registry shift along the [001] direction in the topmost layer

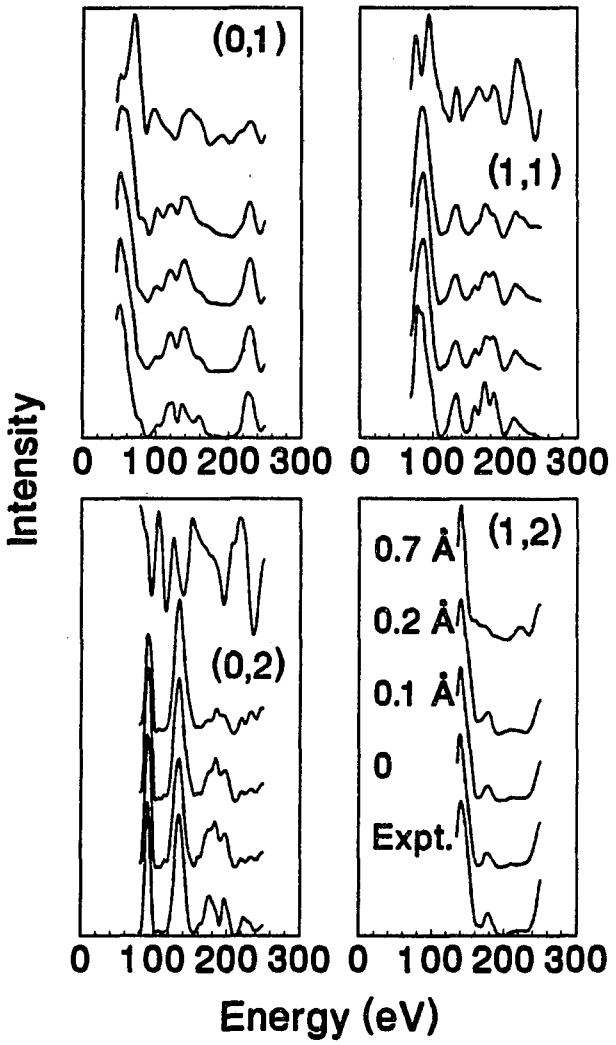


Figure 3. Representative comparison between experimental I(E) curves and best-fit theoretical I(E) curves for $\sigma$ =0, 0.1, 0.2, and 0.7 Å Note the wide range of response with respect to $\sigma$.

($r_p$ =0.238) clearly exceeds this value; thus, by interpolation, we estimate that the upper limit for $\sigma$ is ca. 0.13 Å, which is considerably smaller than the value of 0.7 Å required to account for the He-atom diffraction results of Francis and Richardson. In fact, when $\sigma$ is increased to 0.7 Å, the minimum r factor increases to an extremely poor value ($r_p$ =0.709). As for the interlayer spacings, we find that $d_{12}$ =1.31±0.02 Å and $d_{23}$ =1.39±0.02 Å, which corresponds to a contraction of (4.4±1.5)% in $d_{12}$ and an expansion of (1.5±1.5)% in $d_{23}$ relative to the bulk interlayer spacing of 1.37 Å. Within the uncertainties, both $d_{12}$ and $d_{23}$ are found to be in agreement with the previously mentioned results of Diehl et al. (5) and Skottke et al. (6). Changes in deeper interlayer spacings are not studied since they are most likely smaller than their associated uncertainties.

The rather large uncertainty in $\sigma$ can be attributed in part to momentum transfer being primarily normal to the surface in the normal-incidence configuration (14). LEED's far greater sensitivity to vertical parameters relative to lateral parameters at normal incidence is demonstrated by our results for $\sigma$ =0.2 Å. Although $\sigma$ =0.2 Å clearly exceeds the upper limit established in our analysis, optimum interlayer spacings for this value of $\sigma$ differ by no more than 0.02 Å relative to those obtained for $\sigma$ =0. While the use of the normal-incidence configuration surely diminishes LEED's sensitivity to lateral parameters, we find that domain averaging exerts an even larger effect. As shown in Fig. 4, theoretical I(E) curves for the best-fit $\sigma$ =0.1 Å geometry differ considerably from theoretical I(E) curves for the optimum geometry prior to domain averaging, but only marginally after domain averaging.

Finally, we comment on the possible existence of an order-disorder

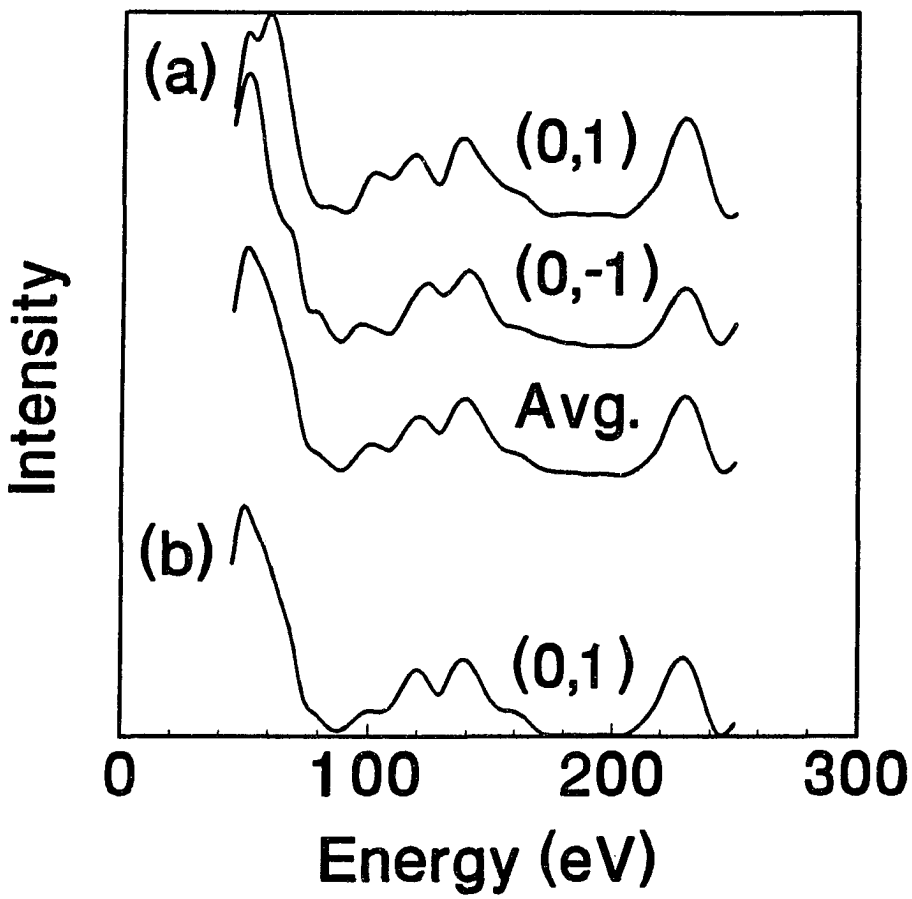


Figure 4. Effect of domain averaging

a) Theoretical I(E) curves for the (0,1) and (0,-1) beams of a single orientational domain of the best-fit $\sigma$ =0.1 Å geometry and their average.

b) Theoretical I(E) curve for the (0,1) beam of the optimum geometry.

transition on Pd(110) near 250 K. Although we cannot claim that we have reached a definitive conclusion concerning the absence or presence of lateral displacements, the fact that lateral displacements of the magnitude required to account for the He-atom diffraction results of Francis and Richardson are clearly not present indicates that if an order-disorder transition does exist, then it is of a far more subtle nature. Since I(E) curves collected above and below the proposed transition temperature do not differ significantly, we believe that the upper limit of ca. 0.13 Å for $\sigma$ is also valid for a laterally disordered surface. As has been previously pointed out, the use of rigid registry shifts to model random lateral displacements is a good approximation due to the fact that the extent of intralayer multiple scattering is relatively small (15).

## V. ACKNOWLEDGEMENTS

This work is supported by the National Science Foundation through Grant No. CHE-9014214. We thank R.J. Baird and G.W. Graham of Ford Motor Company for the use of their Pd(110) crystal. We also thank M.A. Van Hove for supplying the LEED package and phase shifts. O.L.W. acknowledges support from the Amoco Foundation, and P.A.T. acknowledges support from NSF Grant No. CHE-9024358, and from the Camille and Henry Dreyfus Foundation. Some equipment and all facilities are provided by the Ames Laboratory, which is operated for the U.S. Department of Energy by Iowa State University under Contract No. W-7405-ENG-82.

## VI. REFERENCES


1. S.M. Francis and N.V. Richardson, Phys. Rev. B 33 (1986) 662.
2. M. Wolf, A. Goschnick, J. Loboda-Cacković, M. Grunze, W.N. Unertl and J.H. Block, Surf. Sci. 182 (1987) 489.
3. M. Guillopé and B. Legrand, Surf. Sci. 215 (1989) 577.
4. A.M. Lahee, J.P. Tonnies and Ch. Wöll, Surf. Sci. 191 (1987) 529.
5. R.D. Diehl, M. Lindroos, A. Kearsley, C.J. Barnes and D.A. King, J. Phys. C 18 (1985) 4069.
6. M. Skottke, R.J. Behm, G. Ertl, V. Penka and W. Moritz, J. Chem. Phys. 87 (1987) 6191.
7. R. Raval, S. Haq, M.A. Harrison, G. Blyholder and D.A. King, Chem. Phys. Lett. 167 (1990) 391.
8. G. Kleinle, M. Skottke, V. Penka, G. Ertl, R.J. Behm and W. Moritz, Surf. Sci. 189/190 (1987) 177; H. Niehus, C. Hiller and G. Comsa, Surf. Sci. 173 (1986) L599.
9. J. Goschnick, M. Wolf, M. Grunze, W.N. Unertl, J.H. Block and J. Loboda-Cacković, Surf. Sci. 178 (1986) 831.
10. J.R. Noonan and H.L. Davis, in: Determination of Surface Structure by LEED, Eds. P.M. Marcus and F. Jona (Plenum, New York, 1984) p. 449.
11. M.A. Van Hove and S.Y. Tong, Surface Crystallography by LEED (Springer, Berlin, 1979).
12. V. Moruzzi, J. Janak and A. Williams, Calculated Electronic Properties of Metals (Pergamon, New York, 1978).
13. J.B. Pendry, J. Phys. C 13 (1980) 937.
14. M.A. Van Hove, W.H. Weinberg and C.-M. Chan, Low-Energy Electron

Diffraction (Springer, Berlin, 1986).

15. D.G. Kelly, R.F. Lin, M.A. Van Hove and G.A. Somorjai, Surf. Sci. 224 (1989) 97.

PAPER II:

# DETERMINATION OF (1X1) AND (1X2) STRUCTURES OF Pt THIN FILMS ON Pd(110) BY DYNAMICAL LOW-ENERGY ELECTRON-DIFFRACTION ANALYSIS

# Determination of (1X1) and (1x2) Structures of Pt Thin Films on Pd(110) by Dynamical Low-Energy Electron-Diffraction Analysis

O.L. Warren, H.-C. Kang, P.J. Schmitz, and P.A. Thiel
Department of Chemistry and Ames Laboratory
Iowa State University
Ames, Iowa 50011

P. Kaukasoina and M. Lindroos
Tampere University of Technology
P.O. Box 527, SF-33101
Tampere, Finland

## ABSTRACT

Geometric structures of (1x1) and (1x2) Pt thin films on Pd(110) have been determined by dynamical low-energy electron-diffraction analysis. The (1x1) structure exhibits relaxations in the first two interlayer spacings of $\Delta d_{12}$ =-11.0% and $\Delta d_{23}$ =6.6% at a Pt coverage of one monolayer, and relaxations of $\Delta d_{12}$ =-6.6% and $\Delta d_{23}$ =4.4% at two monolayers. As for the (1x2) structure, the top three layers are Pt. The topmost layer is of the missing-row type, the second layer is slightly row paired (0.06 Å), and the third layer is significantly rumpled (0.23 Å). Relaxations in the first four interlayer spacings are $\Delta d_{12}$ =-9.5%, $\Delta d_{23}$ =-8.0%, $\Delta d_{34}$ =-7.3%, and $\Delta d_{45}$ =2.2%. Except for a significantly less contracted first interlayer spacing, the (1x2) structure of the Pt film mimics the (1x2) structure of bulk Pt(110).

# I. INTRODUCTION

The (110) face of bulk Pt is known to reconstruct. The two most commonly observed periodicities–(1x2) and (1x3)– have been shown to correspond to geometries of the missing-row type (1-3). The clean surface of Pd(110), on the other hand, is known to be stable with respect to reconstruction (4-6). Thus, a Pt film on Pd(110) represents a reconstructive film grown atop a nonreconstructive substrate. Since the lattice mismatch is only 0.8% (7), one would not expect this factor to play a major role in determining the film structure or growth mode, at least for the first few layers (8).

Recently, we have observed (1x1), (1x2), and (1x3) low-energy electron-diffraction (LEED) patterns for Pt thin films grown on Pd(110) (9,10). Conditions required to produce each LEED pattern are as follows. For Pt coverages $\leq$1 ML, only a (1x1) LEED pattern is observed. [A Pt coverage of one monolayer (ML) is defined as the atomic density of the Pd(110) surface.] A (1x1) LEED pattern is also observed for Pt coverages greater than 1 ML, but only if the films are deposited and maintained at low temperature. Upon annealing, these films exhibit a streaky LEED pattern for Pt coverages between 1 and 2 ML, and either a (1x2) or a (1x3) LEED pattern for Pt coverages $\geq$2 ML. All films are unstable with respect to extensive dissolution if annealed to a sufficiently high temperature (9,10), which is consistent with the fact that Pt and Pd are known to be continuously miscible in the solid state (11).

Interestingly, two specific conditions must be met to produce the (1x2) structure. First, the (1x2) structure develops only at 2 ML;

slightly lower coverages result in no distinct superstructure and slightly higher coverages result in the (1x3) structure. Second, the formation of the (1x2) structure at 2 ML requires that Pt be deposited at temperatures less than 200 K; higher deposition temperatures result in the (1x3) structure. This is particularly surprising since relatively high annealing temperatures are required to form either superstructure. We have investigated the possibility that the peculiarity at 2 ML is the result of temperature-dependent contamination (9), but have concluded that this is unlikely; furthermore, one would expect contamination to exert a similar effect at higher coverages. Therefore, we believe that the peculiarity is caused instead by a strong temperature dependence in the morphology of the film prior to annealing.

The similarity between the periodicities observed for the (110) face of bulk Pt and those we observe here suggests that the two systems share a common origin, i.e., the (1x2) and (1x3) structures of the Pt films are reconstructions of the missing-row type. This hypothesis is supported by the fact that exposing either the (1x2) or the (1x3) structure of the Pt films to CO "lifts" the reconstruction (9,10), which is also known to occur on the corresponding bulk Pt surfaces (3,12).

In this paper, we present the results of a dynamical LEED study, in which we have investigated the (1x1) structure at 1 ML, the (1x1) structure at 2 ML, and the (1x2) structure of Pt on Pd(110). While LEED has been used extensively in obtaining detailed structural information for clean and adsorbate-induced reconstructions of bulk fcc(110) surfaces, here we report on a structural determination by LEED for a reconstructed fcc(110) thin film.

# II. EXPERIMENTAL PROCEDURES

Experiments are performed in a stainless-steel ultrahigh-vacuum chamber (base pressure $\leq 1 \times 10^{-10}$ torr) equipped with a single-pass cylindrical mirror analyzer for Auger electron spectroscopy (AES); quadrupole mass spectrometer; $\mu$-metal-shielded, display-type, four-grid LEED optics; sputter gun; provisions for gas exposure; and a metal evaporator for Pt deposition. The Pd(110) crystal is cleaned by cycles of $Ar^+$ bombardment at 300 K and annealing at 1100 K until impurities, with the possible exception of carbon, are reduced to the noise level of AES. Since carbon levels are difficult to ascertain by AES due to the overlap of the carbon 272-eV and Pd 279-eV Auger signals, cycles of oxygen exposure at 640 K to remove carbon as carbon oxides and flashes to 1100 K to desorb residual oxygen are performed. Carbon levels are considered to be sufficiently low when thermal desorption spectra for the CO-saturated surface are consistent with those previously reported for a carbon-free surface (13). Cleaning in the above manner results in a surface that exhibits a high-quality (1x1) LEED pattern.

Pt is deposited at 105 K, at a rate of ca. 1 ML $min^{-1}$. After deposition, the LEED pattern is (1x1) and no impurities are detected by AES. Relative Pt coverage is determined by measuring $R_{Pt/Pd}$, which is defined as the ratio of the peak-to-peak Auger signals for Pt (64 eV) and Pd (330 eV); 2-keV primary beam energy and 1-V peak-to-peak modulation voltage are used in AES work. Measurements of $R_{Pt/Pd}$ at various sample positions indicate that the films are spatially uniform to within ±5%. Figure 1 shows that linear segments and equidistant breaks characteristic

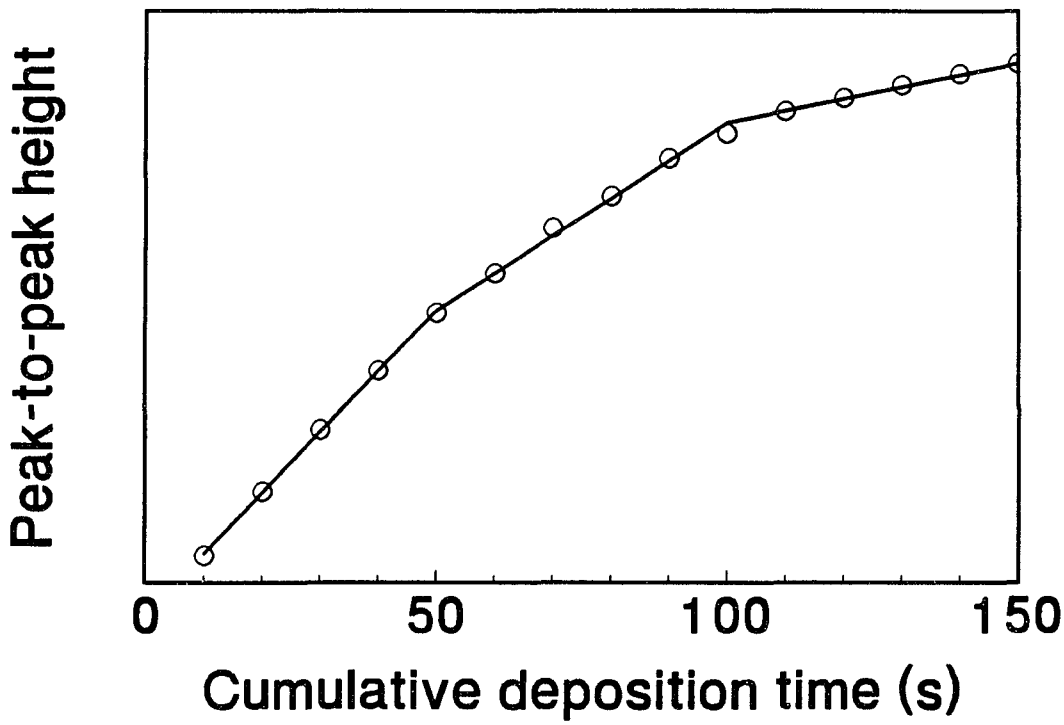


Figure 1. Peak-to-peak height of the Pt 64-eV AES signal vs cumulative deposition time

Deposition and AES measurements are performed at 105 K.

of layer-by-layer growth (14) are observed in a plot of the Pt 64-eV peak-to-peak height versus cumulative deposition time. Values obtained for $R_{Pt/Pd}$ at the first (0.30) and second (0.75) break points, or at 1 and 2 ML, are found to be in excellent agreement with those reported previously for the first two monolayers of Pt on Pd(100) based on the characterization of coverage-dependent Bragg-intensity oscillations (15).

The (1x1) films are not annealed to ensure that only the (1x1) phase is present. LEED patterns for 1- and 2-ML films are not as good as that of the clean substrate, but are of sufficient quality to acquire reliable intensity-energy [I(E)] curves, i.e., no serious loss of low-intensity features is observed. Of the two, the LEED pattern for the 2-ML film is worse due to slightly higher background intensity and visibly detectable oscillations in spot size with beam energy. Although still visible, LEED patterns at higher coverages are degraded to the extent that an analysis is not warranted.

The (1x2) structure is produced by annealing the 2-ML film at 530 K. This procedure results in a bright, low-background LEED pattern with comparable integral and half-order intensities, although as shown in Fig. 2, half-order beams remain rather broad along the [001] direction. Neither impurities nor loss of Pt are detected by AES after annealing.

Experimental I(E) curves are acquired at normal incidence with a computer-interfaced video processor and a silicon-intensified-target camera. The crystal is maintained at 105 K. Background subtraction is performed locally during data collection, and beam-current normalization is performed separately after measuring the current as a function of beam energy with the crystal biased sufficiently positive to suppress secondary

Figure 2. (1x2) LEED pattern at 70 eV
(0,1/2), (0,1), (1,0), (1,1/2), and (1,1) beam sets are visible. Note the elongation of the half-order beams along the [001] direction.

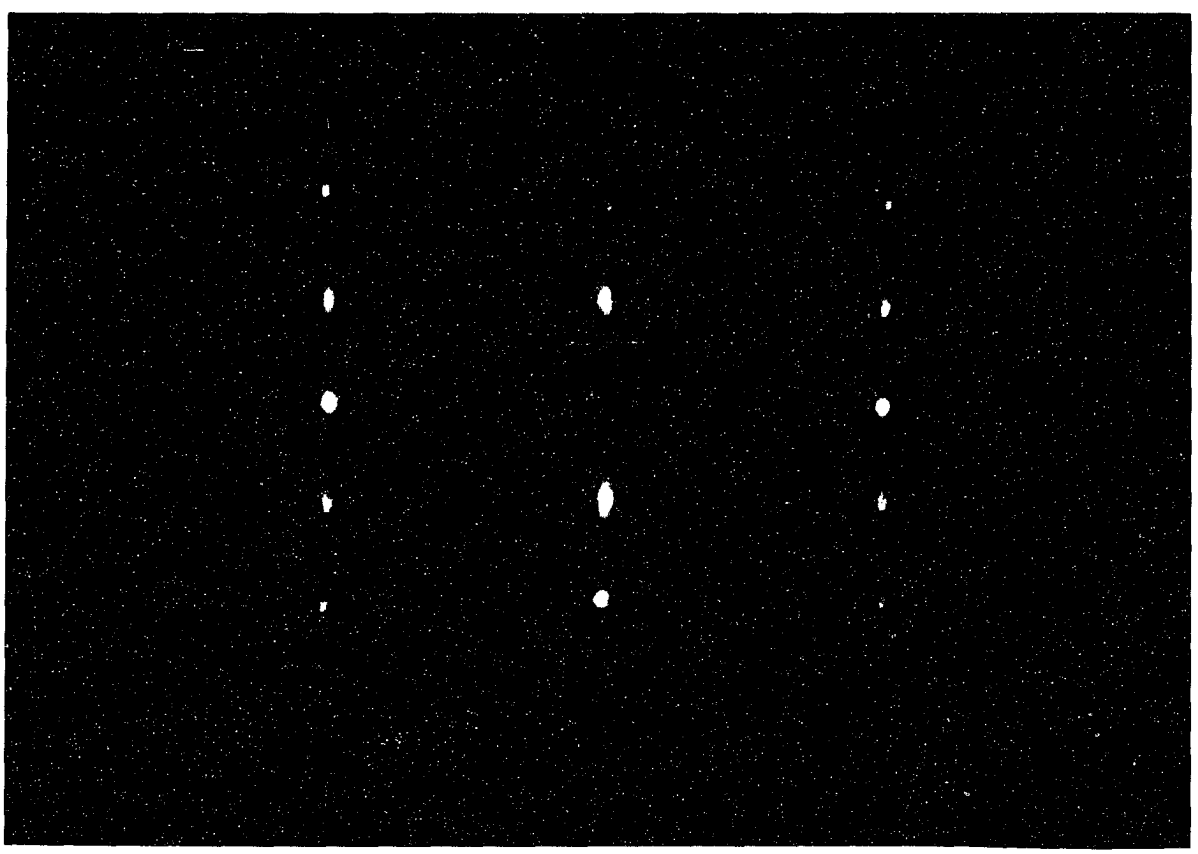

emission. Equivalent beam averaging—a procedure known to minimize residual experimental errors (16)— is performed when possible. Eight symmetry-nonequivalent curves over the energy range of 50-250 eV are available for each of the (1x1) films, and nine symmetry-nonequivalent curves (five integral-order, four half-order) over the energy range of 30-300 eV are available for the (1x2) structure. Truncation of curves prior to the maximum energy is due to either manipulator shadowing or the inability to track the beam over an extended energy range of low intensity.

Normal incidence is determined by comparing symmetry-equivalent I(E) curves. In particular, the (1,1) beam set of the (1x2) LEED pattern is found to be extremely sensitive to misalignment. Figure 3 shows that while curves collected at normal incidence are in excellent agreement, a small deliberate misalignment results in substantial differences. However, the merit of equivalent beam averaging is readily apparent by noting the close similarity between averaged curves.

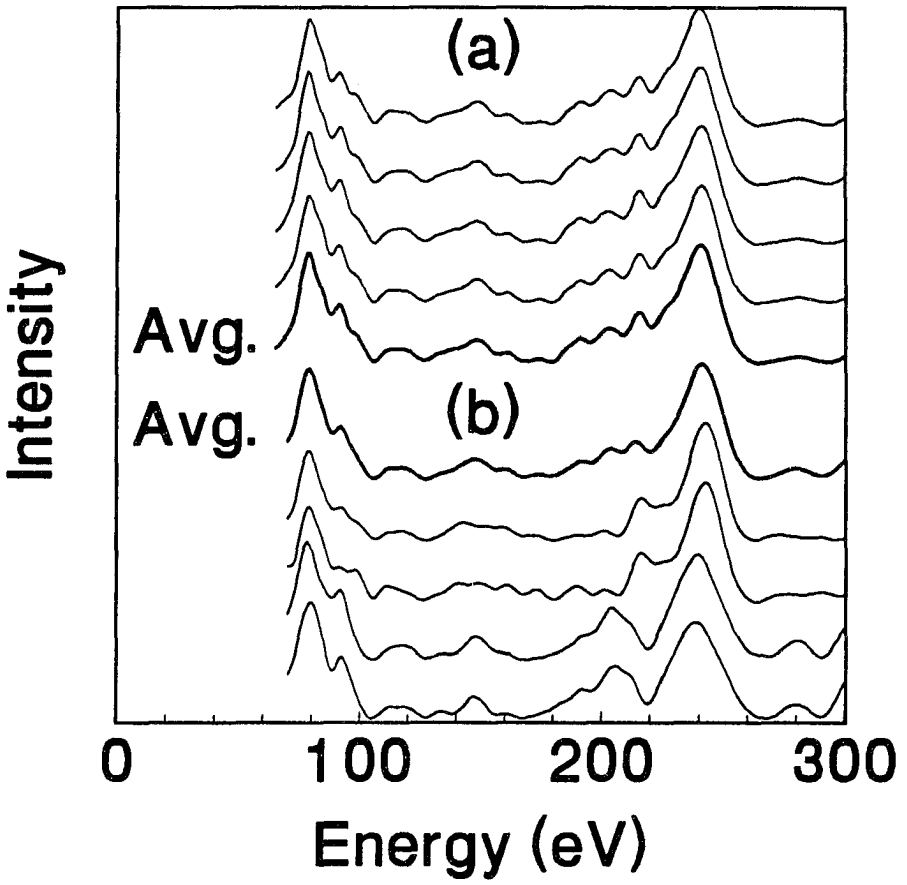


Figure 3. Experimental I(E) curves and their average for the (1,1) beam set of the (1x2) LEED pattern

a) At normal incidence. From top to bottom, beam indices are (-1,1), (-1,-1), (1,-1), and (1,1).

b) As in a), but for 0.5° off-normal incidence.

Note the close similarity between averaged curves.

# III. COMPUTATIONAL PROCEDURES

Theoretical I(E) curves are calculated for normal incidence with the LEED package of Van Hove and Tong (17). After calculating reflection and transmission matrices within the self-consistent formalism, interlayer scattering is accomplished by layer doubling. The combined space method for composite layers with matrix inversion is employed when small spacings between subplanes are involved. Random substitutional disorder is studied with the average T-matrix approximation (ATA) (18), which has been shown to yield calculationally correct results (19). Domain averaging is carried out for (1x2) structural models with only one mirror plane.

Eight phase shifts ($\ell_{max}$ =7) are used throughout in the (1x1) analysis. Pd phase shifts are calculated from the tabulated potential of Moruzzi, Janak, and Williams (20), and spin-averaged Pt phase shifts are calculated from the potential of Wang (21). The phase shifts are temperature corrected with an effective Debye temperature ($\theta_D$) of 230 K for Pd and 195 K for Pt. Up to nine phase shifts ($\ell_{max}$ =8) are included in the (1x2) analysis. Pd phase shifts are calculated from the potential described above, and spin-averaged Pt phase shifts are calculated from the potential of Mattheiss (22). The phase shifts are temperature corrected with a $\theta_D$ of 195 for Pd and 160 K for Pt. The real part of the optical potential ($V_{or}$) is treated as a constant over the entire energy range, and is shifted in 1-eV steps during reliability-factor (r-factor) analysis to obtain the best level of agreement. The final value of $V_{or}$ is -6 eV for all three structures. The imaginary part of the optical potential ($V_{oi}$) is fixed at -5 eV in the (1x1) analysis, and at -4 eV in the (1x2) analysis.

No further steps are taken to improve the level of agreement through the values of the nonstructural parameters since such steps generally have little influence on the final structural result (23).

Theoretical and experimental I(E) curves are compared quantitatively with the Pendry r factor ($r_p$) (24). Since this r factor is highly sensitive to spectral noise (24), both sets of curves are smoothed prior to r-factor analysis.

# IV. (1x1) RESULTS

In the analysis of the (1x1) structures, we consider only overlayer geometries, since complications due to intermixing seem unlikely in light of the fact the (1x1) films are deposited and maintained at low temperature. The number of Pt layers is, however, considered as a variable in order to test our Pt coverage assignments based on the AES plot shown in Fig. 1. An acceptable fit between theory and experiment for both 1- and 2-ML films will confirm that a significant degree of layer-by-layer quality is indeed achieved for the first two monolayers of film growth (25).

Results are summarized in Table 1. Initially, the relaxation of the first interlayer spacing is considered for zero to three Pt layers. From the r-factor results, it is clear that 1- and 2-ML films are best described by one and two Pt layers, respectively. Optimum first interlayer spacings and minimum r factors for one-layer relaxation are as follows: $d_{12}$ =1.25 Å and $r_P$ =0.39 for the 1-ML film; $d_{12}$ =1.31 Å and $r_P$ =0.35 for the 2-ML film.

Next, the (1x1) structures are further refined by considering relaxations in the first two interlayer spacings. Optimum first and second interlayer spacings and minimum r factors for two-layer relaxation are as follows: $d_{12}$ =1.22 Å, $d_{23}$ =1.46 Å, and $r_P$ =0.27 for the 1-ML film; $d_{12}$ =1.28 Å, $d_{23}$ =1.43 Å, and $r_P$ =0.30 for the 2-ML film. Differences in the interlayer spacings relative to the truncated substrate geometry are as follows: $\Delta d_{12}$ =-11.0% and $\Delta d_{23}$ =6.6% for the 1-ML film; $\Delta d_{12}$ =-6.6% and $\Delta d_{23}$ =4.4% for the 2-ML film. As expected, by allowing $d_{23}$ to expand from the Pd(110) bulk interlayer spacing of 1.37 Å, a further contraction in $d_{12}$ is found for both films (26). Based on Pendry's (24) definition of the

Table 1. Results of the (1x1) analysis

Dash indicates that the parameter is not varied.

| ML | No. of Pt layers | Optimum parameters (Å) | | |
|---|---|---|---|---|
| (expt.) | (theory) | $d_{12}$ | $d_{23}$ | Pendry r factor |
| 1 | 0 | 1.33 | - | 0.61 |
| 1 | 1 | 1.25 | - | 0.39 |
| 1 | 2 | 1.34 | - | 0.52 |
| 1 | 3 | 1.36 | - | 0.61 |
| 2 | 0 | 1.35 | - | 0.61 |
| 2 | 1 | 1.38 | - | 0.57 |
| 2 | 2 | 1.31 | - | 0.35 |
| 2 | 3 | 1.32 | - | 0.52 |
| 1 | 1 | 1.22 | 1.46 | 0.27 |
| 2 | 2 | 1.28 | 1.43 | 0.30 |

variance, an uncertainty of ca. ±0.03 Å (±2%) is associated with each interlayer spacing. Changes in deeper interlayer spacings are not considered since they are most likely smaller than their associated uncertainties. For instance, while a first-principles calculation for a single (1x1) layer of Au on Ag(110) predicts relaxations in the first two interlayer spacings comparable to those found for the 1-ML Pt film ($\Delta d_{12}$ =-11.9%, $\Delta d_{23}$ =5.5%), it predicts only a negligible relaxation in the third interlayer spacing ($\Delta d_{34}$ =-0.7%) (27). Contour maps of $r_p$ as a function of the first two interlayer spacings are shown in Fig. 4. Experimental and best-fit theoretical I(E) curves are visually compared in Figs. 5 and 6.

Pendry r factors obtained for both films are somewhat higher than the values of less than 0.20 typically expected for clean surfaces of unreconstructed metals, which could be due in part to surface roughness. [Although it should be noted that such low values are generally not achieved for high-Z metals such as Pt, e.g., a Pendry r factor of only 0.50 was reported for the clean surface of Pt(111)-(1x1) (28).] As mentioned previously, LEED patterns for both films are poorer than that of the clean substrate, and oscillations in spot size with beam energy are detected in the case of the 2-ML film, which indicates the presence of random steps (29). The presence of steps has been previously implicated as a cause for degrading the level of agreement in LEED analysis (30). Despite the apparent deviation from ideality, the predominant ordered component of the 1- and 2-ML films is clearly shown to be one and two layers thick, respectively, which confirms that film growth at low temperature occurs in at least a pseudo-layer-by-layer fashion for the first two monolayers, i.e., the interface width is considerably narrower than predicted by

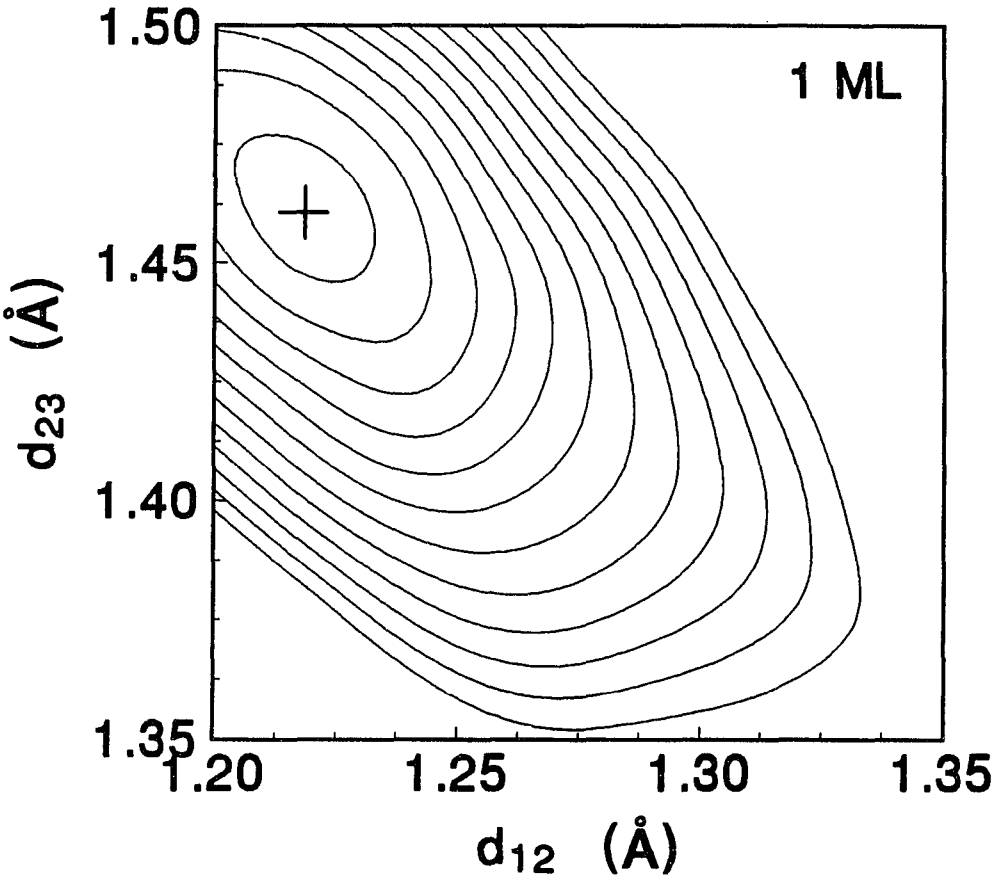


Figure 4. Pendry r-factor contour maps for the (1x1) structures
The innermost contour corresponds to $r_p$ =0.28 in the 1-ML map, and to $r_p$ =0.31 in the 2-ML map. Each successive contour corresponds to an increase in $r_p$ of 0.02.

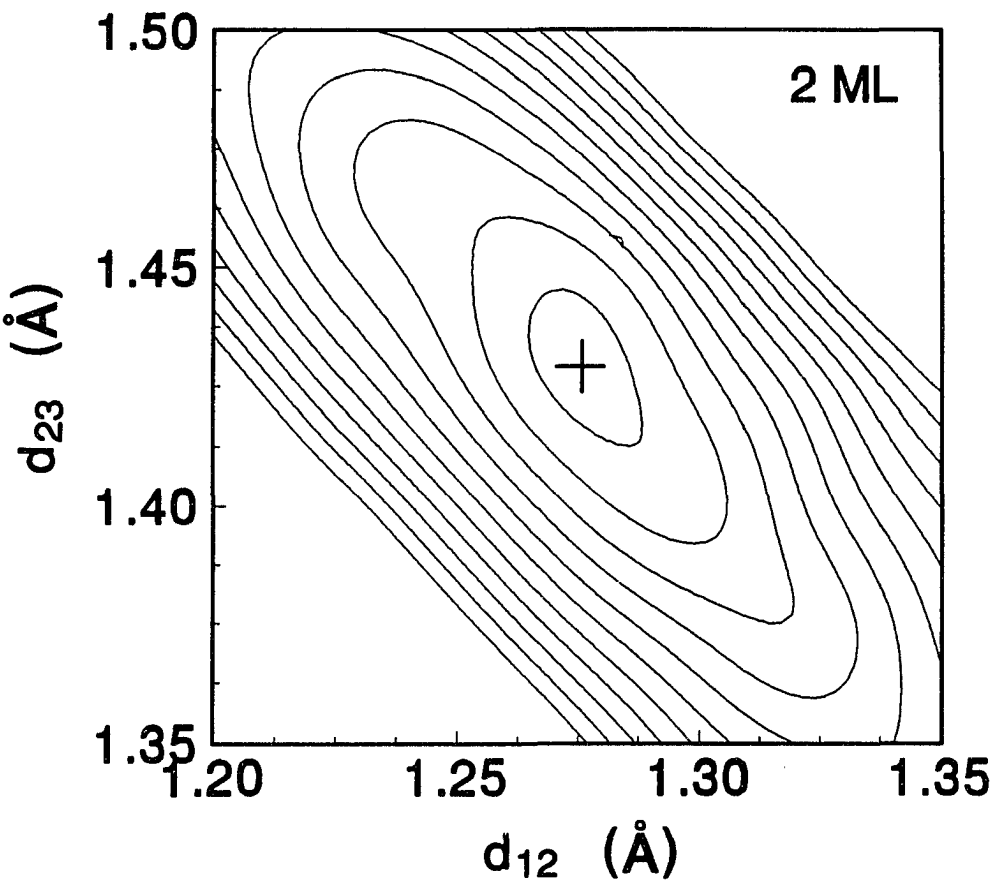


Figure 4. (Continued)

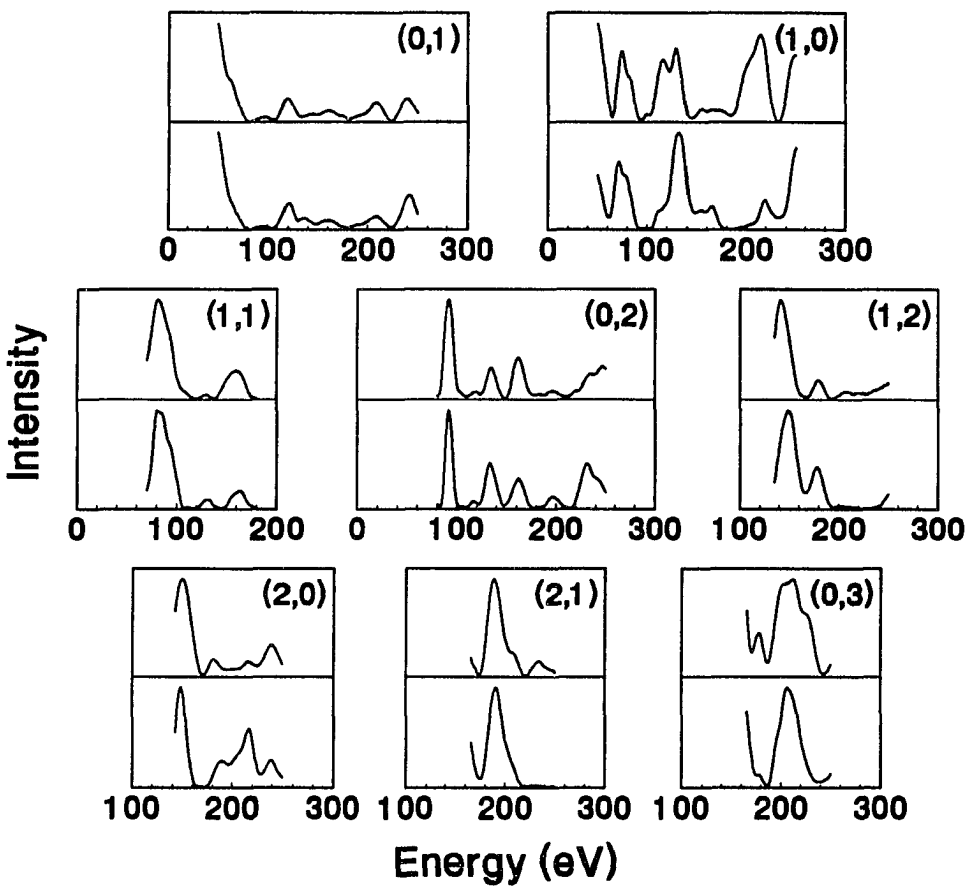


Figure 5. Experimental and best-fit theoretical I(E) curves for the (1x1) structure at 1 ML

Upper curves correspond to theory.

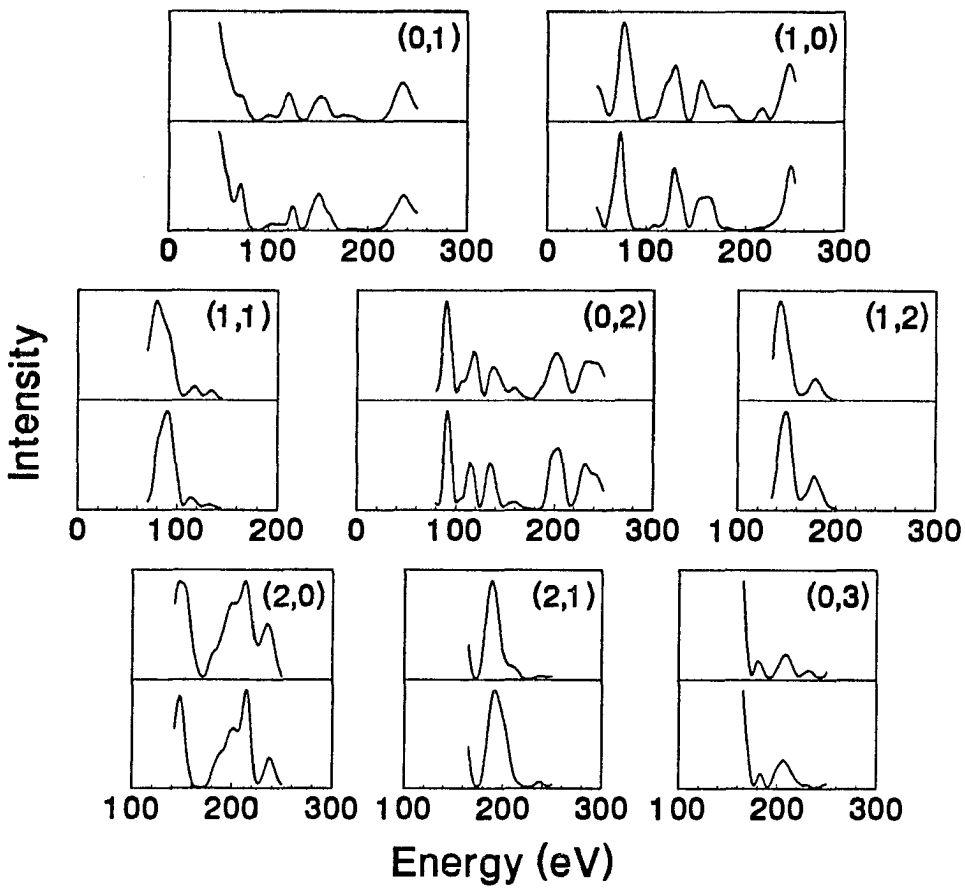


Figure 6. Experimental and best-fit theoretical I(E) curves for the (1x1) structure at 2 ML

Upper curves correspond to theory.

Poisson statistics. This behavior has also been observed for low-temperature growth of Pt on Pd(100) (31). For statistically random deposition on an fcc(100) substrate, it has been demonstrated that diffusionless pseudo-layer-by-layer growth is feasible, with the stipulation that adsorption can occur only in fourfold hollow sites (32). An analogous explanation may apply here.

# V. (1x2) RESULTS

In the analysis of the (1x2) structure, we focus primarily on missing-row-type models. However, paired-row, rumpled-surface, and sawtooth (33) models are also tested since the electronic influence of the Pd substrate may induce a reconstruction different from that of bulk Pt. Descriptions of these models can be found in Ref. 34. Since the ideal coverage of the (1x2) phase is not exactly known experimentally, the number of Pt layers is treated as a variable. In addition, the possibility of intermixing is considered for the (1x2) structure since its formation requires a relatively high annealing temperature. Structural parameters—interlayer spacings ($d_{12}$-$d_{45}$), extent of pairing ($\sigma$), and extent of rumpling ($\delta$)— are defined in Fig. 7 for the missing-row model with second-layer row pairing and third-layer rumpling. These parameters are similarly defined for models not shown.

First, overlayer models are considered. Results for these models are summarized in Table 2. Correctness of a missing-row topmost layer is clearly demonstrated by the r-factor results for models 1-4. The missing-row model yields the lowest r factor (0.54) when compared to paired-row (0.75), rumpled-surface (0.65), and sawtooth (0.77) models. The missing-row model is also preferred when partial r factors for integral and half-order beams are taken separately into account. Since the optimum pairing in the paired-row model corresponds to the situation with no pairing, the partial r factor for the half-order beams is estimated to be 1. Although the number of Pt layers is fixed at three at this stage of the analysis, we believe that models 2-4 can be excluded from further consideration. [A

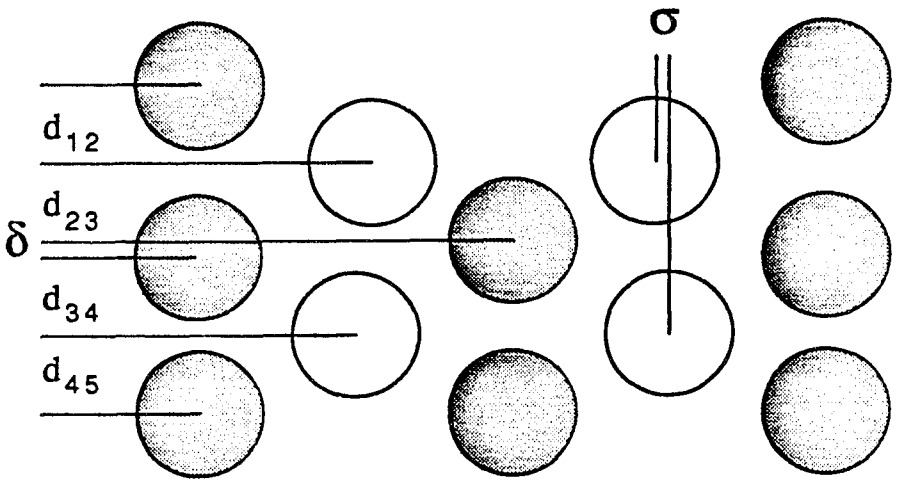


Figure 7. Schematic of the missing-row model with second-layer row pairing and third-layer rumpling

Sign conventions for pairing ($\sigma$) and rumpling ($\delta$) are as follows: positive pairing corresponds to pairing towards the missing row, and negative rumpling corresponds to the situation where the upper atom in the rumpled layer is directly beneath the missing row. The schematic is drawn to exhibit positive pairing and negative rumpling.

Table 2. Results for (1x2) overlayer models

Missing-row model with second-layer row pairing and third-layer rumpling is denoted as M+P+R. Missing-row model with rumpling in the second layer is denoted as M+R. Dash indicates that the parameter is either not relevant to the model under consideration or is not varied.

| Model | No. of Pt layers (theory) | Optimum parameters (Å) | | | | | | Pendry r factor | | |
|---|---|---|---|---|---|---|---|---|---|---|
| | | $d_{12}$ | $d_{23}$ | $d_{34}$ | $d_{45}$ | $\sigma$ | $\delta$ | Integral | Half | Total |
| 1 Missing-row | 3 | 1.27 | 1.59 | 1.21 | 1.40 | - | - | 0.47 | 0.64 | 0.54 |
| 2 Paired-row | 3 | 1.29 | 1.53 | 1.28 | 1.44 | 0.00 | - | 0.52 | 1.00 | 0.75 |
| 3 Rumpled-surface | 3 | 1.19 | 1.41 | 1.41 | 1.38 | - | -0.16 | 0.52 | 0.79 | 0.65 |
| 4 Sawtooth | 3 | 1.26 | 1.18 | 1.25 | - | - | - | 0.75 | 0.78 | 0.77 |
| 5 Missing-row | 0 | 1.24 | 1.21 | 1.54 | 1.39 | - | - | 0.52 | 0.58 | 0.55 |
| 6 Missing-row | 1 | 1.30 | 1.26 | 1.44 | 1.38 | - | - | 0.57 | 0.63 | 0.60 |
| 7 Missing-row | 2 | 1.20 | 1.35 | 1.42 | 1.38 | - | - | 0.56 | 0.64 | 0.60 |
| 8 M+P+R | 0 | 1.25 | 1.21 | 1.44 | 1.39 | -0.19 | -0.09 | 0.53 | 0.53 | 0.53 |
| 9 M+P+R | 1 | 1.27 | 1.25 | 1.36 | 1.37 | 0.09 | -0.07 | 0.57 | 0.57 | 0.57 |
| 10 M+P+R | 2 | 1.19 | 1.32 | 1.35 | 1.36 | 0.08 | -0.10 | 0.52 | 0.59 | 0.55 |
| 11 M+P+R | 3 | 1.24 | 1.26 | 1.27 | 1.40 | 0.06 | -0.23 | 0.30 | 0.35 | 0.32 |
| 12 M+P+R | 4 | 1.22 | 1.28 | 1.29 | 1.37 | -0.01 | -0.23 | 0.58 | 0.45 | 0.52 |
| 13 M+R | 3 | 1.26 | 1.58 | 1.21 | 1.40 | - | -0.02 | 0.47 | 0.64 | 0.54 |

film thickness of N layers corresponds to an ideal coverage of (N-0.5) ML for the missing-row model, (N-1) ML for the sawtooth model, and N ML for paired-row and rumpled-surface models.]

The r factor for the missing-row model is, however, still rather poor; thus, the sensitivity of LEED with respect to the number of Pt layers is tested in models 5-7. While r factors for one (0.60) and two (0.60) layers are worse, it is somewhat disturbing that the same level of agreement is achieved for zero (0.55) and three (0.54) layers. The failure to identify the number of Pt layers suggests that the missing-row model is not a complete description of the reconstruction. Although the first LEED analysis of bulk Pt(110)-(1x2) favored the missing-row model, the results were not conclusive due to an incomplete account of the full extent of the reconstruction (35). Subsequent LEED analyses have shown that an extension of the reconstruction to subsurface layers in the form of alternating row pairing and rumpling is necessary to obtain an acceptable fit between theory and experiment (2,3). Thus, the missing-row model is extended to include these features, with the number of Pt layers remaining as a variable.

In models 8-12, the effect of row pairing in the second layer and rumpling in the third layer is studied for zero to four Pt layers. While r factors for zero, one, two, and four layers remain above 0.50, a significantly improved r factor (0.32) is achieved for three layers (model 11). Comparable partial r factors are obtained for integral (0.30) and half-order (0.35) beams.

While pairing in the second layer of model 11 is found to be only slight ($\sigma$ =0.06 Å), rumpling in the third layer is found to be significant

($\delta$ =-0.23 Å). It is known that vertical displacements, such as rumpling, exert a large effect on I(E) curves due to momentum transfer being primarily toward the surface normal in the normal-incidence configuration (34). By the same reasoning, I(E) curves are somewhat insensitive to lateral displacements such as row pairing (34). Thus, we conclude that the omission of third-layer rumpling is the principal cause for the above-mentioned failure to identify the number of Pt layers within the (1x2) structure. [Due to the weak effect of row pairing, a missing-row model with three Pt layers and rumpling instead of pairing in the second layer is also tested (model 13); however, the r-factor result for this model (0.54) indicates that this is not a good choice for the position of the rumpled layer.]

Next, intermixing models are considered. Results for these models are summarized in Table 3. Random substitutional disorder within the first four layers of the missing-row model with second-layer row pairing and third-layer rumpling is studied with the ATA method in models 14-17. While the atomic concentration is varied for the layer under consideration, all structural parameters and all other layer compositions are fixed as listed for model 11 in Table 2. The results favor a small amount of Pd in the topmost layer (12%), but this cannot be judged conclusive since the r factor obtained for no intermixing clearly falls within the range of uncertainty.

Since the rumpled layer in model 11 is in direct contact with the substrate, the possibility of a 1:1 ordered alloy in this layer is considered in models 18 and 19. However, after reoptimization of the structural parameters, we find that the r factor increases to 0.44 for Pt

Table 3. Results for (1x2) intermixing models

Structural parameters in the average T-matrix approximation (ATA) models are fixed at the values listed for model 11 in Table 2. M+P+R is defined in Table 2.

| Model | % Pt layer 1 | % Pt layer 2 | % Pt layer 3 | % Pt layer 4 | Optimum % Pt in varied layer | Pendry r factor Integral | Pendry r factor Half | Pendry r factor Total |
|---|---|---|---|---|---|---|---|---|
| 14 ATA | Varied | 100 | 100 | 0 | 88 | 0.29 | 0.35 | 0.32 |
| 15 ATA | 100 | Varied | 100 | 0 | 100 | 0.30 | 0.35 | 0.32 |
| 16 ATA | 100 | 100 | Varied | 0 | 100 | 0.30 | 0.35 | 0.32 |
| 17 ATA | 100 | 100 | 100 | Varied | 0 | 0.30 | 0.35 | 0.32 |

| Model | Upper atom | Lower atom | Optimum parameters (Å) $d_{12}$ | $d_{23}$ | $d_{34}$ | $d_{45}$ | $\sigma$ | $\delta$ | Pendry r factor Integral | Pendry r factor Half | Pendry r factor Total |
|---|---|---|---|---|---|---|---|---|---|---|---|
| 18 M(Pt)+P(Pt)+R(alloy) | Pt | Pd | 1.22 | 1.27 | 1.26 | 1.35 | 0.07 | -0.23 | 0.37 | 0.52 | 0.44 |
| 19 M(Pt)+P(Pt)+R(alloy) | Pd | Pt | 1.19 | 1.33 | 1.25 | 1.35 | 0.05 | -0.21 | 0.43 | 0.55 | 0.48 |

as the upper atom in the rumpled layer, and to 0.48 for Pd as the upper atom in the rumpled layer. A preference for Pt rather than Pd as the upper atom is a further indication that this layer is all Pt.

Finally, combinations of missing-row Pt or (Pd+Pt) in the topmost layer; 2Pt, (Pd+Pt), or (Pt+Pd) in the second and third layers; and 2Pd, (Pd+Pt), or (Pt+Pd) in the fourth layer are tested (results are not listed in Table 3 due to the large number of combinations). The first four interlayer spacings are taken into account, but neither pairing nor rumpling is considered. In all cases, at least the mirror plane perpendicular to the [1$\bar{1}$0] direction is retained as a symmetry element. However, the results again do not favor the presence of ordered alloy layers, e.g., the following combination: (Pd+Pt) in the topmost layer, 2Pt in the second layer, (Pd+Pt) in the third layer, and 2Pd in the fourth layer yields an r factor of 0.56, with partial r factors of 0.44 and 0.72 for integral and half-order beams, respectively.

Thus, we conclude that the missing-row model with second-layer row pairing and third-layer rumpling best describes the (1x2) structure of Pt on Pd(110). Three layers of Pt are present in the reconstructed phase, which corresponds to an ideal coverage of 2.5 ML. Optimum structural parameters and the minimum r factor are as follows: $d_{12}$ =1.24 Å, $d_{23}$ =1.26 Å, $d_{34}$ =1.27 Å, $d_{45}$ =1.40 Å, $\sigma$ =0.06 Å, $\delta$ =-0.23 Å, and $r_p$ =0.32. In the same manner as for bulk Pt(110)-(1x2) (2,3), pairing occurs toward the missing row and the upper atom of the rumpled layer is directly beneath the missing row. The directions of these displacive movements are consistent with reducing the large corrugation of the missing-row reconstruction. Differences in the interlayer spacings relative to the truncated substrate

geometry are as follows: $\Delta d_{12}$ =-9.5%, $\Delta d_{23}$ =-8.0%, $\Delta d_{34}$ =-7.3%, and $\Delta d_{45}$ =2.2%. Plots of $r_p$ as a function of a single structural parameter, with all other parameters fixed near their optimum values, are shown in Fig. 8. Experimental and best-fit theoretical I(E) curves are visually compared in Fig. 9.

The Pendry r factor obtained for the (1x2) structure is comparable to the value of 0.36 reported for bulk Pt(110)-(1x2) (3). Nevertheless, it is unlikely that the (1x2) phase forms a continuous overlayer. For instance, the coverage of the (1x1) film leading to the (1x2) structure upon annealing is 0.5 ML less than the ideal coverage of the (1x2) structure. This suggests that the (1x2) phase occurs as patches with limited spatial extent along the [001] direction–to be consistent with the LEED pattern–with perhaps (1x1) areas of either bare Pd or one-layer thick Pt in between. If the (1x2) phase does exist as patches, then they must cover a large fraction of the surface since comparable integral and half-order intensities are observed. Unfortunately, there is no simple way (if any) to include inhomogeneity in LEED calculations, although it may be possible to improve the level of agreement by mixing in intensities from ordered (1x1) areas. However, such a procedure would not likely affect the final structure obtained for the (1x2) phase.

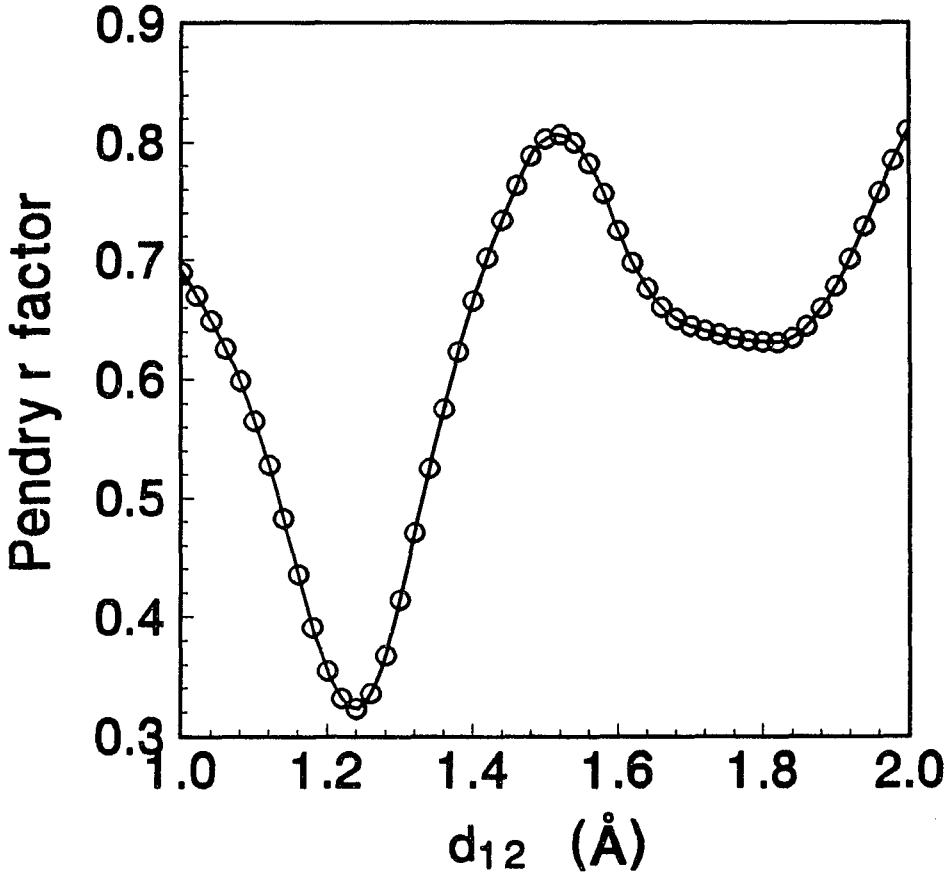


Figure 8. Pendry r-factor sensitivity plots for the (1x2) structure All parameters other than the parameter under consideration are fixed near their optimum values.

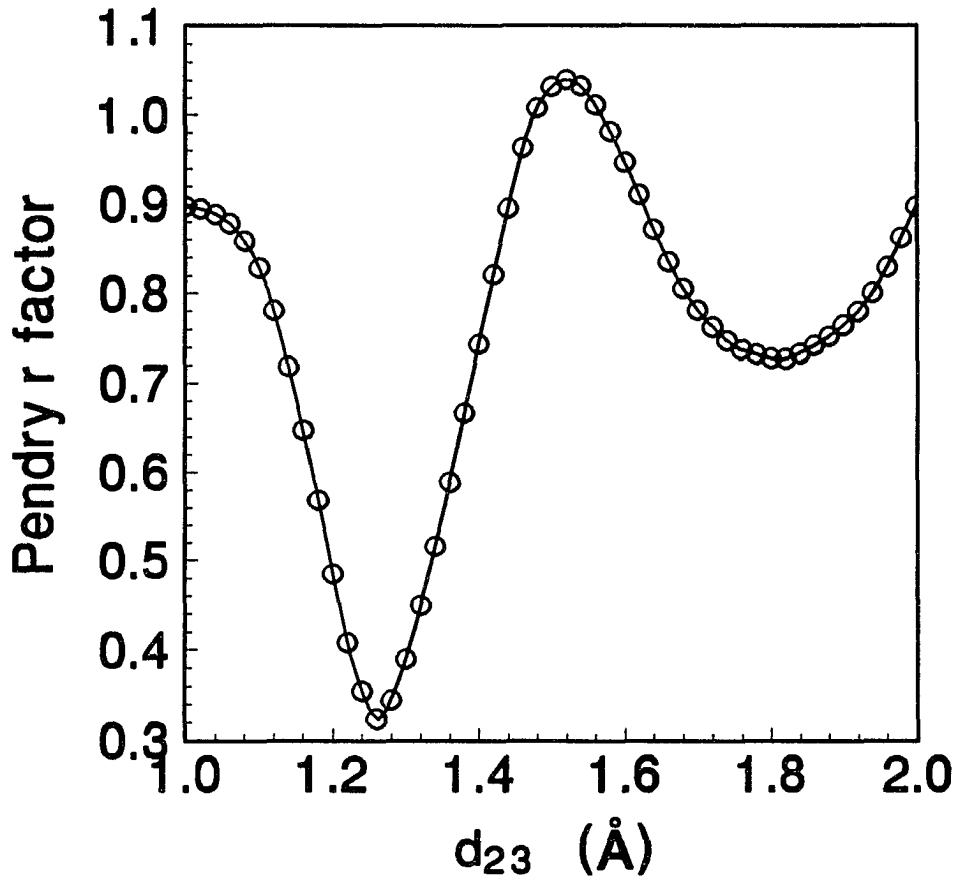


Figure 8. (Continued)

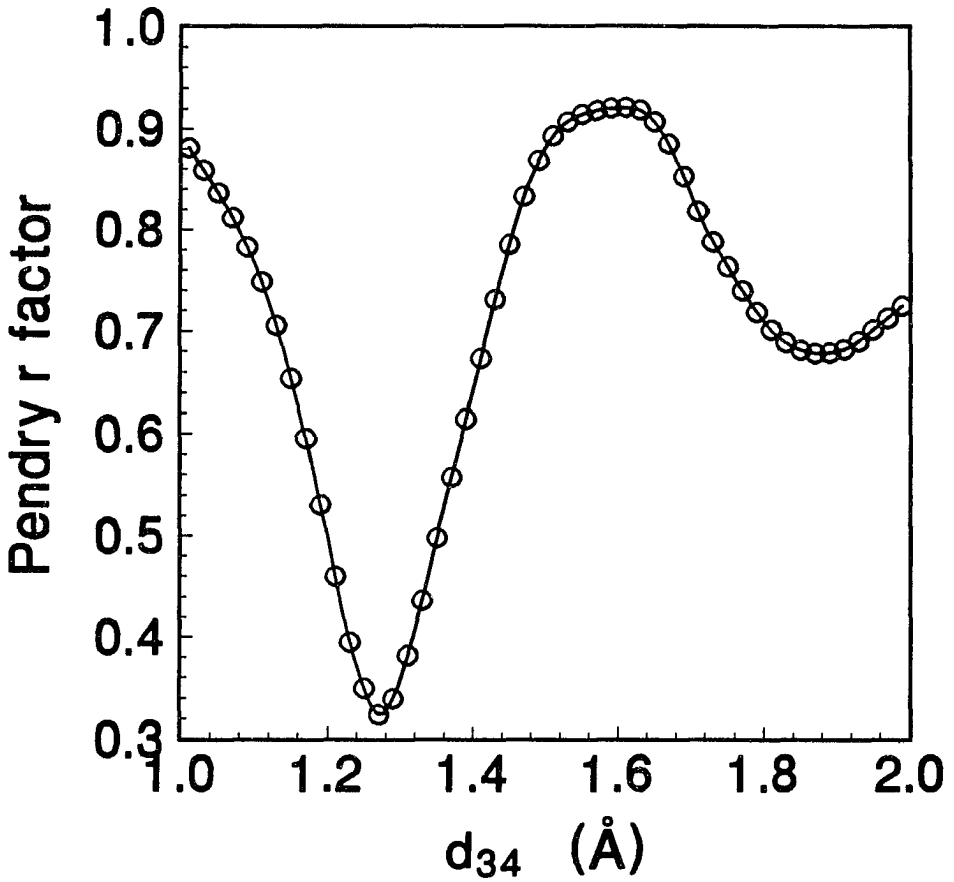


Figure 8. (Continued)

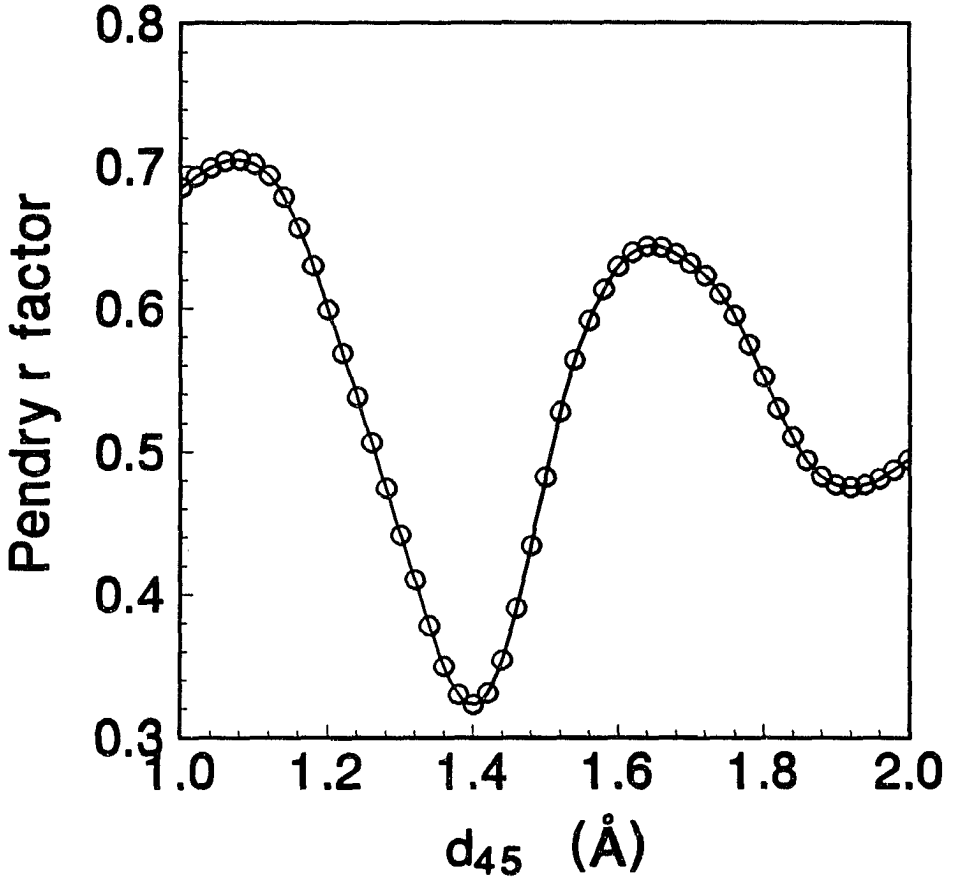


Figure 8. (Continued)

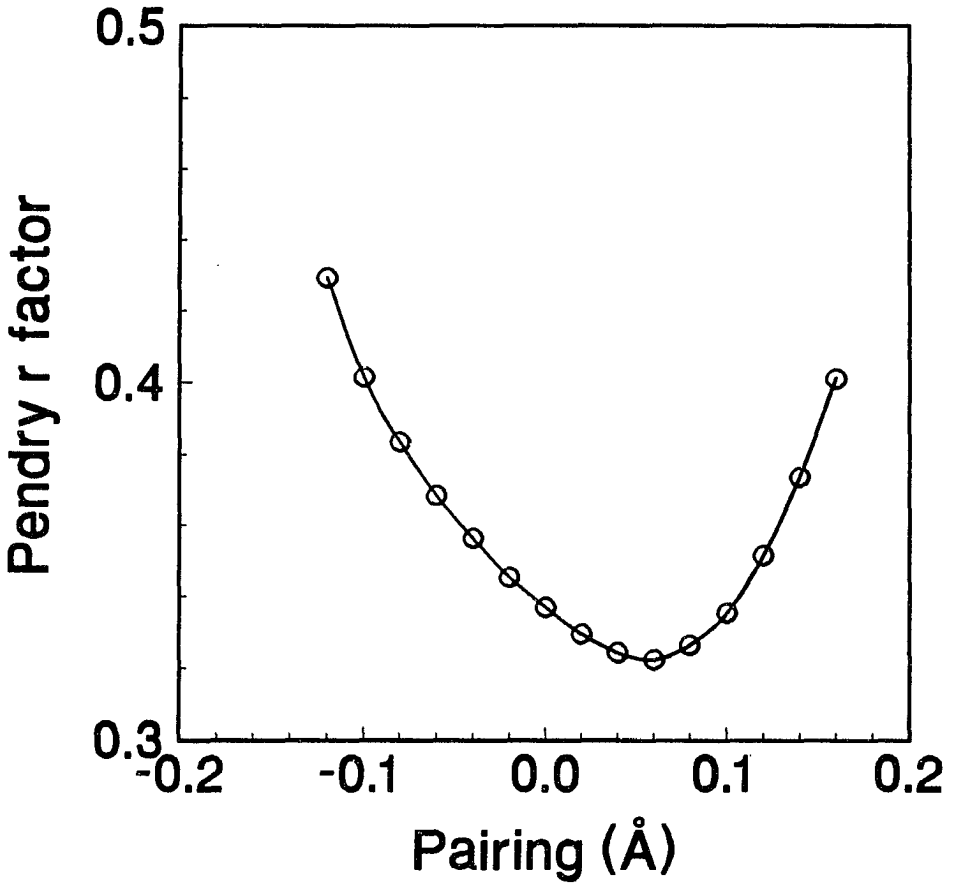


Figure 8. (Continued)

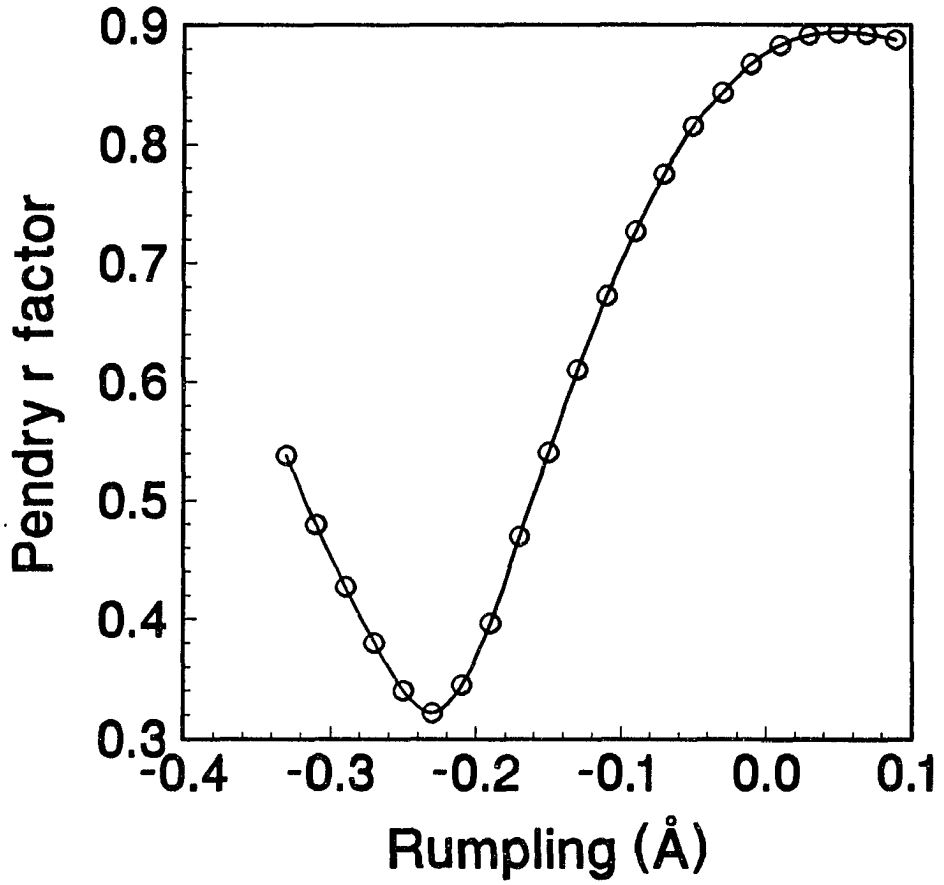


Figure 8. (Continued)

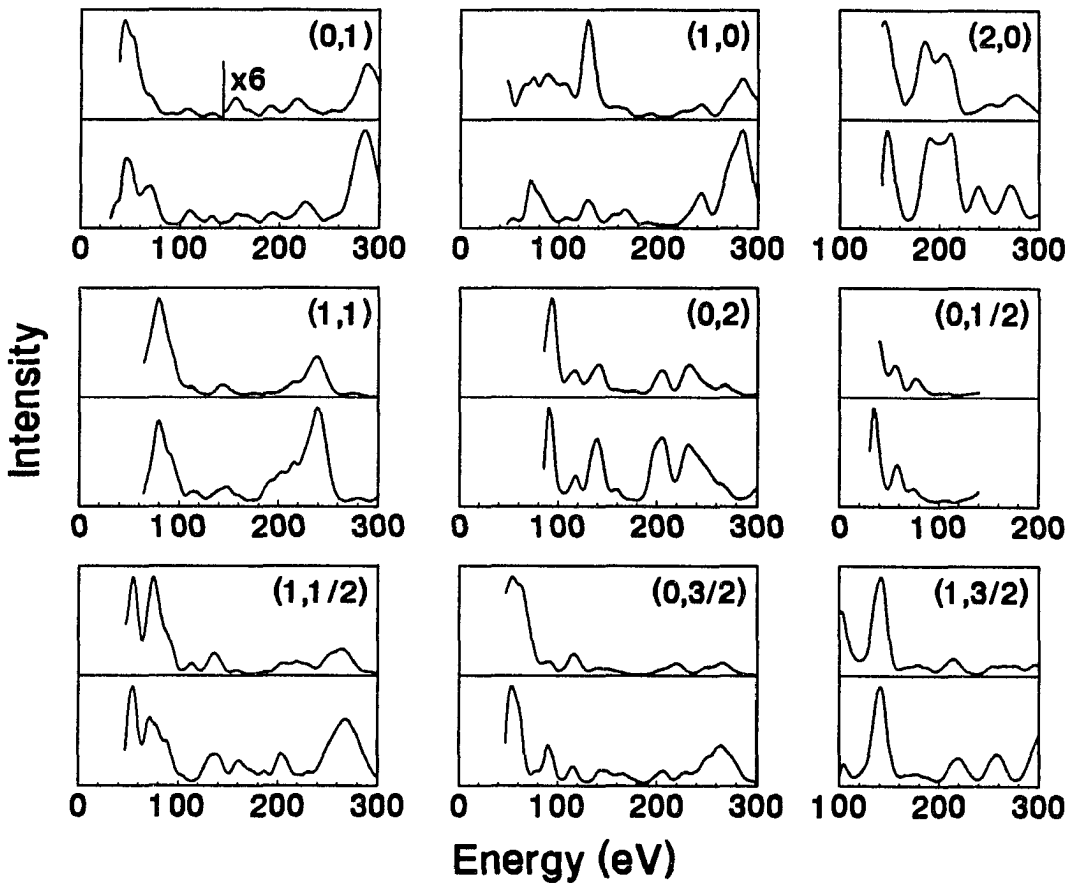


Figure 9. Experimental and best-fit theoretical I(E) curves for the (1x2) structure

# VI. DISCUSSION

A comparison to LEED results obtained for relevant surface structures of Pt and Pd is made in Table 4. While both (1x1) films are found to follow the trend of contracted $d_{12}$ and expanded $d_{23}$ characteristic of clean surfaces of bulk fcc(110)-(1x1) metals (36), the magnitudes of the relaxations are found to depend on Pt coverage. The much larger contraction in $d_{12}$ of the 1-ML film relative to that of either the 2-ML film or the clean substrate (see Table 4) suggests that an attractive electronic interaction between Pt and Pd is present at the interface, i.e., bonding between Pt and Pd is stronger than either to itself. However, the attractive interaction does not appear to be strong enough to override the driving force for oscillatory relaxation when a second layer of Pt is present since this structure exhibits an expanded interlayer spacing at the interface.

It is known that strong bonding between the overlayer and substrate favors complete wetting for the first monolayer of deposition (37). Therefore, it is reasonable to conclude that the (1x1) structure should be more stable than the missing-row-type structure at 1 ML since the (1x1) structure maximizes the number of Pt atoms in contact with the Pd substrate. Thus, it is not surprising that a minimum Pt coverage is required before reconstruction can set in. As mentioned previously, no evidence for superstructure formation is observed at Pt coverages $\leq$1 ML. The presence of an attractive electronic interaction is also consistent with a tendency to alloy (37), which is supported by our observation of extensive film dissolution upon annealing to a sufficiently high

Table 4. Comparison of Pt on Pd(110) results to Pt and Pd structures that have been determined by LEED

| Surface | $\Delta d_{12}$ (%) | $\Delta d_{23}$ (%) | $\sigma$ (Å) | $\delta$ (Å) | Reference |
|---|---|---|---|---|---|
| Pd(110)-(1x2) (Cs-induced) | -9 | -1 | 0.05 | -0.1 | 34 |
| Pt(110)-(1x2) | -18.4 | -24.2 | 0.07 | -0.32 | 2 |
| Pt(110)-(1x2) | -20.9 | -7.2 | 0.04 | -0.17 | 3 |
| Pt/Pd(110)-(1x2) | -9.5 | -8.0 | 0.06 | -0.23 | this work |
| Pd(110)-(1x1) | -5.7 | 0.5 | | | 4 |
| Pd(110)-(1x1) | -5.1 | 2.9 | | | 5 |
| Pt/Pd(110)-(1x1) (1 ML) | -11.0 | 6.6 | | | this work |
| Pt/Pd(110)-(1x1) (2 ML) | -6.6 | 4.4 | | | this work |

temperature.

The optimum geometry of the (1x2) structure is found to be qualitatively similar to that of bulk Pt(110)-(1x2). Quantitatively, the most striking difference is that $d_{12}$ of the Pt film is clearly found to be only half as contracted (see Table 4). Two factors could contribute to this difference. First, a lattice compression of 0.8% in the Pt overlayer–induced by the smaller surface unit cell of the Pd substrate– may create sufficient strain energy that a less contracted $d_{12}$ results. Second, the relaxation of the (1x2) structure may be governed to some extent by the electronic influence of the Pd substrate.

For clean surfaces of bulk fcc(110) metals, the reduction in total energy by reconstructing to the (1x2) missing-row-type structure is probably rather small since this phenomena occurs only for Pt, Au (38), and Ir (39). In fact, a first-principles calculation has shown that the surface energy of the (1x2) phase of Au is only ca. 5% lower than that of the (1x1) phase (40). Further evidence for a small difference in the stability of the two phases is that clean surfaces of bulk fcc(110)-(1x1) metals can be pushed into the (1x2) missing-row-type structure by a slight disturbance, e.g., by a small fraction of a monolayer of alkali metal (34). Thus, subtle modifications in the electronic structure of fcc(110) metals can cause significant changes in geometric structure. Based on these arguments, a less contracted $d_{12}$ due in part to a different electronic environment is understandable.

## VII. ACKNOWLEDGEMENTS

The experimental component of this work is supported primarily by the National Science Foundation through Grant No. CHE-9014214, and by the Ford Motor Company. R.J. Baird and G.W. Graham of Ford Motor Company are thanked for the use of their Pd(110) crystal. M.A. Van Hove is thanked for supplying the LEED package and phase shifts for the (1x1) analysis. E. Arola is thanked for providing the Pt potential for the (1x2) analysis. O.L.W. acknowledges support from the Amoco Foundation, P.J.S. acknowledges support from Phillips Petroleum, and P.A.T. acknowledges support from NSF Grant No. CHE-9024358, and from the Camille and Henry Dreyfus Foundation. Some equipment and all facilities are provided by the Ames Laboratory, which is operated for the U.S. Department of Energy by Iowa State University under Contract No. W-7405-ENG-82.

# VIII. REFERENCES


1. P. Fenter and T. Gustafsson, Phys. Rev. B 38 (1988) 10197.
2. E.C. Sowa, M.A. Van Hove and D.L. Adams, Surf. Sci. 199 (1988) 174.
3. P. Fery, W. Moritz and D. Wolf, Phys. Rev. B 38 (1988) 7275.
4. R.D. Diehl, M. Lindroos, A. Kearsley, C.J. Barnes and D.A. King, J. Phys. C 18 (1985) 4069.
5. M. Skottke, R.J. Behm, G. Ertl, V. Penka and W. Moritz, J. Chem. Phys. 87 (1987) 6191.
6. M. Wolf, A. Goschnick, J. Loboda-Cacković, M. Grunze, W.N. Unertl and J.H. Block, Surf. Sci. 182 (1987) 489.
7. C. Kittel, Introduction to Solid State Physics (Wiley, New York, 1986).
8. J.H. van der Merwe, Philos. Mag. A 45 (1982) 127.
9. W.-Y. Leung, P.J. Schmitz, H.-C. Kang and P.A. Thiel, Surf. Sci. 257 (1991) 79.
10. P.J. Schmitz, W.-Y. Leung, H.-C. Kang and P.A. Thiel, Phys. Rev. B 44 (1991) 13734.
11. R.P. Elliot and F.A. Shunk, Bull. Alloy Phase Diagrams 2 (1982) 482.
12. T. Gritsch, D. Coulman, R.J. Behm and G. Ertl, Phys. Rev. Lett. 63 (1989) 1086, and references therein.
13. J. Goschnick, M. Wolf, M. Grunze, W.N. Unertl, J.H. Block and J. Loboda-Cacković, Surf. Sci. 178 (1986) 831.
14. G.E. Rhead, M.-G. Barthès and C. Argile, Thin Solid Films 82 (1981) 201.
15. D.K. Flynn, W.-D. Wang, S.-L. Chang, M.C. Tringides and P.A. Thiel,

Langmuir 4 (1988) 1096.

16. J.R. Noonan and H.L. Davis, in: Determination of Surface Structure by LEED, Eds. P.M. Marcus and F. Jona (Plenum, New York, 1984) p. 449.
17. M.A. Van Hove and S.Y. Tong, Surface Crystallography by LEED (Springer, Berlin, 1979).
18. R. Baudoing, Y. Gauthier, M. Lundberg and J. Rundgren, J. Phys. C 19 (1986) 2825.
19. S. Crampin and P.J. Rous, Surf. Sci. 244 (1991) L137.
20. V. Moruzzi, J. Janak and A. Williams, Calculated Electronic Properties of Metals (Pergamon, New York, 1978).
21. Attributed to S.W. Wang.
22. L.F. Mattheiss, Phys. Rev. 133 (1964) A1399.
23. H.B. Nielsen and D.L. Adams, J. Phys. C 15 (1982) 615.
24. J.B. Pendry, J. Phys. C 13 (1980) 937.
25. J. Quinn, Y.S. Li, H. Li, D. Tian, F. Jona and P.M. Marcus, Phys. Rev. B 43 (1991) 3959.
26. M.L. Xu and S.Y. Tong, Phys. Rev. B 31 (1985) 6332.
27. K.-P. Bohnen, C.T. Chan and K.M. Ho, Surf. Sci. 268 (1992) L284.
28. D.F. Ogletree, M.A. Van Hove and G.A. Somorjai, Surf. Sci. 173 (1986) 351.
29. M. Henzler, Surf. Sci. 22 (1970) 12.
30. E. Zanazzi, F. Jona, D.W. Jepsen and P.M. Marcus, J. Phys. C 10 (1977) 375.
31. D.K. Flynn, J.W. Evans and P.A. Thiel, J. Vac. Sci. Technol. A 7 (1989) 2162.
32. J.W. Evans, D.E. Sanders, P.A. Thiel and A.E. DePristo, Phys. Rev. B

41 (1990) 5410.

33. H.P. Bonzel and S. Ferrer, Surf. Sci. 118 (1982) L263.

34. C.J. Barnes, M. Lindroos and D.A. King, Surf. Sci. 201 (1988) 108.

35. D.L. Adams, H.B. Nielsen, M.A. Van Hove and A. Ignatiev, Surf. Sci. 104 (1981) 47.

36. For examples, see J.M. MacLaren, J.B. Pendry, P.J. Rous, D.K. Saldin, G.A. Somorjai, M.A. Van Hove and D.D. Vvedensky, Surface Crystallographic Information Service (Reidel, Boston, 1987).

37. J.H. van der Merwe, in: Chemistry and Physics of Solid Surfaces V, Eds. R. Vanselow and R. Howe (Springer, Berlin, 1984) p. 365.

38. W. Moritz and D. Wolf, Surf. Sci. 163 (1985) L655.

39. C.-M. Chan and M.A. Van Hove, Surf. Sci. 171 (1986) 226.

40. K.M. Ho and K.-P. Bohnen, Phys. Rev. Lett. 59 (1987) 1833.

# PAPER III:

# STRUCTURAL DETERMINATION OF A NiO(111) FILM ON Ni(100) BY DYNAMICAL LOW-ENERGY ELECTRON-DIFFRACTION ANALYSIS

# Structural Determination of a NiO(111) Film on Ni(100) by Dynamical Low-Energy Electron-Diffraction Analysis

O.L. Warren and P.A. Thiel

Department of Chemistry and Ames Laboratory

Iowa State University

Ames, Iowa 50011

## ABSTRACT

The geometric structure of a thin NiO(111) film on Ni(100) has been determined by dynamical low-energy electron-diffraction analysis. The oxide film is sufficiently thick to carry out the analysis in the bulk crystal limit. Four orientational domains of NiO(111) are present. We consider four possible terminations of the oxide film (oxygen or nickel, fcc or hcp sites). Our results indicate that the oxide film terminates with a topmost layer of oxygen in fcc sites, and exhibits a 14.8% contraction in the first interlayer spacing. The "bulk" lattice parameters of the oxide film are found to be uniformly compressed by 2.6% relative to bulk NiO(111).

# I. INTRODUCTION

Presumably, surface energy considerations will dictate whether a polar metal oxide film terminates with a topmost layer of oxygen or metal. As a consequence, a polar metal oxide film offers insight into the relative stabilities of the anionic and cationic surfaces of its corresponding bulk crystal. In the case of metal oxides crystallizing in the rocksalt structure, the (111) surfaces are polar (1). [A rocksalt(111) crystal can be thought of in terms of an fcc(111) crystal with layers alternating between all anions and all cations; therefore, each charge neutral slab possesses a perpendicular dipole moment.] Electrostatic arguments show that polar surfaces of ionic crystals should have prohibitively large surface energies, and can only be stabilized by reconstruction or adsorption of additional charge (1). Experimental studies of rocksalt(111) surfaces of bulk metal oxides confirm the general validity of the electrostatic arguments, e.g., MgO(111) has been reported to reconstruct (2) and facet to stable nonpolar (100) surfaces (3), and NiO(111) has been reported to be stabilized by impurity segregation (4).

With the inherent instability of rocksalt(111) surfaces in mind, it is quite interesting that thin films of metal oxides crystallizing in the rocksalt structure can often be grown in the (111) orientation without reconstruction (5-12). A classic example of this is thin films of NiO(111) grown by oxidation of Ni(100) (8-12). These films grow preferentially at temperatures below ca. 300 K (10), to a saturation thickness of ca. 3-4 layers of NiO (9,11,12), and in accordance with the theories of surface stabilities of ionic crystals (1,13,14), they are unstable with respect to

NiO(100) at temperatures above ca. 500 K (10,12).

Although considerable effort has been expended in studying surface oxidation of Ni(100) (8-12,15-20), the fundamental question of whether a NiO(111) film on Ni(100) is terminated with a topmost layer of oxygen or nickel has not yet been answered. Of course, such knowledge is a prerequisite for developing a detailed understanding of the properties of such a film; therefore, we have undertaken a dynamical low-energy electron-diffraction (LEED) analysis of its structure.

## II. EXPERIMENTAL PROCEDURES

Experiments are performed in a stainless-steel ultrahigh-vacuum chamber (base pressure $\leq 1 \times 10^{-10}$ torr) equipped with a single-pass cylindrical mirror analyzer for Auger electron spectroscopy (AES); $\mu$-metal-shielded, display-type, four-grid LEED optics; quadrupole mass spectrometer; sputter gun; and provisions for gas exposure. The Ni(100) crystal is cleaned by cycles of $Ar^+$ bombardment at 300 K and annealing at 1000 K. Residual carbon is removed by cycles of small doses of oxygen at 300 K and annealing at 1000 K. After cleaning in the above manner, no impurities are detected by AES and the surface exhibits a high-quality (1x1) LEED pattern.

Thin films of NiO(111) are prepared by oxidation of Ni(100) at 225 K, followed by annealing at 425 K. An exposure of 160 Langmuir ($P = 8 \times 10^{-8}$ torr) is sufficient to optimize the NiO(111) LEED pattern. AES measurements from the annealed oxide film do not reveal impurity concentrations greater than the noise level. Figure 1 shows a photograph of the NiO(111) LEED pattern at 90 eV. This pattern can only be explained by the presence of orientational domains, which is discussed later in detail. Since the NiO(111) LEED pattern exhibits relatively sharp spots, we speculate that the domains have significant lateral dimensions. However, increased background intensity is observed and the maximum intensity level of the spots is roughly a factor of eight lower than that of the clean substrate, so it is highly likely that the ordered domains coexist with significant regions of considerable disorder. [Although it should be noted that part of the reduction in intensity can be attributed

Figure 1. NiO(111) LEED pattern at 90 eV

to the presence of incorporated oxygen, which scatters more weakly than nickel. Based on a comparison between calculated intensities for the clean surface of Ni(100) and calculated intensities for the oxide film, a reduction by a factor of 2.5 in the maximum intensity level is to be expected when both surfaces are perfectly ordered.]

Experimental LEED intensity-energy [I(E)] curves are acquired at normal incidence (50-170 eV, 1-eV grid) with a computer-interfaced video processor and a silicon-intensified-target camera. The crystal is maintained at 105 K. Sixteen video frames are averaged at each energy to improve the signal-to-noise ratio. Camera saturation effects are tested by collecting curves over a wide range of camera aperture settings. Equivalent beam averaging—a procedure known to minimize residual experimental errors (21)— is carried out over the experimentally accessible beams. Background subtraction is performed locally during data collection, and normalization to constant beam current is performed separately after measuring the current as a function of beam energy with the crystal biased sufficiently positive to suppress secondary emission. Curves collected in three separate experiments are in excellent agreement, and are averaged to further enhance statistical reliability.

# III. COMPUTATIONAL PROCEDURES

Theoretical I(E) curves are calculated from 40-180 eV for normal incidence with the LEED package of Van Hove and Tong (22). After calculating reflection and transmission matrices within the self-consistent formalism, interlayer scattering is accomplished by layer doubling. An equivalent of up to 55 beams are included in the plane-wave expansion of the wave field. Domain averaging is carried out to reproduce the symmetry observed in the experimental LEED pattern.

Eight phase shifts ($\ell_{max}$ =7) are used throughout. Although NiO is ionic, we have chosen to use neutral phase shifts on the basis that calculated phase shifts have been found to be rather insensitive to the amount of charge transfer (5). Nickel phase shifts are calculated from the Wakoh potential (23), and oxygen phase shifts are calculated from overlapping atomic potentials (24). Corrections to the phase shifts for thermal effects are not taken into account, but this should be of no consequence in view of the relatively high Debye temperature ($\theta_D$) of NiO (ca. 500 K) (25,26). The real part of the optical potential ($V_{or}$) is assumed to be constant over the entire energy range, and is initially set to -10 eV. During reliability-factor (r-factor) analysis, this parameter is treated as a variable and is rigidly shifted in 1-eV steps to obtain the best level of agreement. The final value of $V_{or}$ corresponding to the optimum geometry is found to be unchanged from the initial value. The imaginary part of the optical potential ($V_{oi}$) is fixed at -5 eV. Further steps to improve the level of agreement through the values of the nonstructural parameters are not taken since such steps generally have

little influence on the final structural result (27).

Experimental and theoretical I(E) curves are compared quantitatively with the Pendry r factor ($r_p$) (28). Since this r factor is highly sensitive to spectral noise (28), both sets of curves are smoothed with two passes of a three-point smoothing algorithm (29) prior to r-factor analysis.

# IV. RESULTS AND DISCUSSION

Figure 2 shows a schematic of the LEED pattern observed before and after oxidation at 225 K. Squares correspond to the LEED pattern of the clean substrate, and open and filled circles correspond to the superposition of two hexagonal arrays of spots associated with the oxide film. The latter LEED pattern was first observed by Holloway and Hudson (8), and was later assigned by Mitchell, Sewell, and Cohen (9) to two orientational domains of NiO(111) rotated 30° apart.

Figure 3 shows that all spots at a radius defined by the (1,0) beam of NiO(111) yield equivalent I(E) curves at normal incidence, which indicates that the intensities of each of the two hexagonal arrays of spots exhibit sixfold symmetry at normal incidence rather than the expected threefold symmetry of fcc(111) stacking. [Our intensity calculations indicate that the twelve first-order spots would yield two distinctly different sets of curves if only threefold symmetry were present.] This result is consistent with the presence of four orientational domains of NiO(111) with azimuthal rotations of 0, 30, 60, and 90° rather than two orientational domains of NiO(111) with azimuthal rotations of 0 and 30°. Moreover, since four of the twelve first-order spots coincide with the original (1,0)-type spots of the clean substrate, the equivalency of all first-order curves further indicates that the oxide film is sufficiently thick to carry out the analysis in the bulk crystal limit, and that contributions to the curves from possibly bare substrate areas are negligible. In support of these conclusions, spots corresponding to the (1,1) beam set of Ni(100), which do not coincide with spots associated with the oxide film, are not observed

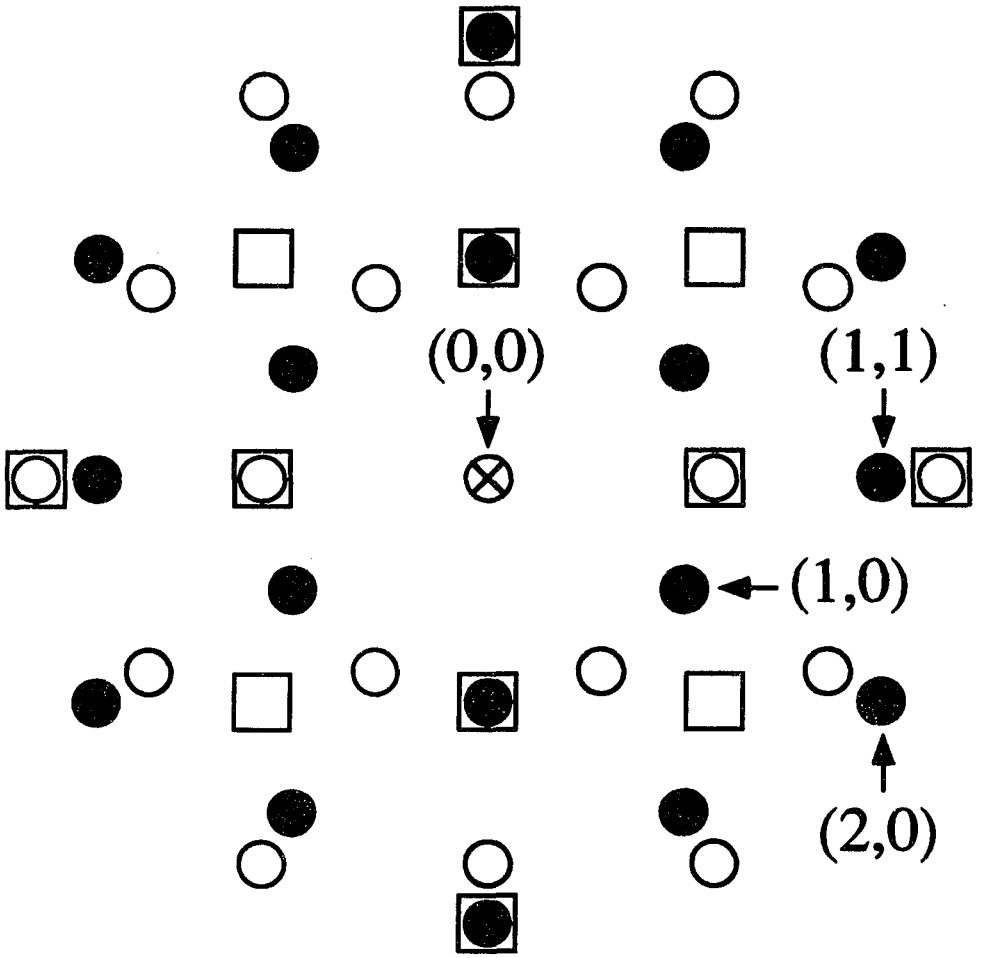


Figure 2. Schematic of the LEED pattern observed before and after oxidation of Ni(100) at 225 K

Squares correspond to the LEED pattern of clean Ni(100), and open and filled circles correspond to the superposition of two hexagonal arrays of spots associated with NiO(111). Beam indices are shown for one orientational domain of NiO(111).

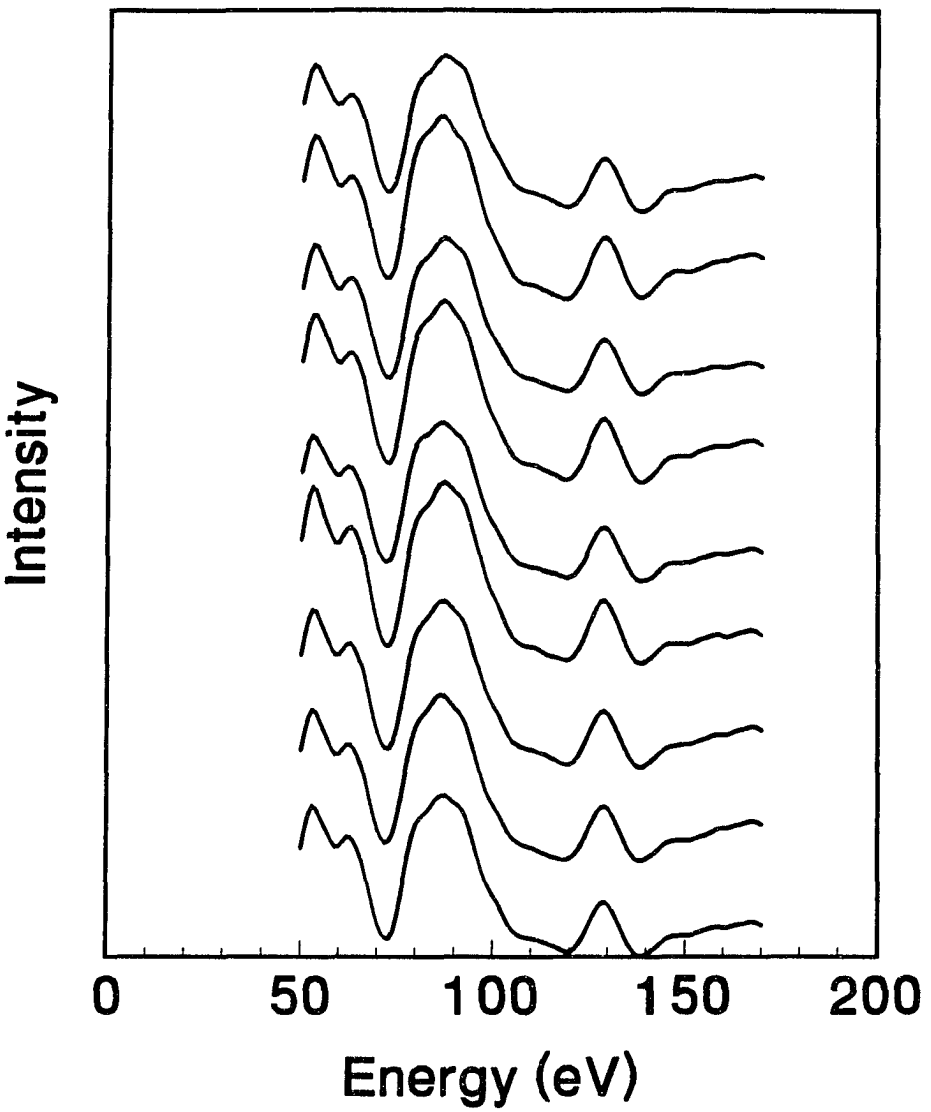


Figure 3. Experimental I(E) curves for the accessible first-order spots of NiO(111)

Second, fifth, and eighth curves from the top are for spots coinciding with the original (1,0)-type spots of Ni(100). Displayed curves are from a single experiment.

after oxidation.

As mentioned previously, it is not known whether the NiO(111) film terminates with a topmost layer of oxygen or nickel. Furthermore, it is also feasible for the topmost layer to undergo a phase transformation from the expected fcc sites to hcp sites. Therefore, we consider the following four terminations: oxygen in fcc sites (FCC-O), nickel in fcc sites (FCC-Ni), oxygen in hcp sites (HCP-O), and nickel in hcp sites (HCP-Ni). From the intralayer lattice parameter of Ni(100) (2.491 Å), one can deduce from the LEED pattern an intralayer lattice parameter of 2.876 Å for the oxide film, which corresponds to a lateral compression of 2.6% relative to bulk NiO(111). We have chosen to set the "bulk" interlayer spacing of the oxide film ($d_{bulk}$) to 1.174 Å, which corresponds to a uniform compression in both lateral and vertical directions. The experimental data base to compare to theory consists of (1,0) and (1,1) I(E) curves yielding a total-energy range of $\Delta E$ =159 eV. [Spots at a radius defined by the (2,0) beam of NiO(111) are also observed, but only over an insufficient energy range]. In view of the limited data base, only the first interlayer spacing ($d_{12}$) is varied (0.924-1.224 Å) in trying to distinguish between the four possible terminations.

Figures 4 and 5 compare experimental I(E) curves to optimum theoretical I(E) curves obtained for each of the four terminations. Visual inspection readily confirms that only the FCC-O model reproduces both (1,0) and (1,1) curves simultaneously. Minimum r factors obtained for each of the four models are as follows: $r_p$ =0.28 for FCC-O, 0.66 for FCC-Ni, 0.43 for HCP-O, and 0.57 for HCP-Ni. Figure 6 shows a plot of $r_p$ as a function of $d_{12}$ for the FCC-O model. The r-factor minimum occurs at 1.00 Å, which

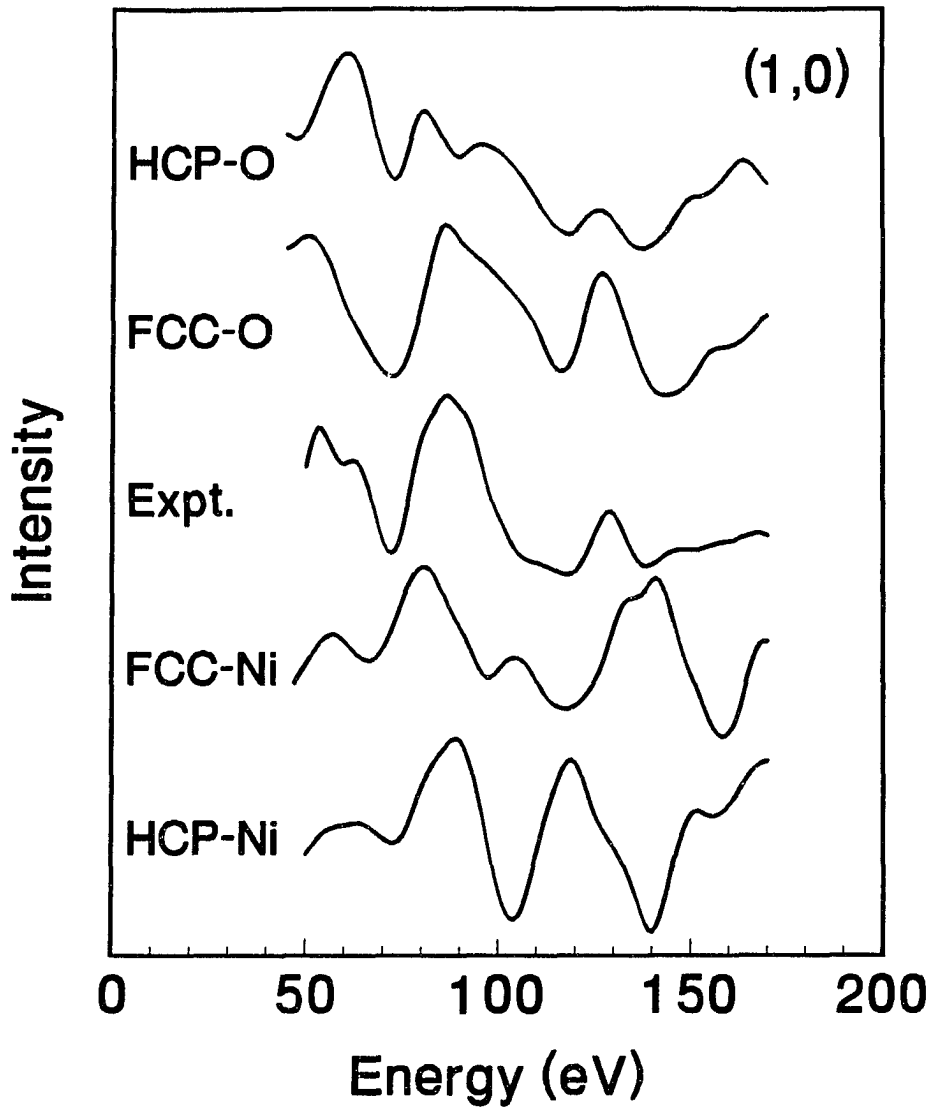


Figure 4. Experiment-theory comparison for the (1,0) I(E) curve

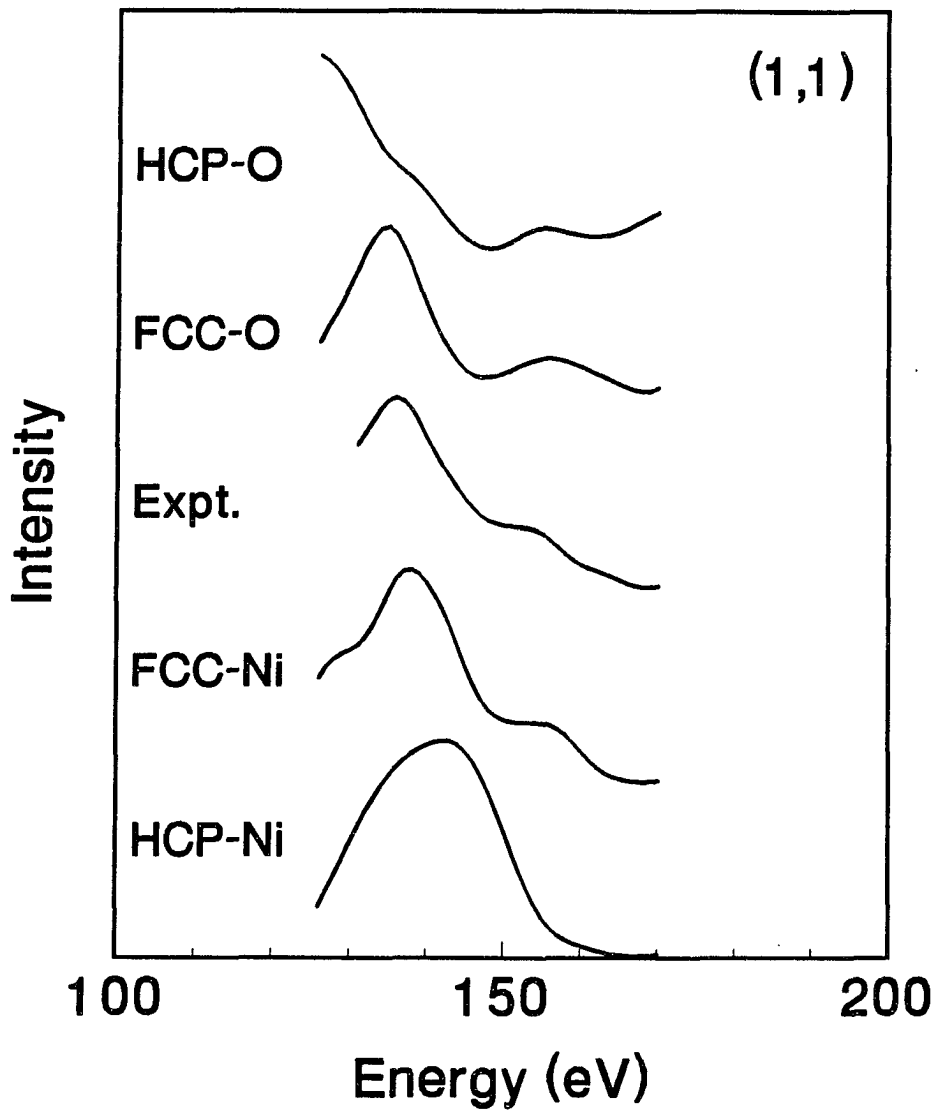


Figure 5. Experiment-theory comparison for the (1,1) I(E) curve

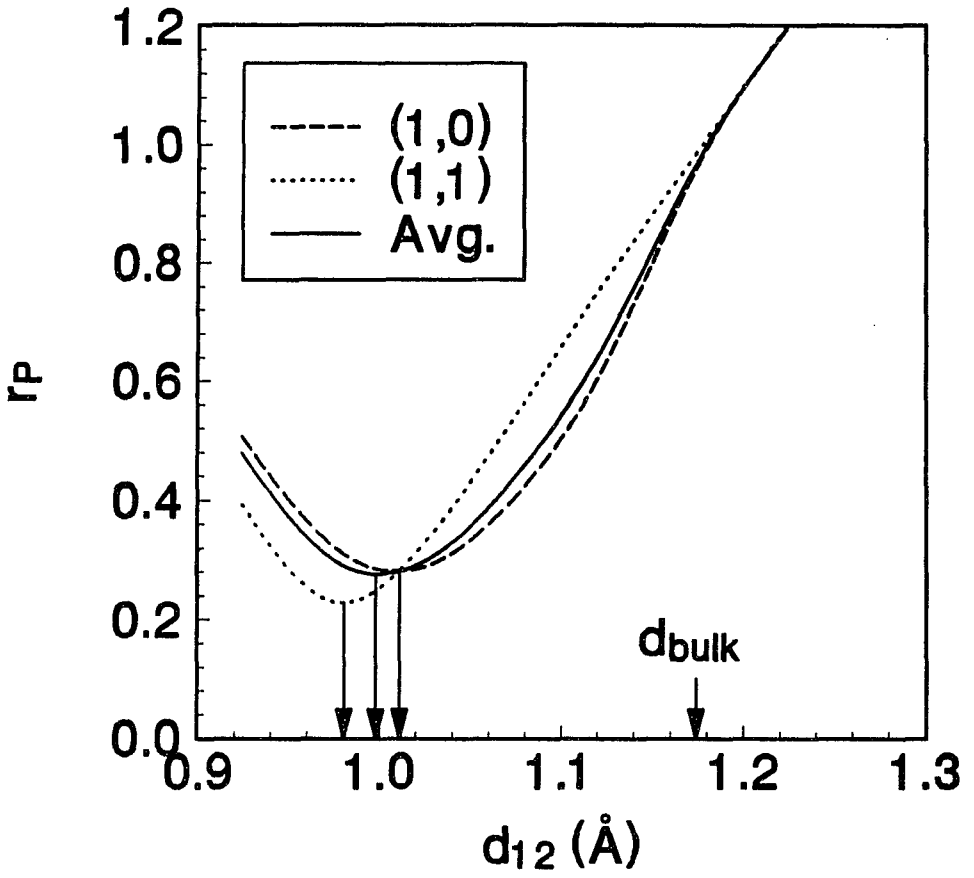


Figure 6. Pendry r factor as a function of the first interlayer spacing for the FCC-O model

The average r-factor plot represents the energy-range weighted average of the single-beam r-factor plots.

corresponds to a 14.8% contraction in $d_{12}$ relative to $d_{bulk}$ of the oxide film. Based on the spread of the minima of the single-beam r factors, which are also shown in Fig. 6, we estimate an uncertainty in $d_{12}$ of ±0.03 Å or ±2.5% of $d_{bulk}$. An estimate of this quantity based on Pendry's (28) definition of the variance–$\Delta r = r_{min}(8V_{oi}/\Delta E)^{1/2}$– results in a significantly larger value (±0.06 Å or ±5% of $d_{bulk}$) due primarily to the limited data base. It is important to note that the values quoted above for both $d_{12}$ and its uncertainty do not take into account possible correlations between $d_{12}$ and deeper interlayer spacings. Nevertheless, it is still safe to say that $d_{12}$ is significantly contracted.

Having established that the termination is FCC-O, we now test the validity of assuming a uniformly compressed lattice for the "bulk" layers of the oxide film. First, we consider the possibility that a lateral compression might result in a vertical expansion to conserve the bulk NiO value for the bond length between nickel and its nearest oxygen neighbor in the adjacent layer. The minimum r factor obtained for this model after varying $d_{12}$ ($r_p$ =0.49), however, clearly does not favor a distortion away from the cubic symmetry of the rocksalt lattice in the "bulk" layers. Next, we consider the possibility that the "bulk" lattice parameters of the oxide film may actually be equal to those of bulk NiO(111). A difference of only 2.6% in the intralayer lattice parameter may be difficult to detect by inspection of the LEED patterns. Although the minimum r factor obtained for this model after varying $d_{12}$ ($r_p$ =0.31) is only slightly higher than that achieved for a uniform compression in the "bulk" layers, the final value of $V_{or}$ (0 eV) is not consistent with the values of -10 to -15 eV reported in previous dynamical LEED studies of simple metal oxide surfaces

(5,30-33). On the other hand, the final value of $V_{or}$ for a uniform compression in the "bulk" layers (-10 eV) is consistent with the range of values mentioned above; therefore, we believe that the oxide film adopts a uniformly-compressed lattice in the "bulk" layers. Figure 7 gives a possible explanation for the observed lateral compression. An intralayer lattice parameter of 2.876 Å implies that the perpendicular distance between the atomic rows of the oxide film exactly matches the distance between the atomic rows of the substrate. Thus, by compressing laterally, the oxide film can match the row spacings of the substrate in one dimension to reduce interfacial strain.

Finally, we assess the generality of our results. A dynamical LEED analysis of an unreconstructed thin film of CoO(111) on Co(0001) also favors termination with a topmost layer of oxygen in fcc sites and a 15±5% contraction in $d_{12}$ relative to $d_{bulk}$ of the oxide film (5), and a recent theoretical calculation based on the Harris-Foulkes total energy functional in the local density approximation indicates that the oxygen-terminated surface of bulk-truncated MgO(111) has a lower surface energy than the metal-terminated surface (13). These results, in conjunction with our own, suggest that termination with a topmost layer of oxygen in fcc sites and a large contraction in $d_{12}$ relative to $d_{bulk}$ of the oxide film may be of general significance for unreconstructed rocksalt(111) surfaces of thin metal oxide films. [In the case of the CoO(111) film, the large contraction in $d_{12}$ has been explained qualitatively by the net electrostatic force acting on a surface ion due to the other ions in the crystal (34).] In closing, we note that the "bulk" component of the CoO(111) film adopts a uniformly-expanded lattice relative to bulk

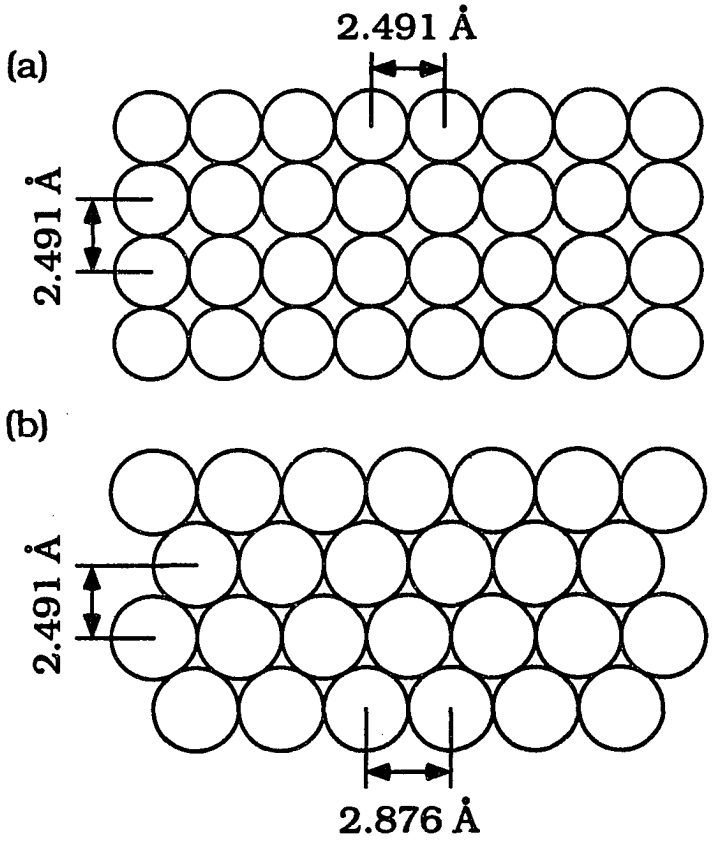


Figure 7. One-dimensional row matching at the Ni(100) and NiO(111) interface

a) Hard sphere representation of the Ni(100) surface.

b) Hard sphere representation of the interfacial layer of two of the four orientational domains of NiO(111). [The relative registries of the subsequent layers determine which of the two orientational domains is represented.]

Rotating b) by 90° results in the hard sphere representation of the interfacial layer of the two remaining orientational domains of NiO(111).

CoO(111) (5). Comparison of this result to the uniform compression found here for the "bulk" component of the NiO(111) film suggests that except for surface relaxation, a distortion away from the cubic symmetry of the rocksalt lattice may not be energetically favorable.

# V. CONCLUSIONS

Dynamical LEED results indicate that a thin NiO(111) film grown by oxidation of Ni(100) at 225 K is terminated with a topmost layer of oxygen in fcc sites, and exhibits a 14.8% contraction in the first interlayer spacing relative to the "bulk" interlayer spacing of the oxide film. The "bulk" lattice parameters of the oxide film are found to be uniformly compressed by 2.6% relative to bulk NiO(111). The observed lateral compression is consistent with a reduction in interfacial strain via one-dimensional row matching between the overlayer and substrate. The oxide film is sufficiently thick that the substrate does not participate in the diffraction process, and bare Ni(100) areas are not detected. Four orientational domains of NiO(111), with lateral dimensions sufficient to produce relatively sharp LEED spots, are present. However, it is highly likely that the ordered domains coexist with significant regions of considerable disorder. Comparison to a previous dynamical LEED study of a thin CoO(111) film on Co(0001) (5), and to a theoretical calculation of the relative stabilities of the anionic and cationic surfaces of MgO(111) (13), suggests that termination with a topmost layer of oxygen in fcc sites and a large contraction in the first interlayer spacing relative to the "bulk" interlayer spacing of the oxide film may be of general significance for unreconstructed rocksalt(111) surfaces of metal oxide films.

## VI. ACKNOWLEDGEMENTS

M.A. Van Hove is thanked for supplying the LEED package. This work is supported by the National Science Foundation through Grant No. GER-9024358. O.L.W. acknowledges additional support from the U.S. Department of Education. Some equipment and all facilities are provided by the Ames Laboratory, which is operated for the U.S. Department of Energy by Iowa State University under Contract No. W-7405-ENG-82.

# VII. REFERENCES


1. P.W. Tasker, J. Phys. C 12 (1979) 4977.
2. M. Gajdardziska-Josifovska, P.A. Crozier and J.M. Cowley, Surf. Sci. 248 (1991) L259.
3. V.E. Henrich, Surf. Sci. 57 (1976) 385.
4. N. Floquet and L.-C. Dufour, Surf. Sci. 126 (1983) 543.
5. A. Ignatiev, B.W. Lee and M.A. Van Hove, in: Proceedings of the 7th International Vacuum Congress and 3rd International Conference on Solid Surfaces (Vienna, 1977) p. 1733.
6. G.H. Vurens, V. Maurice, M. Salmeron and G.A. Somorjai, Surf. Sci. 268 (1992) 170.
7. H. Namba, J. Darville and J.M. Gilles, Surf. Sci. 108 (1981) 446.
8. P.H. Holloway and J.B. Hudson, Surf. Sci. 43 (1974) 123.
9. D.F. Mitchell, P.B. Sewell and M. Cohen, Surf. Sci. 61 (1976) 355.
10. W.-D. Wang, N.J. Wu and P.A. Thiel, J. Chem. Phys. 92 (1990) 2025.
11. S.J. Bushby, T.D. Pope, B.W. Callen, K. Griffiths and P.R. Norton, Surf. Sci. 256 (1991) 301.
12. J.G. Chen, D.A. Fischer, J.H. Hardenbergh and R.B. Hall, Surf. Sci. 279 (1992) 13.
13. A. Gibson, R. Haydock and J.P. LaFemina, J. Vac. Sci. Technol. A 10 (1992) 2362.
14. P.A. Cox, F.W.H. Dean and A.A. Williams, Vacuum 33 (1983) 839, and references therein.
15. C.R. Brundle and J.Q. Broughton, in: The Chemical Physics of Solid Surfaces and Heterogeneous Catalysis, Vol. 3A, Eds. D.A. King and D.P.

Woodruff (Elsevier, Amsterdam, 1990) p. 381, and references therein.

16. J.G. Chen, M.D. Weisel and R.B. Hall, Surf. Sci. 250 (1991) 159.
17. M. Bäumer, D. Cappus, H. Kuhlenbeck, H.-J. Freund, G. Wilhelmi, A. Brodde and H. Neddermeyer, Surf. Sci. 253 (1991) 116.
18. T.D. Pope, S.J. Bushby, K. Griffiths and P.R. Norton, Surf. Sci. 258 (1991) 101.
19. R.S. Saiki, A.P. Kaduwela, M. Sagurton, J. Osterwalder, D.J. Friedman, C.S. Fadley and C.R. Brundle, Surf. Sci. 282 (1993) 33.
20. W.-D. Wang, N.J. Wu, P.A. Thiel and M.C. Tringides, Surf. Sci. 282 (1993) 229.
21. J.R. Noonan and H.L. Davis, in: Determination of Surface Structure by LEED, Eds. P.M. Marcus and F. Jona (Plenum, New York, 1984) p. 449.
22. M.A. Van Hove and S.Y. Tong, Surface Crystallography by LEED (Springer, Berlin, 1979).
23. S. Wakoh, J. Phys. Soc. Jap. 20 (1965) 1984.
24. J.E. Demuth, D.W. Jepsen and P.M. Marcus, Phys. Rev. Lett. 31 (1973) 540.
25. W.L. Roth, Phys. Rev. 110 (1958) 1333.
26. W.-D. Wang, PhD Thesis, Iowa State University (1990).
27. H.B. Nielsen and D.L. Adams, J. Phys. C 15 (1982) 615.
28. J.B. Pendry, J. Phys. C 13 (1980) 937.
29. M.A. Van Hove, W.H. Weinberg and C.-M. Chan, Low-Energy Electron Diffraction (Springer, Berlin, 1986).
30. M.R. Welton-Cook and W. Berndt, J. Phys. C 15 (1982) 5691.
31. M. Prutton, J.A. Ramsey, J.A. Walker and M.R. Welton-Cook, J. Phys. C 12 (1979) 5271.

32. R.C. Felton, M. Prutton, S.P. Tear and M.R. Welton-Cook, Surf. Sci. 88 (1979) 474.

33. M.R. Welton-Cook and M. Prutton, J. Phys. C 13 (1980) 3993.

34. M.A. Van Hove and P.M. Echenique, Surf. Sci. 82 (1979) L298.

# GENERAL CONCLUSIONS

The main conclusions that can be drawn from the work presented in this dissertation are given below:

a) Within an uncertainty of 0.13 Å, the topmost layer of the clean surface of Pd(110) is in registry with the bulk layers. The first interlayer spacing is contracted by 4.4% relative to the bulk interlayer spacing, and the second interlayer spacing is expanded by 1.5%. These results demonstrate that if an order-disorder transition does occur on Pd(110) near 250 K, then it is of a much more subtle nature than has been proposed by other authors on the basis of their He-atom diffraction results.

b) Pt films deposited onto Pd(110) at 105 K retain the (1x1) periodicity of the underlying substrate when left unannealed. Auger measurements indicate that film growth at this temperature occurs in a reasonably layer-by-layer manner for at least the first two monolayers. However, from the quality of the LEED patterns, it is apparent that the films are not as well ordered as annealed surfaces. From a structural viewpoint, both one and two-monolayer films exhibit multilayer relaxation characteristic of clean (1x1) surfaces of bulk fcc(110) crystals. The magnitude of relaxation is, however, highly dependent on coverage. In the case of the one-monolayer film, the first interlayer spacing is contracted by 11.0% relative to the bulk-truncated geometry of the substrate, and the second interlayer spacing is expanded by 6.6%. In the case of the two-monolayer film, the first interlayer spacing is contracted by 6.6%, and the second interlayer spacing is expanded by 4.4%. These results indicate that

the substrate exerts considerable electronic influence on the overlayer. The presence of strong interfacial bonding in the case of the one-monolayer film is consistent with the fact that this film does not reconstruct upon annealing.

c) The (1x2) structure of Pt on Pd(110) essentially mimics that of the clean surface of bulk Pt(110). The topmost layer is of the missing-row type, the second layer is slightly row paired (0.06 Å), and the third layer is significantly rumpled (0.23 Å). Pairing occurs toward the missing row, and the upper atom of the rumpled layer is directly beneath the missing row. The directions of these displacive movements are consistent with a reduction in the large corrugation of the (1x2) missing-row structure. As for the interlayer spacings, the first interlayer spacing is contracted by 9.5% relative to the bulk-truncated geometry of the substrate, the second interlayer spacing is contracted by 8.0%, the third interlayer spacing is contracted by 7.3%, and the fourth interlayer spacing is expanded by 2.2%. The contraction of the first interlayer spacing is only about half as much as that of the clean surface of bulk Pt(110), which may be due to a combination of lattice strain and overlayer-substrate electronic effects. The ideal coverage of the (1x2) phase is 2.5 monolayers, which is 0.5 monolayers higher than the actual coverage. Therefore, it is unlikely that the (1x2) phase forms a continuous overlayer. The elongation of the half-order LEED spots along the [001] direction is consistent with the presence of (1x2) patches, probably in the form of ribbons.

d) NiO(111) on Ni(100) is sufficiently thick that the substrate does not participate in the diffraction process, and bare Ni(100) areas are not detected. Four rather than two orientational domains of NiO(111) are

present. Although the size of the domains is large enough to produce relatively sharp LEED spots, a considerable amount of disorder is evident. The oxide film is terminated with a topmost layer of oxygen in fcc sites, and exhibits a 14.8% contraction in the first interlayer spacing. Based on comparisons to relevant studies, we believe that these results may be of general significance for unreconstructed thin films of metal oxides crystallizing in the rocksalt(111) structure. The "bulk" lattice parameters of the oxide film are uniformly compressed by 2.6% relative to bulk NiO(111), which suggests that except for surface relaxation, a distortion away from the cubic symmetry of the rocksalt lattice may not be energetically favorable. The observed lateral compression is consistent with a reduction in interfacial strain via one-dimensional row matching between the overlayer and substrate.

# REFERENCES CITED


1. The fcc(311) surface is one example of a surface with only one mirror plane of symmetry. For a compilation of fcc(311) surface geometries, see Y.S. Li, F. Jona and P.M. Marcus, Phys. Rev. B 44 (1991) 8267.
2. For example, see the following paper on the surface geometry of MgO(100): M.R. Welton-Cook and W. Berndt, J. Phys. C 15 (1982) 5691.
3. For examples of experimental results on relaxation of metal surfaces, see J.M. MacLauren, J.B. Pendry, P.J. Rous and D.K. Saldin, Surface Crystallography Information Service (D. Reidel, Boston, 1987), and F. Jona and P.M. Marcus, in: The Structure of Surfaces II, Eds. J.F. Van der Veen and M.A. Van Hove (Springer, Berlin, 1987) p. 90.
4. For examples of theoretical results on relaxation of metal surfaces, see S.B. Sinnott, M.S. Stave, T.J. Raeker and A.E. DePristo, Phys. Rev. B 44 (1991) 8927.
5. R. Smoluchowski, Phys. Rev. 60 (1941) 661.
6. M.W. Finnis and V. Heine, J. Phys. F 4 (1974) L37.
7. U. Landman, R.N. Hill and M. Mostoller, Phys. Rev. B 21 (1980) 448.
8. R.N. Barnett, U. Landman and C.L. Cleveland, Phys. Rev. B 27 (1983) 6534.
9. R.N. Barnett, U. Landman and C.L. Cleveland, Phys. Rev. B 28 (1983) 1685.
10. P. Jiang, P.M. Marcus and F. Jona, Solid State Commun. 59 (1986) 275.
11. For a recent review on reconstructions of metal surfaces, see P.A. Thiel and P.J Estrup, in: Handbook of Surface Imaging and Visualization, Ed. A.T. Hubbard (CRC Press, Boca Raton, 1993).

12. R.A. Barker, P.J. Estrup, F. Jona and P.M. Marcus, Solid State Commun. 25 (1978) 375.

13. J.A. Walker, M.K. Debe and D.A. King, Surf. Sci. 104 (1981) 405.

14. D.A. King, Physica Scripta T 4 (1983) 34.

15. G. Schmidt, H. Zagel, H. Landskron, K. Heinz, K. Müller and J.B. Pendry, Surf. Sci. 271 (1992) 416.

16. D.-M. Smilgies, P.J. Eng and I.K. Robinson, Phys. Rev. Lett. 70 (1993) 1291.

17. R.S. Daley, T.E. Felter, M.L. Hildner and P.J. Estrup, Phys. Rev. Lett. 70 (1993) 1295.

18. I. Stensgaard, L.C. Feldman and P.J. Silverman, Phys. Rev. Lett. 42 (1979) 247.

19. D. Singh, S.-H. Wei and H. Krakauer, Phys. Rev. Lett. 57 (1986) 3292.

20. J.P. Pendry, K. Heinz, W. Oed, H. Landskron, K. Müller and G. Schmidtlein, Surf. Sci. 193 (1988) L1.

21. I.K. Robinson, A.A. MacDowell, M.S. Altman, P.J. Estrup, K. Evans-Lutterodt, J.D. Brock and R.J. Rirgeneau, Phys. Rev. Lett. 62 (1989) 1294.

22. I. Stensgaard, K.G. Purcell and D.A. King, Phys. Rev. B 39 (1989) 897.

23. J. Jupille, K.G. Purcell and D.A. King, Phys. Rev. B 39 (1989) 6871.

24. L. Roelefs, T. Ramseyer, L.L. Taylor, D. Singh and H. Krakauer, Phys. Rev. B 40 (1989) 9147.

25. D.G. Kelly, R.F. Lin, M.A. Van Hove and G.A. Somorjai, Surf. Sci. 224 (1989) 97.

26. W.K. Han and S.-C. Ying, Phys. Rev. B 41 (1990) 4403.

27. W.K. Han and S.-C. Ying, Phys. Rev. B 41 (1990) 9163.

28. M. Weinert, A.J. Freeman and S. Ohnishi, Phys. Rev. Lett. 56 (1986) 2295.

29. X.W. Wang and W. Weber, Phys. Rev. Lett. 58 (1987) 1452.

30. X.W. Wang, C.T. Chan, K.M. Ho and W. Weber, Phys. Rev. Lett. 60 (1988) 2066.

31. C.Z. Wang, E. Tosatti and A. Fasolino, Phys. Rev. Lett. 60 (1988) 2661.

32. G. Binnig, H. Rohrer, Ch. Gerber and E. Weibel, Surf. Sci. 131 (1983) L379.

33. W. Moritz and D. Wolf, Surf. Sci. 163 (1985) L655.

34. C.-M. Chan and M.A. Van Hove, Surf. Sci. 171 (1986) 226.

35. E.C. Sowa, M.A. Van Hove and D.L. Adams, Surf. Sci. 199 (1988) 174.

36. P. Fery, W. Moritz and D. Wolf, Phys. Rev. B 38 (1988) 7275.

37. P. Fenter and T. Gustafsson, Phys. Rev. B 38 (1988) 10197.

38. E. Vlieg, I.K. Robinson and K. Kern, Surf. Sci. 233 (1990) 248.

39. M. Stock, J. Risse, U. Korte and G. Meyer-Emsen, Surf. Sci. 233 (1990) L243.

40. T. Gritsch, D. Coulman, R.J. Behm and G. Ertl, Surf. Sci. 257 (1991) 297.

41. F. Masson and J.W. Rabalais, Surf. Sci. 253 (1991) 245.

42. W. Hetterich, U. Korte, G. Meyer-Ehmsen and W. Heiland, Surf. Sci. 254 (1991) L487.

43. W. Hetterich and W. Heiland, Surf. Sci. 210 (1989) 129.

44. W. Hetterich, C. Höfner and W. Heiland, Surf. Sci. 251/252 (1991) 731.

45. H. Bu, M. Shi, F. Masson and J.W. Rabalais, Surf. Sci. 230 (1990) L140.

46. M. Shi, H. Bu and J.W. Rabalais, Phys. Rev. B 42 (1990) 2852.

47. H. Bu, M. Shi and J.W. Rabalais, Surf. Sci. 244 (1991) 96.

48. R. Koch, M. Borbonus, O. Haase and K.H. Rieder, Phys. Rev. Lett. 67 (1991) 3416.

49. K.M. Ho and K.-P. Bohnen, Phys. Rev. Lett. 59 (1987) 1833.

50. C.J. Barnes, M. Lindroos and D.A. King, Surf. Sci. 201 (1988) 108.

51. C.J. Barnes, M. Lindroos, D.J. Holmes and D.A. King, Surf. Sci. 219 (1989) 143.

52. R.J. Behm, in: Physics and Chemistry of Alkali Metal Adsorption, Eds. H.P. Bonzel, A.M. Bradshaw and G. Ertl (Elsevier, Amsterdam, 1989) p. 111.

53. Z.P. Hu, B.C. Pan, W.C. Fan and A. Ignatiev, 41 (1990) 9692.

54. C.L. Fu and K.M. Ho, Phys. Rev. Lett. 63 (1989) 1617.

55. M. El-Batanouny, M. Strongin, G.P. Williams and J. Colbert, Phys. Rev. Lett. 46 (1981) 269.

56. H. Niehus, C. Hiller and G. Comsa, Surf. Sci. 173 (1986) L599.

57. M. Skottke, R.J. Behm, G. Ertl, V. Penka and W. Moritz, J. Chem. Phys. 87 (1987) 6191.

58. G. Kleinle, M. Skottke, V. Penka, G. Ertl, R.J. Behm and W. Moritz, Surf. Sci. 189/190 (1987) 177.

59. J.-W. He, D.A. Harrington, K. Griffiths and P.R. Norton, Surf. Sci. 198 (1988) 413.

60. J.W.A. Sachtler, M.A. Van Hove, J.P. Biberian and G.A. Somorjai, Phys. Rev. Lett. 45 (1980) 1601.

61. J.W.A Sachtler, J.P. Biberian and G.A. Somorjai, Surf. Sci. 110 (1981) 43.

62. J.W.A. Sachtler, M.A. Van Hove, J.P. Biberian and G.A. Somorjai, Surf. Sci. 110 (1981) 19.

63. S.M. Francis and N.V. Richardson, Phys. Rev. B 33 (1986) 662.

64. M. Wolf, A. Goschnick, J. Loboda-Cacković, M. Grunze, W.N. Unertl and J.H. Block, Surf. Sci. 182 (1987) 489.

65. A.M. Lahee, J.P. Tonnies and Ch. Wöll, Surf. Sci. 191 (1987) 529.

66. M. Guillopé and B. Legrand, Surf. Sci. 215 (1989) 577.

67. J.B. Pendry, Low Energy Electron Diffraction (Academic Press, New York, 1974).

68. M.A. Van Hove and S.Y. Tong, Surface Crystallography by LEED (Springer, Berlin, 1979).

69. P.M. Marcus and F. Jona, Eds., Determination of Surface Structure by LEED (Plenum, New York, 1984).

70. L.J. Clarke, Surface Crystallography (Wiley, New York, 1985).

71. M.A. Van Hove, W.H. Weinberg and C.-M. Chan, Low-Energy Electron Diffraction (Springer, Berlin, 1986).

# ACKNOWLEDGEMENTS

I am grateful for the support, patience, and guidance that my advisor, Professor Patricia Thiel, has provided over the past four and a half years. Her willingness to allow me considerable latitude in my research efforts will always be cherished.

I acknowledge others who have made significant contributions to my research. I thank Robert Mann, Tim Pope, and Professor Peter Norton at the University of Western Ontario, Canada for showing me the details of their video LEED system. In particular, a conversation with Robert opened my eyes to the error of my ways in C programming. I thank Petri Kaukasoina and Professor Matti Lindroos at the Tampere University of Technology, Finland for collaborating on the Pt/Pd(110)-(1x2) project. I thank Trang Vu Grimsby and Professor Keith Mitchell at the University of British Columbia, Canada for the wonderful two weeks spent in the beautiful city of Vancouver for the purpose of learning the computational aspects of dynamical LEED analysis. Never before have I seen such majestic mountains so near shore. I thank Professor Michel Van Hove at the University of California-Berkeley for supplying the LEED package and phase shifts, which has allowed us to conduct our research without reinventing the wheel.

Many past and present members of the Thiel group have made my time in Ames enjoyable. I am indebted to Dr. Diane Sanders for her skill in teaching me the essentials of ultrahigh-vacuum surface science during my first few months in the lab. I appreciate the conversions with Mark Jensen over the merits of being a fan of the Cincinnati Reds (Mark follows the Chicago Cubs). I have enjoyed the friendship of Dr. Barb Nielsen and

family (Chris, Birgitte, Steffen), Dr. Mike Columbia, and Dr. Joe Burnett.

Others have also made my time in Ames memorable. I appreciate the many political and not so political discussions with Luther Schmidt, John Morris, Nancy Benz, and Dave McGregor during lunch. I have enjoyed the friendship of Sonjong Hwang, Dr. Sadri Housseni, and Dr. Dan Smith. I will miss the "friendly" competition between the members of the Chemistry Fantasy Football League.

I am especially indebted to my wife, Beth, and to my son, Fletcher, for keeping life in perspective. I am truly blessed by their presence. I am grateful to my family (Mom, Edmond, Lydia) and to my wife's family (Bill, Mary, Martha) for making me feel at home whenever I return to my old stomping grounds in Ohio. I am indebted to Dr. Subrata Gosh, who kindled my interest in chemistry, and to Professor Vladimir Katovic at Wright State University, who fueled it further. I thank God for making everything possible.

I am grateful for having received financial support from an Amoco Foundation Fellowship, and from a GAANN Fellowship via the U.S. Department of Education. Funding for this work comes primarily from the National Science Foundation through Grant No. CHE-9014214 and GER-9024358, and from the Ford Motor Company. This work was performed at Ames Laboratory under Contract No. W-7405-ENG-82 with the U.S. Department of Energy. The United States government has assigned the DOE Report number IS-T 1660 to this dissertation.

# APPENDIX:

## VIDEO LEED PROGRAM

# I. INTRODUCTION

Video LEED is a technique in which video technology is used to measure the intensity (or the intensity distribution) of a LEED spot displayed on a phosphor screen. The advantage of this technique over more traditional methods, such as the Faraday cup method or the spot photometer method, is the rate at which data can be collected. Whereas the more traditional methods require time-consuming mechanical motion, video LEED is based entirely on digitized video signal, and is thus very fast. For example, while the time required to measure a single I(E) curve can exceed 1 hr when using either the Faraday cup method or the spot photometer method, a typical video LEED system can collect a complete set of curves in about 10 min.

The purpose of this appendix is to document the computer program written for our video LEED system for the benefit of future users.

# II. HARDWARE CONSIDERATIONS

## A. System Overview

The video LEED system consists of the following hardware components: 8/16 MHz Arche Pro-File 286 computer (IBM-AT clone), Matrox MVP-AT video processor board, beam energy controller (comprised of a Data Translation DT2801-A analog and digital I/O board and a Burr-Brown 3656 isolation amplifier), Dage-MTI SIT-66 video camera, and a suitable B/W television monitor. Connections between the hardware components are shown in Fig. 1.

## B. Computer Requirements

The computer must meet the following specifications in order for the software to run properly: 1) Sufficient RAM must be available at run time. Although 640 kbytes of low memory has proven to be more than enough, the amount of RAM actually needed at run time is difficult to estimate due to the fact that the software makes extensive use of dynamical memory allocation. 2) A storage device with drive specification E: must be available for writing output files. The computer in current use assigns drive specification E: to a 3 Mbyte RAM drive in order to maximize the rate of data transfer. 3) The video card and the computer monitor must be compatible with EGA color graphics. 4) An 80287 math coprocessor must be available for floating point operations. The computer in current use is peculiar in the sense that the math coprocessor will not operate properly unless the CPU speed is set to 16 MHz. 5) The I/O bus speed must be no faster than 8 MHz.

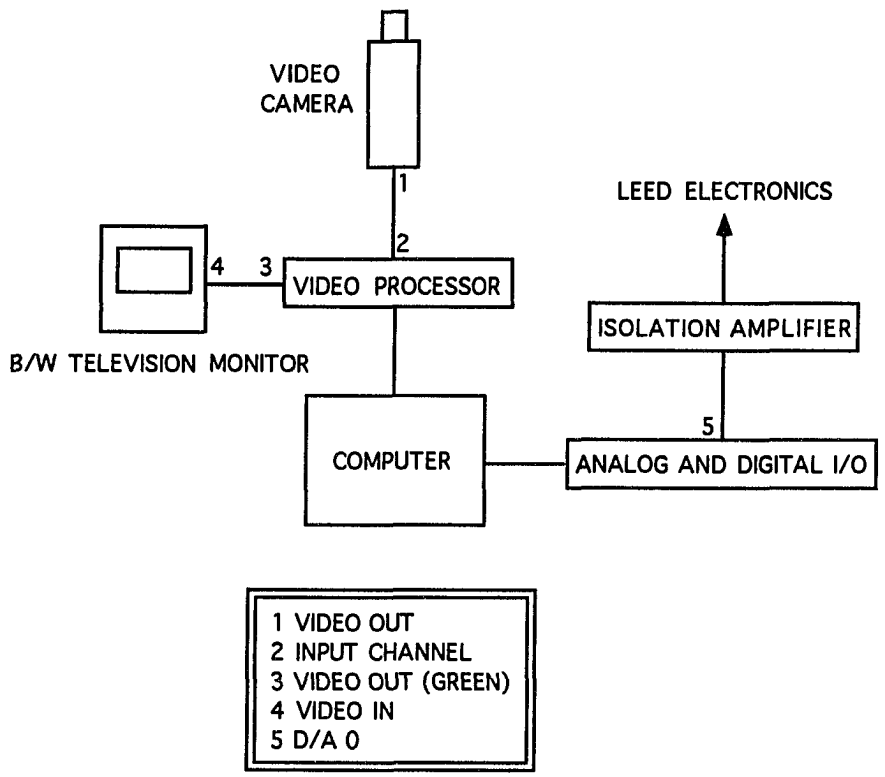


Figure 1. Connections between the hardware components of the video LEED system

## C. Video Processor

Memory segment and I/O base addresses must be selected for interfacing the video processor to the computer. Values found to be compatible with the computer in current use are $D000_{16}$ and $340\text{-}35F_{16}$, respectively.

Input decoders digitize the analog output of the video camera at a full-frame rate of 30 Hz, with a spatial resolution of 512x480 pixels. The intensity resolution is 8 bits, which corresponds to a gray scale of 0-255. Programmable offset and gain logic determines the reference voltages used in the decoding procedure. Intensities below the black level are set to 0; intensities above the white level are set to 255.

After the input decoders have performed their task, the decoded intensities are mapped onto the input lookup table (ILUT). The ILUT is an 8-kbyte memory device divided into 32 palettes, each consisting of 256 bytes. While palettes 16-31 are reserved for internal use by the video processor, palettes 0-15 are available for the user to define by storing a value from 0-255 at each byte location.

The result of the ILUT mapping procedure is determined by the decoded intensities and the values residing in the active palette of the ILUT. For example, if the decoded intensity of a particular pixel is 50 and the active palette is palette 0, then the value residing at the 50th byte location in palette 0 is stored at the location in video memory corresponding to the spatial coordinates of the pixel. The software uses palette 0 as the active palette, and a 1:1 correspondence between the decoded intensities and the stored intensities is employed. It is important to note that the ILUT must be scaled in reverse order relative to the decoded intensities, i.e., the value at the first byte location in

palette 0 is 255 rather than 0.

The video memory consists of four frame buffers (FB0-FB3) totalling 1 Mbyte of RAM. Each frame buffer can be thought of as an 8-bit-deep array of 512x512 pixels. Since the spatial resolution of the decoded image is 512x480 pixels, the last 32 lines correspond to garbage. In practice, the 480th line is also found to be garbage, so only the first 479 lines are accessed by the software.

The software combines FB2 and FB3 into one 16-bit-deep frame buffer referred to as FB5. FB5 is used to store the sum of several images taken in succession, which serves as a filter to increase the signal-to-noise ratio. The portion of FB5 that corresponds to FB2 is used to store the low-byte component of the accumulated image, and the portion of FB5 that corresponds to FB3 is used to store the high-byte component of the accumulated image. FB0 is used to store the contents of FB5 after normalizing with respect to the number of frames included in the summation, and FB1 is used to store overlays. The primary purpose of overlays is to allow the software to generate windows for defining areas over which intensities can be extracted.

An image stored in video memory can be viewed on the B/W monitor after the contents of the frame buffer selected for display (always an 8-bit-deep frame buffer) are mapped onto the output lookup table (OLUT). The OLUT is an 8-kbyte memory device divided into 32 palettes, each consisting of 256 bytes. Unlike the ILUT, all 32 palettes of the OLUT are available for the user to define.

The following is a description of the OLUT mapping procedure used by the software: 1) If only the contents of FB0, FB2, or FB3 are displayed,

then the mapping procedure is done in exactly the same manner as described for the ILUT. The software uses palette 0 as the active palette, and a 1:1 correspondence between the stored intensities and the displayed intensities is employed. To avoid confusion, it is noted that the OLUT must be scaled in the same order as the intensities stored in video memory. 2) If the contents of FB0 are also displayed for the purpose of overlays, then the value of the low nibble of each pixel in FB0 corresponds to a palette index. For example, if the value of the low nibble of a particular pixel is 0, then the corresponding palette is palette 0, and the intensity of the corresponding pixel in FB0, FB2, or FB3 is displayed. However, if the value of the low nibble is nonzero, then the value represents a palette index ranging from 1-15, and the intensity stored throughout the appropriate palette is displayed. The software floods palette 1 with 0's, and floods palette 15 with 255's. Intermediate palettes are flooded with intermediate values.

## D. Beam Energy Controller

The beam energy can be controlled with the computer by programming the D/A 0 output (0-5 V, 12 bits) of the analog and digital I/O board, which is connected to the LEED electronics through an isolation amplifier configured for three-port isolation, noninversion, and unity gain. A programmed voltage of 0 V corresponds to a beam energy of ca. 0 eV, and a programmed voltage of 1 V corresponds to a beam energy of ca. 300 eV. It is important to note that although the isolation amplifier can withstand up to 8 V applied to its input, the LEED electronics can take no more than 5 V without damage.

The isolation amplifier serves the purpose of isolating the LEED electronics from the video LEED system. The necessity of this arises from the fact that the voltage sent to the LEED electronics must be referenced to the power common of the LEED control module rather than earth ground. A schematic of the circuitry involved in making the connections between the isolation amplifier, the analog and digital I/O board, and the LEED electronics is shown in Fig. 2.

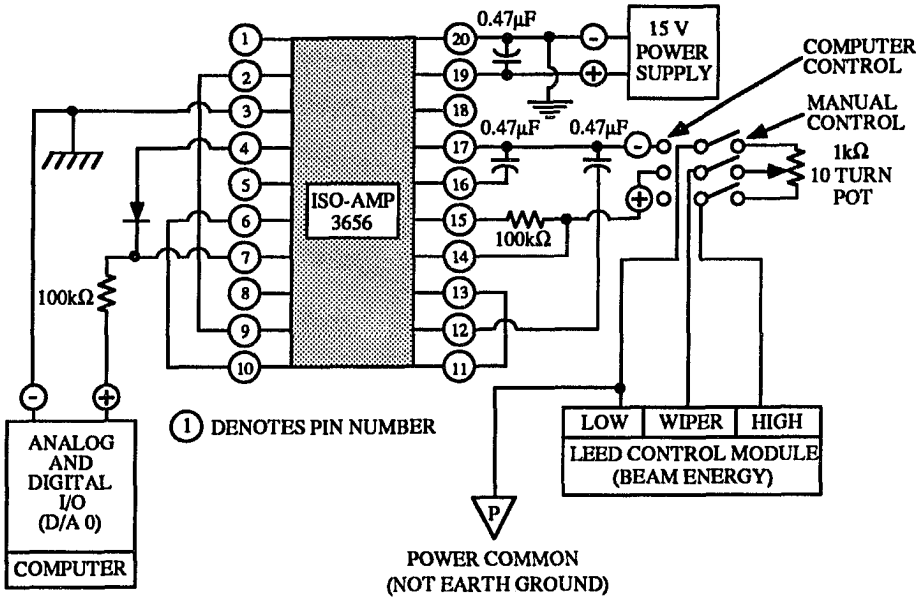


Figure 2. Schematic of the beam energy controller

# III. SOFTWARE CONSIDERATIONS

ACQUIRE.EXE is a menu-driven program written in the C programming language. Its sole purpose is to collect LEED data. Other programs are required for data manipulation and conversion of binary files to text files, but due to their small size, they are not documented in this appendix.

ACQUIRE.EXE must be able to access the contents of the following files: DEFAULT.LDP, HALOAWON.DEV, and ANSI.SYS. DEFAULT.LDP contains default window parameters and HALOAWON.DEV is a device driver supplied with the Halo graphics package, which is used to display EGA color graphics. Both files must reside in the same directory as ACQUIRE.EXE, so that ACQUIRE.EXE can find them upon program initiation. ANSI.SYS is used primarily to interpret extended key codes, such as for F and cursor keys, and is loaded into memory upon booting up the computer when the following line appears in CONFIG.SYS: device =pathname\ANSI.SYS, where pathname describes where ANSI.SYS is stored.

ACQUIRE.EXE is comprised of eleven object modules: ACQUIRE.OBJ, SETUP.OBJ, WINDOWS.OBJ, DATA.OBJ, ENERGY.OBJ, TIMERAMP.OBJ, ALIGN.OBJ, DTOA.OBJ, FWHM.OBJ, COMMON.OBJ, and HALODVXX.OBJ. The first ten modules are generated by compiling corresponding source code files with the .C file extension, e.g., ACQUIRE.C. The last module is supplied with the Halo graphics package; therefore, no source code file is available.

Compiling and linking is accomplished with the Microsoft C 5.0 Optimizing Compiler package. Libraries needed in addition to those supplied with the compiler package are MVPLM.LIB and HALOUL.LIB. MVPLM.LIB

contains object code for Matrox functions and HALOUL.LIB contains object code for Halo functions. To facilitate linking, both libraries should reside in the same directory as the libraries provided with the compiler package. Header files needed in addition to those supplied with the compiler package are LEED.H, MVPPROTO.H, and IM2TO3.H. [Include statements in the source code files are written such that these files must reside in the same directory as the source code files.] LEED.H provides definitions for constants and data types appearing in the source code files; MVPPROTO.H provides prototypes, base addresses, and error codes for Matrox functions; and IM2TO3.H adds the required im_ prefix to Matrox functions, which does not appear explicitly in the source code files. [IM2TO3.H is included in MVPPROTO.H, so its inclusion in the source code files is not readily apparent.] If one wishes to write additional source code files for ACQUIRE.EXE, then one needs to remember that LEED.H must be included before MVPPROTO.H. This is due to the fact that LEED.H contains definitions of data types appearing in MVPPROTO.H.

An environment suitable for the compiler package must be set up prior to compiling and linking. The easiest way to accomplish this is to execute MSEA.BAT. To restore the default environment, execute AUTOEXEC.BAT.

Compiling is initiated by entering the following command line: cl /c /G2 /FPi87 /AL /W3 FILENAME.C, where FILENAME is to be understood as a generic file name. [The C programming language is case sensitive, so the command line must be entered as shown.] Switches appearing in the command line are defined as follows: compile without linking, use 80286 CPU instructions, use 80287 in-line math coprocessor instructions for floating point operations, select the large memory model, and compile with the

highest warning level with regard to syntax errors. The large memory model allows for multiple 64-kbyte code and data segments, and is the only memory model compatible with MVPLM.LIB and HALOUL.LIB.

Linking is accomplished by executing ACQLINK.BAT. [ACQLINK.BAT is specific to ACQUIRE.EXE, and must reside in the same directory as the object modules.] The following switch appears in the command line stored in ACQLINK.BAT: /ST:10000. This switch sets the stack size to 10,000 bytes, which has proven to be sufficient thus far. During the linking procedure, you will be prompted to provide additional libraries. At this point, enter the following: MVPLM+HALOUL. If modifications are made to ACQUIRE.EXE, then ACQLINK.BAT may also need to be modified to reflect the new program structure.

# IV. USING ACQUIRE.EXE

## A. Program Introduction

Five major menus are incorporated into ACQUIRE.EXE: ACQUIRE, SETUP, WINDOWS, DATA, and IMAGE. Connections between these menus are shown in Fig. 3. To select an option from a menu, move the highlight bar to the desired option with [↑] or [↓], then press [Enter]. To return to the previous menu, press [Esc]. (Pressing [Esc] is the standard procedure used in ACQUIRE.EXE for exiting features with menu characteristics.) As is evident in Fig. 3, IMAGE differs from the other menus in the respect that it does not appear as a selectable option. IMAGE is selected instead by pressing [F2] when in ACQUIRE, SETUP, WINDOWS, or DATA.

ACQUIRE.EXE offers two other major features in addition to the five major menus: a window editor, and a table of current values for parameters other than window parameters. The table of current values can be displayed by pressing [F1] when in ACQUIRE, SETUP, WINDOWS, or DATA. To exit from this table, press any key. [Pressing any key is the standard procedure used in ACQUIRE.EXE for terminating optionless displays.] The window editor is discussed later.

Many selectable options will result in a prompt for input followed by the current value of the parameter of interest. If the current value is satisfactory, either press [Esc] or ensure that the cursor position resides completely to the left and press [Enter]. Following either of these two procedures will result in no change in the value of the parameter. In some cases, a line representing the maximum storage space allocated for the input character string will appear below the cursor. To avoid overflowing

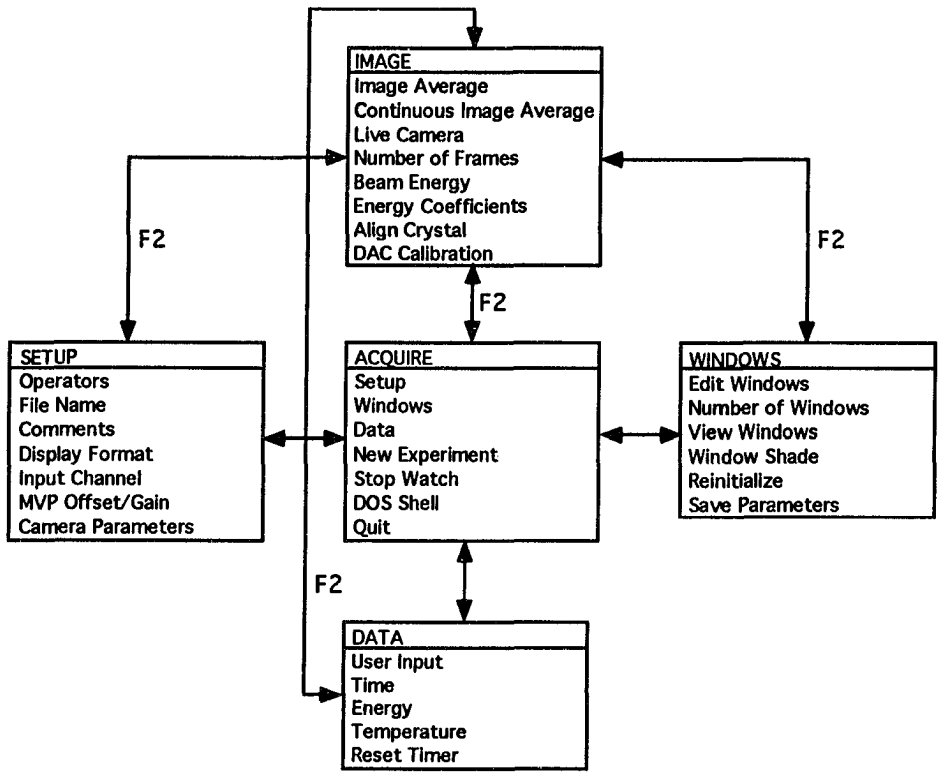


Figure 3. Connections between the major menus incorporated into ACQUIRE.EXE

the allocated storage space, do not input beyond this line.

To execute a DOS command while in ACQUIRE.EXE, select DOS Shell in ACQUIRE. To return to ACQUIRE.EXE, enter the following character string: exit.

If a timer is needed, select Stop Watch in ACQUIRE. The computer will respond with a continuous series of beeps once the entered amount of time has elapsed. To terminate the beeps, press any key.

## B. Initial Setup

Date and time of program initiation are stored automatically. Names of the operators, comments, output file name (DOS restrictions apply), and camera parameters can be stored by selecting the appropriate option in SETUP. The output file name is initially set to UNTITLED, and is again set to UNTITLED after each experiment so that an accidental overwrite of the previous experiment does not occur. File extensions are appended automatically, so do not add one when entering the output file name.

ACQUIRE.EXE assumes that the video camera is connected to input channel 0 of the video processor. If the video camera is connected to a different input channel, select Input Channel in SETUP to change the channel.

Frame grabbing and live video features reside in IMAGE. To capture an image, select Image Average. To capture images repetitively, select Continuous Image Average. The default value for the number of frames accumulated in an image is 16. To change this value, select Number of Frames. To view the live video input, select Live Camera.

Three formats are available for the video output to the B/W monitor:

normalized, accumulated low byte, and accumulated high byte. Normalized format displays the normalized image, accumulated low-byte format displays the low-byte component of the accumulated image, and accumulated high-byte format displays the high-byte component of the accumulated image. The default setting is normalized format. To change the format, select Display Format in SETUP. It is important to note that ACQUIRE.EXE is written such that the video synchronization signal must be supplied by the camera; thus, the video camera must remain on when viewing digitized images.

The offset setting of the video processor ranges from 0-255, where 0 corresponds to a black level voltage (BLV) of 0.2 V and 255 corresponds to a BLV of -0.2 V. The gain setting of the video processor ranges from 0-255, where 0 corresponds to a white level voltage (WLV) of (BLV+0.63) V and 255 corresponds to a WLV of (BLV+1.03) V. Default values for the offset and gain settings are 51 and 204, respectively. To change these values, select MVP Offset/Gain in SETUP. Since WLV depends on BLV, one should change the offset setting before changing the gain setting.

The MVP Offset/Gain option also allows the user to display the following: a histogram (a plot of the number of pixels versus intensity) of the normalized image, and a table of the number of pixels in the normalized image with intensities of 0-19 and 236-255. These two features allow the user to quantitate the change in the intensity distribution when adjusting the offset and gain settings. Ideally, all intensities in the normalized image should be greater than 0 and less than 255. Otherwise, the image is either undersaturated or oversaturated.

Features for controlling the beam energy with the computer reside in IMAGE. To calibrate the D/A 0 output of the analog and digital I/O board,

select DAC Calibration and enter a DAC value in the range of 0-1000. After entering the DAC value, observe the beam energy reading on the panel meter of the LEED electronics. Repeat this procedure until the relationship between DAC value and beam energy is established. Typically, DAC values of 200, 400, 600, 800, and 1000 are sufficient to determine an accurate slope and intercept for the y =mx+b equation of DAC value versus beam energy. [The coefficients m and b can be determined by performing linear regression on a suitable calculator.] To enter the slope and intercept (default values are m =3.0990 and b =-1.7969), select Energy Coefficients. To set the beam energy to the desired value, select Beam Energy.

## C. Options in WINDOWS

Windows are drawn as rectangular (or square) boxes. To adjust the hue of the borders of the box, select Window Shade. A window shade of 1 corresponds to black and a window shade of 15 corresponds to white. The default window shade is white.

Up to twenty windows can be defined at one time. This number, however, can be reduced by selecting Number of Windows. Setting the number of windows to the actual number needed (default value is 10) reduces the amount of time spent in loops involving window parameters.

Each window can have up to six window types at one time: *X Profile*, *Y Profile*, *Mean Horizontal Profile*, *Mean Vertical Profile*, *Integrated Intensity*, and *Block Transfer*. *X Profile* corresponds to a single-line profile taken in the x (horizontal) direction, and *Y Profile* corresponds to a single-line profile taken in the y (vertical) direction. *Mean Horizontal Profile* corresponds to a profile representing the sum of all x profiles

bounded by the window, and *Mean Vertical Profile* corresponds to a profile representing the sum of all y profiles bounded by the window. The actual summing procedure is, however, somewhat different than implied above. Mean horizontal profiles are obtained by summing each column of pixels bounded by the window and mean vertical profiles are obtained by summing each row of pixels bounded by the window. *Integrated Intensity* corresponds to the net integrated intensity of the window after subtracting the background intensity. The background intensity is defined as the average intensity on the border of the window multiplied by the total number of pixels in the window. *Block Transfer* corresponds to a point-by-point extraction of all pixels within the window. This provides the capability for generating 3-D profiles. If at least one of the six window types has been selected for a window, then the window is considered to be active. Conversely, if no window types have been selected for a window, then the window is considered to be inactive. For further clarification of window types, see Fig. 4.

Selecting Edit Windows brings up the window editor. Connections between the main components of the window editor are shown in Fig. 5.

The upper portion of Fig. 5 shows a table containing window numbers from 0 to (number of windows-1). This table signals the user to enter a window number for editing. If the normalized intensity of the center pixel of the window is displayed along side the window number, then the window is active. This allows the user to quickly differentiate between active and inactive windows.

The middle portion of Fig. 5 shows the core level of the window editor. Within this level, one can establish the following: name of the window, position of the window, dimensions of the window, sampling area

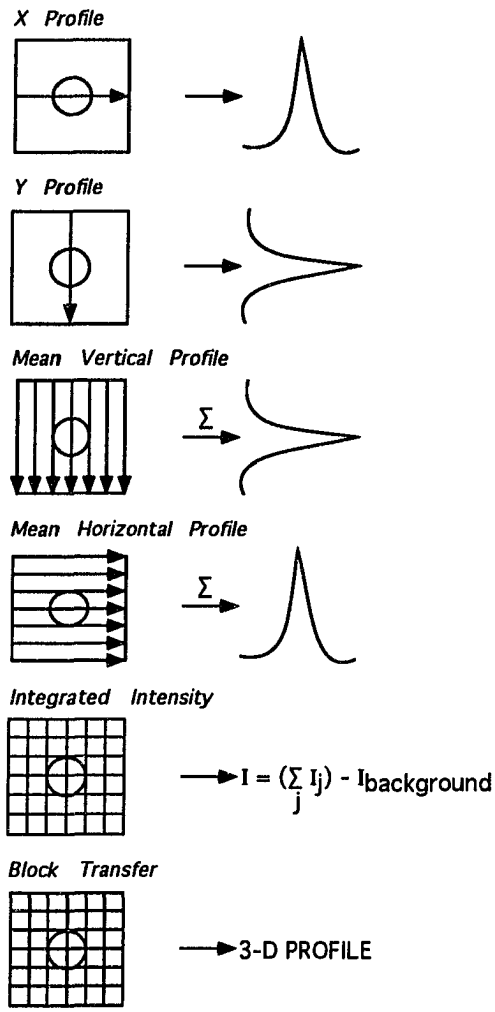


Figure 4. Pictorial representation of the six window types

Arrows drawn within the windows represent single-line profiles. Intersections of lines in cross-hatched windows represent discrete pixels.

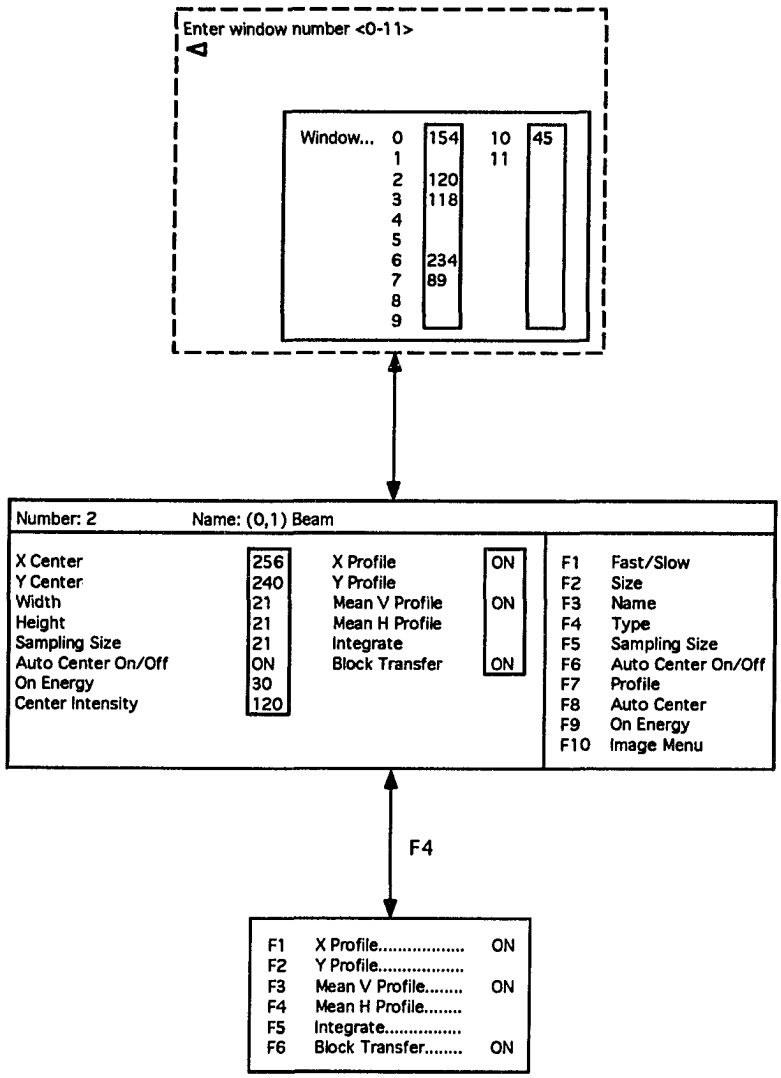


Figure 5. Connections between the main components of the window editor

used for auto centering, whether to auto center during an experiment, energy at which the window is activated when ramping the beam energy, and window types. Descriptions of these parameters, and procedures required to edit these parameters, are given below.

The name of the window allows the user to correlate windows with beam indices. For example, a window intended for the (0,1) spot can be named (0,1). To enter the name of the window, press [F3].

The position of the window is defined as the (x,y) coordinates of the center of the window. The coordinates of the upper lefthand corner of the image is (0,0), and the coordinates of the lower righthand corner of the image is (511,478). To change the position, use the cursor keys or the equivalent keys in the numeric keypad when [Num Lock] is off. Use of the numeric keypad also allows the user to move the window in diagonal directions. If the top of the image is taken to be north, then [Home] moves the window NNW, [Pg Up] moves the window NNE, [Pg Dn] moves the window SSE, and [End] moves the window SSW. To toggle the step size between one and ten-pixel increments, press [F1]. The display of the normalized intensity of the center pixel of the window is continuously updated during the positioning procedure.

The dimensions of the window determine factors such as the length of profiles and the area used in obtaining integrated intensities. Only one restriction is placed on the dimensions—the window cannot wrap around the boundaries of the frame buffer. [This restriction also applies when changing the position of the window.] To change the dimensions of the window, press [F2]. After pressing [F2], the cursor keys are interpreted in terms of size changes rather than position changes. To toggle the step

size between two and twenty-pixel increments, press [F1]. Once the dimensions of the window have been set, press [Enter] or [Esc] to register the changes.

After setting the dimensions of the window, one may wish to observe x and y profiles to determine whether the intensity distribution of a spot has reached the background level at the borders of the window. To view profiles, press [F7]. The profiles are extracted from the normalized frame buffer, and are drawn twice: on a scale of 0-255, and on a scale of 0-1 after normalizing the profile with respect to the peak intensity of the profile.

Auto centering refers to centering the window automatically on the most intense pixel in the sampling area. The sampling area is an invisible square box centered at the original coordinates of the window. To set the size of the sampling area, press [F5]. To center the window automatically, press [F8]. Auto centering can also be performed while collecting data when the auto centering toggle is in the on state. To toggle auto centering between on and off, press [F6]. It is important to note that auto centering is performed only when the signal can be differentiated from the noise. To determine whether the brightest pixel actually corresponds to a spot, the FWHM of the profile is calculated after subtracting a linear background. If the profile crosses the half-height level more than twice, then the brightest pixel is considered to be noise and no change in the position of the window is made. This algorithm has proven to be essential in collecting I(E) curves since spots often exhibit near zero intensity over a continuous energy range of a few eV. By holding the window at the last valid position until the spot again achieves sufficient intensity, the

window is prevented from wandering aimlessly over pixels corresponding to noise.

The beam energy is always ramped positively; therefore, spots corresponding to different orders of diffraction appear on the phosphor screen at different energies. So that a window can be ignored until the spot actually appears on the screen, an energy at which the window is activated is required. To set this energy, press [F9].

The lower portion of Fig. 5 shows a table containing window types. This table can be selected by pressing [F4]. To toggle window types between on and off, press the F keys listed in the table. After selecting the desired window types, press [Enter] or [Esc] to register the changes.

IMAGE often needs to be accessed while in the window editor. To access IMAGE, press [F10].

The remaining options in WINDOWS allow the user to view, save, and reinitialize window parameters. To view a table of current values for parameters associated with windows 0 to (number of windows-1), along with a display of the active windows, select View Windows. To save window parameters to the current working directory, select Save Parameters. The name of the resulting file is FILENAME.LDP. To reinitialize the window parameters to the contents of a previously saved FILENAME.LDP file, select Reinitialize. When prompted for the name of the file, omit the .LDP file extension.

## D. Collecting Data

Intensities can be collected as a function of time (s), energy (eV), or user input (a.u.). To collect intensities as a function of one of these

three independent variables (or x parameters), select the appropriate option in DATA. [Temperature also appears as an option in DATA, but the corresponding routine is still in the development stage.]

Experiments with time as the independent variable are done in a loopwise manner, i.e., they continue until they are terminated by the user. The time stored in the output files is always referenced to the reference time, which is the time of program initiation by default. To change the reference time, select Reset Timer in DATA.

Experiments with energy as the independent variable are also done in a loopwise manner, i.e., they continue until the end of the ramp is reached, or until the user intervenes by terminating the ramp manually. It is important to note that the user views the live video input rather than the digitized image during an energy experiment. This is necessitated by the fact that the constant updating of window positions due to the changing spot positions results in sluggish behavior if the digitized image is viewed.

If I(E) curves are to be collected, then the crystal must be aligned. For establishing normal incidence, select Align Crystal in IMAGE to see I(E) curves plotted in real time. [The curves are not saved during the plotting procedure.] Seeing the curves in real time allows the user to quickly rotate the crystal until symmetry-equivalent curves become as identical as practically possible. Although twenty curves can be plotted at one time (one for each of the twenty possible windows), only four pen colors are available. Curves corresponding to windows 0, 1, 2, and 3 are plotted in black, blue, green, and red, respectively. If more than four windows are used, then the cycle simply repeats itself. As is the case

with energy experiments, the user views the live video input rather than the digitized image when aligning the crystal.

Experiments with user input as the independent variable are noncontinuous, i.e., the user is free to explore the remainder of ACQUIRE.EXE. However, user input experiments can still be performed in a loopwise manner if desired. Features unique to the user input "loop" are the following: 1) The output files can be overwritten in midstream. The Back One option overwrites the data collected from the previous image, and the Rewind option overwrites the entire experiment. 2) Windows can be edited with the window editor directly after the current image has been digitized. 3) You can opt to not save data from the current image.

During the course of an experiment, two output files are generated: FILENAME.LDR and FILENAME.LDD. These files are written to the RAM drive, and remain open until closed with New Experiment or Quit in ACQUIRE. [New Experiment allows the user to stay in ACQUIRE.EXE; Quit terminates the program.] After selecting one of these two options, the contents of FILENAME.LDR and FILENAME.LDD are saved to the current working directory. If an error occurs during the saving procedure, choose Abort from DOS and do not delete the files from the RAM drive when prompted. If not deleted, the files can be recovered with the following procedure: select DOS Shell in ACQUIRE, then copy the files from the RAM drive to a floppy disk. Remember that the RAM drive is only a temporary storage device, so one should close and save the files immediately. It is important to note that FILENAME.LDR and FILENAME.LDD are limited to 1,200,000 bytes in order to ensure that they do not exceed the floppy disk limit. Once either file reaches the maximum size, you will be prompted to terminate the experiment

and save.

Upon selecting either the New Experiment option or the Quit option, you will be prompted as to whether to save a summary file to the current working directory. The resulting FILENAME.LDS file serves the purpose of saving values of parameters not included in FILENAME.LDR or FILENAME.LDD. The information stored in FILENAME.LDS reflects the values of the parameters just prior to saving; therefore, if an accurate reflection of the experiment is desired, do not change the values of the parameters before FILENAME.LDS has been saved.

# V. OUTPUT FILE FORMATS

## A. Output File Overview

FILENAME.LDP stores window parameters, FILENAME.LDR stores records for the intensities, FILENAME.LDD stores the intensities, and FILENAME.LDS stores additional information about the experiment. The first three files are written in binary mode and the last file is written in text mode.

## B. Format of FILENAME.LDP

FILENAME.LDP stores twenty records containing window parameters for the twenty possible windows. The records are written in order according to the window number, e.g., the record for window 0 is written first and the record for window 19 is written last.

Each record is represented by the following structure type defined in LEED.H:

```
/*definition of structure type WINDOW-----------------------------------*/
typedef struct{
 char name[21]; /*name of the window*/
 char xprofile; /*toggle for X Profile*/
 char yprofile; /*toggle for Y Profile*/
 char rowsums; /*toggle for Mean Vertical Profile*/
 char colsums; /*toggle for Mean Horizontal Profile*/
 char integrate; /*toggle for Integrated Intensity*/
 char block; /*toggle for Block Transfer*/
 char autocenter; /*toggle for auto centering*/
```

```
 int x; /*x coordinate of the center of the window*/
 int y; /*y coordinate of the center of the window*/
 int halfwidth; /*determines the width of the window*/
 int halfheight; /*determines the height of the window*/
 int samplesize; /*determines the sampling area used in auto centering*/
 int ev; /*energy at which the window is activated when the beam energy is
 ramped*/
 }WINDOW;
/*end of definition-----------------------------------------------------*/
```

Further explanations for some of the parameters are as follows: 1) Each of the seven toggles can take on values of 0 or 1, where 0 represents the inactive state and 1 represents the active state. 2) (2*halfwidth+1) defines the width of the window and (2*halfheight+1) defines the height of the window. 3) (2*samplesize+1) defines both the width and the height of the sampling area used in auto centering.

The easiest way to access the information stored in FILENAME.LDP is to bring FILENAME.LDP into ACQUIRE.EXE by following the procedure described previously. An alternative method is to read FILENAME.LDP with RPRAMS.EXE. [RPRAMS.EXE is a small program used to display FILENAME.LDP as text.] This method has the advantage of allowing the user to dump the contents of FILENAME.LDP to a line printer by pressing [Print Scrn].

If modifications are made to ACQUIRE.EXE concerning the structure of the window parameters, then a new DEFAULT.LDP file reflecting the changes must be generated. To accomplish this, edit WPRAMS.C to produce a new WPRAMS.EXE program. [WPRAMS.EXE is a small program used to generate

DEFAULT.LDP.] Of course, RPRAMS.C will also need to be edited to produce a new RPRAMS.EXE program.

### C. Formats of FILENAME.LDR and FILENAME.LDD

Each record stored in FILENAME.LDR is represented by the following structure type defined in LEED.H:

```
/*definition of structure type RECORD-----------------------------------*/
typedef struct{
 char number; /*window number*/
 char type; /*window type*/
 int frames; /*number of frames accumulated in an image*/
 float xpvalue; /*value of the independent variable*/
 float xp2value; /*value of the secondary independent variable*/
 int x; /*x coordinate of the center of the window*/
 int y; /*y coordinate of the center of the window*/
 int width; /*width of the window*/
 int height; /*height of the window*/
 long lddoffset; /*file pointer in FILENAME.LDD*/
 }RECORD;
/*end of definition-----------------------------------------------------*/
```

Further explanations for some of the parameters are as follows: 1) Window types are represented by the ASCII code equivalents of the following characters: 'X' for *X Profile*, 'Y' for *Y Profile*, 'R' for *Mean Vertical Profile* (row sums), 'C' for *Mean Horizontal Profile* (column sums), 'I' for

*Integrated Intensity*, and 'B' for *Block Transfer*. 2) The number of frames accumulated in an image is stored since the intensities stored in FILENAME.LDD are not normalized with respect to this number. [Intensities are always extracted from the accumulated frame buffer.] This must be kept in mind when writing data manipulation programs. 3) The previous discussion implies that only one independent variable per experiment is stored, but in actuality, two independent variables per experiment are stored to allow the user some flexibility in modifying ACQUIRE.EXE. Currently, the secondary independent variable is used to store time in all cases other than when time is the independent variable. When the independent variable is time, 0.0 is stored at the location of the secondary independent variable. 4) The file pointer allows FILENAME.LDR to communicate with FILENAME.LDD. The value of the file pointer indicates where the intensities for a given record begin in FILENAME.LDD.

The number of intensities associated with a given record is determined by the window type. The number of intensities for *X Profile* and *Mean Horizontal Profile* corresponds to the width of the window. The number of intensities for *Y Profile* and *Mean Vertical Profile* corresponds to the height of the window. The number of intensities for *Block Transfer* corresponds to the product of the width and height of the window. The number of intensities for *Integrated Intensity* is two, the integrated intensity after background subtraction and the background intensity.

The window type also determines the numerical representation of the intensities. For *X Profile*, *Y profile*, and *Block Transfer*, the intensities are stored as unsigned integers (2 bytes). For *Mean Vertical Profile* and *Mean Horizontal Profile*, the intensities are stored as unsigned long

integers (4 bytes). For *Integrated Intensity*, the intensities are stored as single precision floating points (4 bytes).

The following example clarifies the procedure required to extract data from FILENAME.LDR and FILENAME.LDD. Suppose that one has collected x and y profiles for windows 0 and 1. After collecting these profiles, one wishes to generate text files for only x profiles associated with window 0. To accomplish this, first read a record stored in FILENAME.LDR with fread(), then determine whether the record fits the desired description. If the record is suitable, set the file pointer in FILENAME.LDD to the value stored in FILENAME.LDR with fseek(), and extract a total number of unsigned integers equal to the width of the window with fread(). Of course, this procedure must be repeated many times to step through the files in entirety. [Note: fread() and fseek() are Microsoft C functions.]

Intensities stored in FILENAME.LDD adhere to the following system of ordering. For *X Profile* and *Mean Horizontal Profile*, the intensities are stored from the left edge of the window to the right edge of the window. For *Y Profile* and *Mean Vertical Profile*, the intensities are stored from the top of the window to the bottom of the window. For *Block Transfer*, the intensities are stored as a sequence of x profiles, with the first x profile being from the top of the window and the last x profile being from the bottom of the window. For *Integrated Intensity*, the first intensity represents the integrated intensity after background subtraction and the second intensity represents the background intensity.

A knowledge of the ordering scheme in conjunction with the information stored in the records allows the user to determine (x,y) coordinates for profiles and block transfers. For example, if the window type is *X*

*Profile*, and the (x,y) coordinate of the center of the window is (256,240), and the width of the window is 11, then the (x,y) coordinates of the first and last intensities of the x profile are (251,240) and (261,240), respectively. It is important to note that the pixels have an aspect ratio of ca. 4:3. Since the pixels are not square, an equal number of pixels in the x and y directions does not correspond to equal lengths. Thus, one should use known distances, such as distances between spots, for establishing length scales.

## D. Format of FILENAME.LDS

An example of a FILENAME.LDS file is given below:

Date/Time: Thu Dec 31 23:59:59 1992

Operators: Dedicated chemist

Comments: The apple is descending in Times Square

X Parameter: Energy

MVP Offset: 51

MVP Gain: 204

Camera Parameters: Aperture =0.7

# VI. TIPS ON MODIFYING ACQUIRE.EXE

Source code files can be modified with the Microsoft Quick C editor, which provides excellent features for checking syntax errors. The Microsoft Quick C editor also provides compiling and linking features, but one must refrain from using them to produce ACQUIRE.EXE since Microsoft Quick C generates only medium memory model code.

Table 1 summarizes the major features associated with each of the ten source code files written specifically for ACQUIRE.EXE. Within these ten files are calls to a total of 177 unique functions. Tables 2-5 partition these functions according to their origin in order to avoid confusion during editing. Table 2 lists functions defined in the source code files, Table 3 lists Matrox functions, Table 4 lists Halo functions, and Table 5 lists Microsoft C functions along with their corresponding header files. [Note: Tables 1-5 are presented at the end of the appendix.]

Some functions listed in Table 2 serve the sole purpose of hiding Halo functions. The necessity of this arises from conflicts between the names of Halo and Matrox functions. As mentioned previously, the im_ prefix required for Matrox functions does not appear explicitly in the source code files. Without this prefix, several Halo and Matrox functions become identical in name. To circumvent this problem, all Halo functions are imbedded in functions defined in COMMON.C, which does not contain calls to Matrox functions.

Two functions defined in COMMON.C are of particular importance: outputtext() and graphgets(). The first function is used to output all text to the computer monitor. The second function is used to retrieve all

keyboard input. Both functions use Halo functions to accomplish their task, since equivalent Microsoft C functions are not compatible with the Halo graphics environment.

Before calling Matrox functions, one must ensure that the video processor is operating in an appropriate mode: I/O, graphics, or processing. Incompatibility between the function and the current operating mode results in undefined behavior. To select the proper operating mode, call im_opmode(). The source code files are written such that the number of calls to im_opmode() is minimized. This method of programming has the advantage of producing efficient code, but has the disadvantage of increasing the burden of keeping track of the current operating mode. To facilitate the procedure of keeping track of the current operating mode to some extent, the operating mode is always set to processing before returning to a menu. Therefore, if no prior change in the operating mode has occurred, a Matrox function requiring processing mode can be called safely without a call to im_opmode().

Variables declared in ACQUIRE.C prior to the definition of main() have global status, i.e., they can be made visible to other source code files by using the extern statement. To minimize the risk of inadvertently changing its value, a variable should be given global status only when the following criteria need to be satisfied: 1) The variable must exist for the lifetime of the program. 2) The variable must be visible to many source code files.

Since ACQUIRE.EXE is a menu-driven program, one will have to modify the menus in order to incorporate additional features.

Each menu is represented by the following structure type defined in LEED.H:

```
/*definition of structure type MENU-----------------------------------*/
typedef struct{
 int options; /*number of selectable options*/
 char *strings[MAXSTRINGS]; /*array of pointers to character strings*/
 }MENU;
/*end of definition---------------------------------------------------*/
```

MAXSTRINGS determines the size of the pointer array, which must be at least as large as the number of selectable options plus one for the title of the menu.

The following code segment demonstrates the proper procedure for initializing and acting upon the contents of a menu:

```
/*start of code segment-----------------------------------------------*/
void generic_function(void) /*function definition to follow*/
{
static MENU generic_menu={ /*initialize the contents of the menu*/
 2, /*number of selectable options*/
 "MENU NAME" /*title of the menu*/
 "Option 1" /*first option*/
 "Option 2" /*second option*/
 };
int logical=TRUE; /*boolean logic: TRUE(FALSE) =1(0)*/
while(logical) /*stay in while loop if TRUE*/
 {
 drawmenu(&generic_menu); /*draw the menu*/
```

```
 switch(getselection(&generic_menu)) /*choose an option*/
  {
  case 1: action_1(); break; /*if getselection() returns 1*/
  case 2: action_2(); break; /*if getselection() returns 2*/
  case ESCAPE: logical =FALSE; /*if getselection() returns the Esc key
  code, then terminate the while loop and return to the function that
  called generic_function()*/
  }
 }
}
/*end of code segment-----------------------------------------------------*/
```

The static statement allows generic_menu to exist for the lifetime of the program. Although static variables are identical to global variables in lifetime, they differ in two other respects: 1) Static variables cannot be modified. 2) The visibility of static variables is local rather than global.

Table 1. Major features associated with each source code file

| Source code file | Major features |
|---|---|
| ACQUIRE.C | • Initialize the video processor board<br>• Initialize window parameters<br>• Options in ACQUIRE<br>• Display the table of current values for parameters other than window parameters<br>• Copy FILENAME.LDR and FILENAME.LDD from the RAM drive to the current working directory<br>• Write FILENAME.LDS to the current working directory |
| SETUP.C | • Options in SETUP<br>• Options in IMAGE |
| WINDOWS.C | • Options in WINDOWS<br>• Window editor<br>• Write FILENAME.LDP to the current working directory |
| DATA.C | • Options in DATA<br>• User input experiment<br>• Write FILENAME.LDR and FILENAME.LDD to the RAM drive<br>• Auto centering routine |
| ENERGY.C | • Energy experiment |
| TIMERAMP.C | • Time experiment |
| ALIGN.C | • Determine normal incidence |
| DTOA.C | • Output DAC value to the analog and digital I/O board |
| FWHM.C | • Calculate FWHM of profiles |
| COMMON.C | • Initialize Halo graphics<br>• Menu functions<br>• Text input and output functions<br>• Error handling functions<br>• DOS Shell<br>• Imbedded Halo functions<br>• Utility functions |

Table 2. Functions defined in the source code files

| Function | Source code file |
|---|---|
| abnormalquit() | COMMON.C |
| align() | ALIGN.C |
| backfptr() | DATA.C |
| beamenergy() | SETUP.C |
| boundarycheck() | WINDOWS.C |
| calcfwhm() | FWHM.C |
| camprams() | SETUP.C |
| center() | DATA.C |
| changecoord() | COMMON.C |
| checkspace() | DATA.C |
| checkzero() | COMMON.C |
| cleargraphics() | COMMON.C |
| continuoussnaps() | SETUP.C |
| copyfiles() | ACQUIRE.C |
| data() | DATA.C |
| deltasize() | WINDOWS.C |
| deltatime() | DATA.C |
| displayform() | SETUP.C |
| dosshell() | COMMON.C |
| drawbar() | COMMON.C |
| drawbox() | COMMON.C |
| drawcolor() | COMMON.C |
| draweditor() | WINDOWS.C |
| drawintensitytable() | WINDOWS.C |
| drawline() | COMMON.C |
| drawmenu() | COMMON.C |
| drawprofile() | WINDOWS.C |
| drawwindow() | WINDOWS.C |
| drawwintypetable() | WINDOWS.C |

Table 2. (Continued)

| Function | Source code file |
|---|---|
| editor() | WINDOWS.C |
| editwindows() | WINDOWS.C |
| energycoeffs() | SETUP.C |
| energyramp() | ENERGY.C |
| errortext() | COMMON.C |
| evcal() | SETUP.C |
| flushkeybrd() | COMMON.C |
| fwhm() | FWHM.C |
| getcode() | COMMON.C |
| getcomments() | SETUP.C |
| getimage() | SETUP.C |
| getname() | SETUP.C |
| getselection() | COMMON.C |
| gettitle() | SETUP.C |
| getxpram() | DATA.C |
| go() | DATA.C |
| graphgets() | COMMON.C |
| histogram() | SETUP.C |
| imageaverage() | SETUP.C |
| information() | ACQUIRE.C |
| inithalo() | COMMON.C |
| initialize() | ACQUIRE.C |
| initmatrox() | ACQUIRE.C |
| initstreams() | DATA.C |
| inputchannel() | SETUP.C |
| livecam() | SETUP.C |
| main() | ACQUIRE.C |
| makecpath() | COMMON.C |
| MKFP() | COMMON.C |

Table 2. (Continued)

| Function | Source code file |
|---|---|
| mywaitcommand() | DTOA.C |
| newexperiment() | ACQUIRE.C |
| numframes() | SETUP.C |
| numwindows() | WINDOWS.C |
| offsetgain() | SETUP.C |
| onenergy() | WINDOWS.C |
| outputtext() | COMMON.C |
| pause() | COMMON.C |
| printhistodata() | SETUP.C |
| quit() | ACQUIRE.C |
| quithalo() | COMMON.C |
| reinitwin() | WINDOWS.C |
| resetinitstate() | ENERGY.C |
| resettimer() | DATA.C |
| restoreinitialstate() | ALIGN.C |
| rewindfptr() | DATA.C |
| samplingsize() | WINDOWS.C |
| saveparameters() | WINDOWS.C |
| selprofile() | WINDOWS.C |
| setkeybrd() | COMMON.C |
| setoluts() | ACQUIRE.C |
| setup() | SETUP.C |
| stopwatch() | ACQUIRE.C |
| sublinear() | FWHM.C |
| textcolor() | COMMON.C |
| timeramp() | TIMERAMP.C |
| userinput() | DATA.C |
| viewwindows() | WINDOWS.C |
| voltageout() | DTOA.C |

Table 2. (Continued)

| Function | Source code file |
|---|---|
| windowname() | WINDOWS.C |
| windows() | WINDOWS.C |
| windowtype() | WINDOWS.C |
| winpramstable() | WINDOWS.C |
| winshade() | WINDOWS.C |
| wintypeindicators() | WINDOWS.C |
| writedata() | DATA.C |
| writesummaryfile() | ACQUIRE.C |
| xyprofile() | WINDOWS.C |
| yesno() | COMMON.C |

Table 3. Matrox functions

| Function | Function |
|---|---|
| im_cbl() | im_line() |
| im_chan() | im_move() |
| im_clear() | im_offset() |
| im_colr() | im_olutlay() |
| im_cwb() | im_opmode() |
| im_dot() | im_outpath() |
| im_drawhist() | im_pixr() |
| im_drawmode() | im_rline() |
| im_faverage() | im_rmove() |
| im_gain() | im_rowr() |
| im_gclear() | im_rrect() |
| im_gtext() | im_scaling() |
| im_histmode() | im_setcolor() |
| im_histo() | im_sumvector() |
| im_init() | im_sync() |
| im_key() | im_video() |

Table 4. Halo functions

| Function | Function |
|---|---|
| bar() | initgraphics() |
| box() | lnabs() |
| closegraphics() | movabs() |
| clr() | setcolor() |
| ftcolor() | setcrange() |
| ftinit() | setdev() |
| ftlocate() | setdrange() |
| ftsize() | setxor() |
| fttext() | |

Table 5. Microsoft C functions and their corresponding header files

| Function | Header file |
|---|---|
| atof() | STDLIB.H or MATH.H |
| atoi() | STDLIB.H or MATH.H |
| atol() | STDLIB.H or MATH.H |
| calloc() | STDLIB.H and MALLOC.H |
| ctime() | TIME.H |
| exit() | STDLIB.H or PROCESS.H |
| fclose() | STDIO.H |
| fopen() | STDIO.H |
| fprintf() | STDIO.H |
| fread() | STDIO.H |
| free() | STDLIB.H and MALLOC.H |
| fseek() | STDIO.H |
| ftell() | STDIO.H |
| ftime() | SYS\TYPES.H and SYS\TIMEB.H |
| fwrite() | STDIO.H |
| getch() | CONIO.H |
| getcwd() | DIRECT.H |
| inp() | CONIO.H |
| kbhit() | CONIO.H |
| max() | STDLIB.H |
| outp() | CONIO.H |
| printf() | STDIO.H |
| rewind() | STDIO.H |
| spawnl() | STDIO.H and PROCESS.H |
| sprintf() | STDIO.H |
| strcat() | STRING.H |
| strcpy() | STRING.H |
| strlen() | STRING.H |
| system() | STDLIB.H and PROCESS.H |

Table 5. (Continued)

| Function | Header File |
|---|---|
| time() | TIME.H |
| toupper() | CTYPE.H |